Summer 2021

Electrohydrodynamic Simulations of Capsule Deformation Using a Dual Time-Stepping Lattice Boltzmann Scheme

Charles Leland Armstrong
Old Dominion University, charles.armstrong829@gmail.com

ELECTROHYDRODYNAMIC SIMULATIONS OF CAPSULE DEFORMATION USING A DUAL TIME-STEPPING LATTICE BOLTZMANN SCHEME

by

Charles Leland Armstrong
B.S. August 2015, Old Dominion University
M.S. December 2018, Old Dominion University

A Dissertation Submitted to the Faculty of
Old Dominion University in Partial Fulfillment of the
Requirements for the Degree of

DOCTOR OF PHILOSOPHY

COMPUTATIONAL AND APPLIED MATHEMATICS

OLD DOMINION UNIVERSITY
August 2021

Approved by:

Yan Peng (Director)

Gordon Melrose (Member)

Li-Shi Luo (Member)

Xiaoyu Zhang (Member)

ABSTRACT

ELECTROHYDRODYNAMIC SIMULATIONS OF CAPSULE DEFORMATION USING A DUAL TIME-STEPPING LATTICE BOLTZMANN SCHEME

Charles Leland Armstrong
Old Dominion University, 2021
Director: Dr. Yan Peng

Capsules are fluid-filled, elastic membranes that serve as a useful model for synthetic and biological membranes. One prominent application of capsules is their use in modeling the response of red blood cells to external forces. These models can be used to study the cell's material properties and can also assist in the development of diagnostic equipment. In this work we develop a three-dimensional model for numerical simulations of red blood cells under the combined influence of hydrodynamic and electrical forces. The red blood cell is modeled as a biconcave-shaped capsule suspended in an ambient fluid domain. Cell deformation occurs due to fluid motion and electrical forces that arise due to differences in the electrical properties between the internal fluid, external fluid, and cell membrane. The electrostatic equations are solved using the immersed interface method. A finite element method is used to compute the membrane's elastic forces and the membrane's bending resistance is described by the Helfrich bending energy functional. The membrane forces are coupled to the fluid equations through the immersed boundary method, where the elastic, bending, and electric forces appear as force densities in the Navier-Stokes equations. The fluid equations are solved using a novel dual time-stepping (DTS) lattice Boltzmann method (LBM), which decouples the fluid and capsule discretizations. The computational efficiency of the DTS scheme is studied for capsules in shear flow where it is found that the newly proposed scheme decreases computational time by a factor of 10 when compared to the standard LBM capsule model. The method is then used to study the dynamics of spherical and biconcave capsules in a combined shear flow and DC electric field. For spherical capsules the effect of field strength, shear rate, membrane capacitance, and membrane conductance are studied. For biconcave capsules the effect of the electric field on the tumbling and tank-treading modes of biconcave capsules is discussed.

ACKNOWLEDGEMENTS

I am extremely grateful to my advisor, Dr. Yan Peng, for personally selecting me to work on this topic. I have benefitted immensely from her support, guidance, and expertise. I would also like to thank my committee members for their time and feedback. The books Dr. Li-Shi Luo loaned me were particularly helpful during the early stages of this project.

I was also fortunate to have had the support of two tremendous graduate program directors in Dr. Raymond Cheng and Dr. Ruhai Zhou. Their prompt responses and advice throughout my graduate career made navigating the requirements of my degrees much easier. The professors in the Department of Mathematics and Statistics at ODU also played an integral role in my success. My coursework at ODU spanned everything from single variable calculus with Dr. Cheng to tensor calculus with Dr. Melrose. They have, quite literally, taught me everything I know.

I would also like to thank my classmates in the Applied Mathematics program. I hope they have learned as much from me as I have learned from them. I was fortunate to have two great friends during my graduate studies in Johnathon Upperman and Robert Riggs. Their friendship made my time at ODU much more enjoyable and I have learned a great deal from both of them.

I would like to acknowledge the National Science Foundation for funding this research. This research was also supported by the Research Computing clusters at Old Dominion University. In addition to using their computational resources, the technical support provided by the HPC group was invaluable.

Outside the university, my internships with the AFRL Scholars program were excellent learning experiences. The mentorship from Dr. Michael White and Dr. Ryan Phillips has made me a better scientist and their advice and support was instrumental in determining the next steps in my career.

I would like to thank my parents for their unwavering love and support. Their early emphasis on education set me up for a life of learning, despite my fervent, youthful protests.

Finally, I would like to thank my wife for her patience and sacrifices during my graduate studies. Her love and companionship have helped me to become the person I am today and I look forward to continuing our journey together.

NOMENCLATURE

$[x]$	Units of the quantity x
$\delta\rho$	Density fluctuation
Δt	Physical time step
δt	Lattice Boltzmann time step
Δx	Spatial grid spacing
ε	Permittivity
ε_r	Permittivity ratio
η	Bulk viscosity
κ	Mean curvature
κ_g	Gaussian curvature
λ	Viscosity ratio
$\lambda_{1,2}$	Two-dimensional principle stretch ratios
$[\![f]\!]$	Jump in the quantity f across an interface
$\mathbf{c}_i$	ith lattice velocity
$\mathbf{E}$	Electric field
$\mathbf{f}_b$	Bending force density
$\mathbf{f}_e$	Electric force density
$\mathbf{f}_m$	Elastic force density
$\mathbf{G}$	Two-dimensional Right Cauchy-Green tensor

$\mathbf{J}$	Current density
$\mathbf{j}$	Momentum density
$\mathbf{m}$	Moment vector
$\mathbf{M}$	Moment matrix
$\mathbf{m}^{\text{eq}}$	Equilibria moment vector
$\mathbf{S}$	Relaxation matrix
$\mathbf{v}$	Velocity field
μ	Viscosity
ν	Kinematic viscosity
Ω^{+}	Domain of ambient fluid
Ω^{-}	Domain of capsule fluid
ϕ	Levelset function
Ψ	Discrete electric potential
ψ	Continuous electric potential
ρ	Fluid density
ρ_0	Reference density
Σ	Surface of membrane
σ	Conductivity
σ_r	Conductivity ratio
τ_E	Electric stress tensor
τ_H	Hydrodynamic Stress Tensor

Ca	Capillary number
Ca_E	The electric capillary number
Ma	Mach number
Mn	Mason number
Re	Reynolds number
Re_E	Electric Reynolds number
θ	Inclination angle
a	Equivalent radius
A_0	Initial area of finite element
A_{vor}	Area of Voronoi region
c	Lattice Constant
c_0	Spontaneous curvature
C_m	Membrane capacitance
c_s	Speed of sound
D_{xy}	Deformation parameter
E_0	Electric field strength
E_B	Bending modulus
E_b	Dimensionless bending stiffness
E_s	Shear elasticity modulus
f_i	Distribution function for the ith lattice velocity
G_m	Membrane conductance

k	Shear rate
p	Hydrodynamic pressure
t_b	Bending relaxation time
t_c	Membrane charging relaxation time
t_e	Charge Relaxation time
t_f	Fluid relaxation time
t_m	Elastic relaxation time
V_m	Transmembrane potential
W	Strain energy function
W_b	Bending energy function

TABLE OF CONTENTS

Chapter Page

LIST OF TABLES

LIST OF FIGURES

Figure Page

Figure Page

Figure Page

CHAPTER 1

INTRODUCTION

The study of fluid-filled deformable particles has widespread applications. In manufacturing the response of deformable particles to external forces is essential for technologies such as inkjet printing [1], oil refinement [2], food processing [3], and cosmetics [4]. Furthermore, understanding the behavior of synthetic microcapsules [5], artificial vesicles [6], and biological membranes [7] is essential for biomedical applications such as drug delivery [8] and gene therapy [9]. Of particular interest in this work is the deformation of red blood cells. The highly deformable red blood cell membrane plays a crucial role in blood flow, affecting the rheological properties of blood on the macroscopic scale [10] and enabling the passage of individual cells through narrow capillaries [11]. Microfluidic devices that induce deformation via mechanical flows and electric fields have been developed for diagnosing diseases such as malaria and sickle cell anemia [12, 13], which adversely affect erythrocyte deformability [14], and have also been proposed for the sorting of healthy blood [15]. In the past, numerical simulations have been used in the development of microfluidic devices as they provide a controlled method of assessing the impact that device and cell parameters play in the underlying physics [16]. Thus, the continued development of numerical models for the simulation of red blood cell deformation in flows and electrical fields will aid advances in microfluidic technology.

The simplest model for deformable particles is the droplet, in which an interfacial tension balances the viscous forces between the fluids. The droplet model neglects important features of biological membranes such as area dilation, shear deformation, and bending resistance. Multiscale models, accounting for the microscopic behavior of the membrane have been proposed [17], however continuum models such as capsule and vesicle models are the more common choice. Vesicles are area-preserving membranes, while capsules are elastic membranes, and thus a key distinction between the two is that spherical vesicles will not exhibit deformation, whereas spherical capsules deform due to membrane stretching. The red blood cell membrane is typically modeled as an area-incompressible, elastic capsule [18] and thus, in this work we use the capsule model as well.

Constitutive laws can be employed to impart the capsule membrane with area incompressibility [18], bending resistance [19], and viscosity [20].

1.1 DEFORMATION IN SHEAR FLOW

Interest in deformable particles in shear flow dates back to the work of Sir G. I. Taylor [21], who derived an analytical estimate of the viscosity of a suspension of fluid droplets in an ambient fluid. Later experiments on suspensions of hardened red blood cells in shear flow demonstrated the critical role of flow-induced cell deformation on the macroscopic characteristics of the flow [10]. These findings motivated the study of the deformation of individual red blood cells which revealed the complex dynamics of cell deformation in shear flows [22, 23, 24]. At low shear rates the red blood cell acts as a rigid body, tumbling in the flow, however as the shear rate increases the cell exhibits a phenomenon known as tank-treading, wherein the membrane rotates around the cell contents [25]. In addition to these modes, recent experiments have categorized a number of intermittent phases of red blood cell deformation including swinging, spinning, and rolling motions that had not been previously reported [26, 27].

These dynamics have been the focus of extensive modeling efforts, which were the subject of the recent review by Barthés-Biesel in [28]. A fluid droplet model of red blood cells predicted the tank-treading behavior seen at higher shear rates [22, 23], however the tank-treading frequency of droplets is dependent on the ratio of the internal and external viscosities [29]. This contradicted the experiments of Fischer et al. who found that the tank-treading frequency of the cell membrane was independent of the viscosity of the suspending fluid [30] for red blood cells. These discrepancies motivated researchers to consider elastic capsule models of red blood cell membranes. The small deformation analysis done by Barthés-Biesel [31] and Barthés-Biesel and Rallison [32] for spherical capsules in shear flow predicted deformation to a steady spheroidal shape that exhibited the independence between tank-treading frequency and the viscosity ratio as reported in [30]. The small deformation analysis was later extended to spherical capsules with viscoelastic membranes [33] and was validated by the experimental investigations of Chang and Olbricht [34] and Walter et al. [35].

Due to the non-linearity of the fluid structure interaction, the study of capsules with large deformations or complex geometries is restricted to numerical and experimental investigations.

Early numerical studies included the Boundary element method (BEM) simulations conducted by Pozrikidis [36] and Ramanujan and Pozrikidis [37] and the Immersed Boundary Method (IBM) [38] simulations of Eggleton and Popel [39]. An experimental study by Walter et al. in [40] reported membrane buckling at the equator of the capsule, caused by membrane anisotropies not considered in the aforementioned small deformation theory. In [41, 42] Pozrikidis proposed that these anisotropies were caused by membrane bending resistance and incorporated transverse shear tensions due to bending moments into the two-dimensional membrane theory of [31, 32].

Early biconcave discoid simulations were reported in [37, 43, 39], however numerical instabilities and computational constraints limited the duration and parameter range of these simulations. As computing power has progressed the body of research on numerical simulations of red blood cells has grown considerably. In [44, 45] Sui et al. conduct simulations of the deformation of biconcave capsules in shear flow over a range of capillary numbers, reporting the transition from tumbling to tank-treading found experimentally for red blood cells [22]. In [46] Le studied the effects of membrane bending stiffness for biconcave capsules, reporting restricted deformation that altered the transition from the tumbling to tank-treading modes. The effects of membrane viscosity were studied by Fedosov, Caswell, and Karniadakis in [17] and Cordasco and Bagchi in [47]. A number of other studies on red blood cells in shear flow have been conducted, including BEM simulations in [48, 49, 50, 51, 52, 53] and front-tracking and IBM simulations in [54, 55, 56, 57]. Due to the large number of pre-existing studies, simulations of capsules in shear flow are used in this work to demonstrate the efficacy and efficiency of the proposed numerical scheme.

1.2 DEFORMATION IN AN ELECTRIC FIELD

Historically, the leaky dielectric model was motivated by the experiments of Allan and Mason [58] who observed that, when the dielectric constant of a liquid droplet was less than that of the surrounding fluid, drop deformation was perpendicular to the electric field. These results contradicted the existing theories of liquid droplets as perfect dielectrics, which predicted the alignment of the droplet with the electric field irrespective of the dielectric constants of the two fluids. In [59] Taylor demonstrated that, for weakly conducting fluids, tangential electric stresses develop, driving fluid motion near the droplet interface. In this case, the direction of flow depends on the

conductivity and permittivity of the two fluids and can result in deformation along or perpendicular to the electric field. The mathematical treatment of dielectric fluids with weak conductivities, dubbed the leaky dielectric model, was developed more fully by Melcher and Taylor in [60] and has been the subject of reviews by Saville [61], Vlahovska [62], and Abbasi et al. [63].

The electrical properties of biological membranes result in an electrically charged membrane that allows nutrients to flow into and out of the cell. The transmembrane potential model, proposed by deBruin and Krassowska in [64], considers the effects of the membrane's capacitance and conductance by adding a time dependent component to the current across the membrane. Small deformation studies on the effects of the transmembrane potential have been conducted for vesicles [65], where it is shown that the capacitance of the membrane insulates the interior fluid from the electric field, resulting in complex transient dynamics such as the oblate-prolate and prolate-oblate-prolate transitions.

A number of numerical studies have been conducted for vesicles in DC and AC electric fields, which were the subject of the review by Sinha et al. [66]. In [67, 68, 69] McConnell, Miksis, and Vlahovska use a boundary integral method to study the electrohydrodynamics of two dimensional vesicles in AC and DC electric fields. Of particular importance for this work are the results from [67], where the deformation of a vesicle is studied in a DC electric field with and without shear flow. The dynamics of vesicles in shear flow are reported to have a strong dependence on the strength of the electric field, with strong electric fields counteracting the expected dynamics of vesicles in shear flow. Kolahdouz and Salac use an immersed interface method [70, 71] for simulation of three dimensional vesicles in electric fields including studies of the prolate-oblate-prolate transition and the combined effects of DC electric fields and shear flows [72]. In [73] Morshed et al. use an immersed interface method to study the electrodeformation of vesicles for a wide range of conductivity ratios, electric field strengths, and vesicle shapes. In [74] Hu et al. a combined immersed interface and immersed boundary method is used to study the deformation of two dimensional vesicles. Their simulations include the prolate-oblate-prolate transition and simulations under a combined shear flow and DC electric field, where the effect of the electric field on the transition from tumbling to tank-treading is discussed.

The literature on capsules in electric fields is comparatively sparse. In [75] Ha and Yang apply small deformation theory to study the deformation of capsules under the combined effect of shear

flow and a uniform electric field, where the electric field was found to have a strong effect on the orientation of capsules in the flow. Analytical capsule models have also been used to predict the deformation of polysiloxane capsules suspended in oil [76, 77] and particle-covered drops [78] in DC electric fields. More recently, Thaokar conducted small deformation theory analysis of capsules in an AC electric field [79].

Numerical studies of capsules in electric fields have thus far been restricted to axisymmetric simulations [80, 81, 82]. In [80] Das and Thaokar conduct simulations on the deformation of spherical capsules in a DC electric field for a wide range of field strengths, conductivity ratios, membrane capacitances and membrane conductances, reporting complex deformations including capsule squaring and oblate-prolate shape transitions in strong electric fields. In [81] simulations are conducted for spherical capsules with a Skalak membrane in AC electric fields, reporting frequency and conductivity dependent modes as well as mode transitions. In [82] Das, Deshmukh, and Thaokar conduct simulations for biconcave capsules under the combined effect of an electric field and extensional flow. Due to their similar stress profiles, the deformation of biconcave disks in extensional flow and DC electric fields are both found to attain equilibrium shapes, described as ”capped spheroids” by the aforementioned authors.

1.3 DUAL TIME-STEPPING CAPSULE MODEL

The fluid structure algorithm used in this work is a coupled lattice Boltzmann method immersed boundary method (LBM-IBM) that is well-established and has been used in similar studies on capsule deformation such as those in [44, 83, 84]. For LBM-IBM simulations of capsule deformation, the resolution of the fluid velocity plays an outsized role in the accuracy of the method [83] and thus, a relatively fine Eulerian mesh is desirable. Due to the coupling between the temporal and spatial discretizations of the lattice Boltzmann equation this places a stringent constraint on the time step. For LBM-IBM simulations this limitation results in a time step that is orders of magnitude smaller than the elastic and fluid time scales of the problem.

The large separation between the relevant temporal and spatial scales suggests that de-coupling the LBM time step from the physical time step by employing a dual time-stepping (DTS) scheme could reduce the computational time required for capsule simulations. Applications of DTS

schemes have been reported for spectral [85] and finite volume [86] models of the lattice Boltzmann equation. A DTS procedure was also recently incorporated into a LBM-IBM scheme for simulation of flow past a cylinder [87]. The transient terms were added as a source into the LBE, and the resulting equations are solved using the multigrid lattice Boltzmann method originally developed by Mavriplis in [88]. The authors reported speed up of approximately 4 when compared with the traditional LBM for unsteady flow past a cylinder [87].

In this work we propose a quasi-steady, dual time-stepping (DTS) scheme that couples the multigrid lattice Boltzmann method (LBM) [88] to a IBM method in order to reduce the computational time required to simulate flow-induced capsule deformation at low Reynolds numbers. The quasi-steady implementation of the LBM-IBM capsule model treats each time step as a steady flow problem, allowing us to de-couple the LBM time discretization, which is tied to the spatial discretization, from the capsule discretization. This allows for a physical time step orders of magnitude larger than the one required by traditional LBM-IBM capsule models. Neglecting the transient terms of the incompressible Navier-Stokes equations reduces the computational and memory requirements when compared with the method proposed in [87] without sacrificing accuracy in the low Reynolds number regime of capsule deformation. The proposed quasi-steady scheme also allows for easy incorporation into pre-existing LBM-IBM capsule codes.

1.4 SCOPE AND OUTLINE

This thesis has 3 principal aims. First, a novel dual time-stepping scheme is presented for LBM-IBM capsule simulations. The computational efficiency of the new scheme is compared to the standard LBM-IBM capsule model, where it is demonstrated that decoupling the spatial and temporal discretizations reduces the computational burdens associated with increases in the resolution of the Eulerian mesh. Second, the LBM-IBM capsule model is coupled to to the immersed interface method to facilitate three dimensional electrohydrodynamic simulations of capsules. Several studies have coupled the immersed boundary method with the immersed interface method [89, 74, 90, 73] for two dimensional models, however, to the best of the present authors' knowledge, no three dimensional IBM-IIM coupled schemes have been reported. Third, the dual time-stepping LBM-IBM-IIM scheme is used to study the deformation of capsules under the combined effects of a DC electric field and shear flow. The combined effect of a DC electric field and shear flow

have been studied for droplets [91, 89, 92] and vesicles [93, 72, 74], however, to the best of the present authors' knowledge, the only study for capsules was the small deformation analysis of Ha and Yang [75]. The study done in [75] only considered spherical capsules and neglected the effects of the transmembrane potential, and thus, the present study for spherical and biconcave capsules with transmembrane potential will fill a gap in the literature.

The remainder of the thesis is organized in the following manner: In Chapter 2, the physical problem of a capsule under the combined effects of a uniform electric field and a shear flow is discussed. The governing equations for the leaky dielectric model and the membrane mechanics are presented and the important physical parameters are discussed.

In Chapter 3, the numerical methods used in this work are presented. First, the lattice Boltzmann method and multigrid lattice Boltzmann method are discussed. Second, the immersed interface method and the interpolation scheme are discussed for computation of the electric potential and electric forces respectively. Next, the numerical algorithms for computation of the elastic and bending forces are discussed for the triangular capsule mesh used in this work. Following this, the numerical methods used for fluid-structure interaction, including the coupling of the immersed boundary method and the immersed interface method, are discussed. Finally, the dual time-stepping scheme for capsule deformation is presented.

In Chapter 4, simulations of capsules in shear flow are conducted. First, the results from the DTS scheme proposed here are validated for spherical and spheroidal capsules by comparison to previously published works. Next, the DTS scheme is used to study the transition from tank-treading to tumbling and is compared with previously reported studies. Finally, the efficiency of the dual time-stepping scheme is assessed by comparing the computational times of simulations conducted with the DTS scheme to the computational times of simulations conducted with the standard LBM-IBM capsule model for spherical and biconcave capsules.

In Chapter 5, the dual-time stepping scheme is applied to electrohydrodynamic simulations of capsule deformation in a DC electric field. First, the coupled immersed boundary-immersed interface method is validated through comparison of the steady state deformation of spherical capsules obtained numerically to those obtained using small deformation theory. The chapter concludes with a simulation of the prolate-oblate-prolate transition for elastic capsules.

In Chapter 6, the dual-time stepping scheme is used to study capsule deformation under the

combined influence of a shear flow and a DC electric field. First, the deformation of spherical capsules is studied for various field strengths, shear rates, viscosity ratios, conductivity ratios, and membrane conductivities. The relative effects of the shear flow and electric field are discussed and compared to previous studies. The chapter concludes with simulations of biconcave capsules in a combined shear flow and electric field, where the effect of the electric field on the tumbling and tank-treading modes is discussed. In Chapter 7, the work is concluded with a discussion of the important findings and future directions.

CHAPTER 2

CAPSULE MODEL

In this work we simulate the flow-induced deformation of a three-dimensional capsule under the combined effects of shear flow and a uniform DC electric field. The membrane is modeled as a two-dimensional closed surface, Σ, embedded in a three-dimensional parallelepiped domain. The membrane's mechanical response is parametrized by the Young's surface modulus, $[E_s] = \mathrm{N} \cdot \mathrm{m}^{-1}$, and the bending stiffness modulus, $[E_B] = \mathrm{J}$. The membrane's electrical response is characterized by the membrane permittivity, $[\varepsilon_m] = \mathrm{F} \cdot \mathrm{m}^{-1}$, and membrane conductivity, $[\sigma_m] = \mathrm{S} \cdot \mathrm{m}^{-1}$. The characteristic length of the capsule is given by the equivalent radius, $[a] = \mathrm{m}$, defined as the radius of a sphere with the same volume as the capsule. The membrane surface, Σ, divides the domain into two subdomains, with Ω^- denoting the capsule interior and Ω^+ denoting the region outside the capsule. The viscosity, permittivity, and conductivity in Ω^+ are denoted by, $[\mu^+] = \mathrm{Pa} \cdot \mathrm{s}$, $[\varepsilon^+] = \mathrm{F} \cdot \mathrm{m}^{-1}$, and $[\sigma^+] = \mathrm{S} \cdot \mathrm{m}^{-1}$, respectively. Similarly, the viscosity, permittivity and conductivity in Ω^- are denoted by $[\mu^-] = \mathrm{Pa} \cdot \mathrm{s}$, $[\varepsilon^-] = \mathrm{F} \cdot \mathrm{m}^{-1}$, and $[\sigma^-] = \mathrm{S} \cdot \mathrm{m}^{-1}$, respectively.

A schematic diagram of the plane of shear can be seen in Figure 1. In the y coordinate direction the computational domain is confined by two moving walls, which drive a shear flow in the $x-y$ plane. In the x and z coordinate directions the fluid is assumed to be periodic. The flow is characterized by the shear rate, $[k] = \mathrm{s}^{-1}$. A potential difference is applied between the confining walls, resulting in a uniform electric field in the y coordinate direction. The electric field strength is denoted $[E_0] = \mathrm{V} \cdot \mathrm{m}^{-1}$.

2.1 THE LEAKY DIELECTRIC MODEL

The leaky dielectric model, first proposed by Taylor and Melcher in [59, 60], describes the electrohydrodynamics of flows that arise due to stresses at the interface of fluids with different

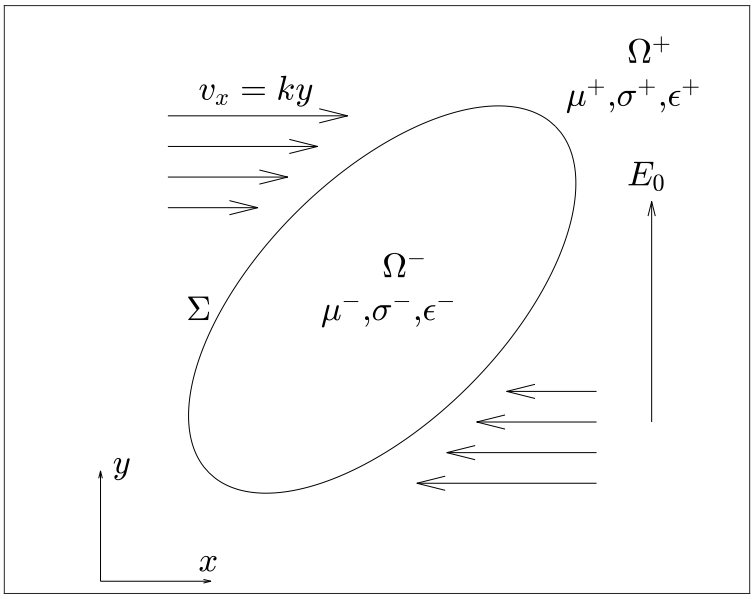

Fig. 1: Schematic of a Capsule in a Shear Flow with a Uniform DC Electric Field.

electrical properties. The fluids in Ω^+ and Ω^- are Newtonian fluids governed by the incompressible Navier-Stokes equations:

$$\rho(\partial_t \mathbf{v} + \mathbf{v}\cdot\nabla\mathbf{v}) = -\nabla\cdot\tau + \mathbf{p} \tag{1}$$

$$\nabla\cdot\mathbf{v} = \mathbf{0} \tag{2}$$

where ρ is the fluid density, $\mathbf{v}$ is the fluid velocity, τ is the stress tensor, and $\mathbf{p}$ is the external force density.

The stress tensor, τ, has contributions from viscous stresses, τ_H, and electric stresses, τ_E. The electric stresses are given by the Maxwell stress tensor for a dielectric material:

$$\tau_E = \varepsilon\mathbf{E}\mathbf{E}^T - \frac{1}{2}\varepsilon\mathbf{E}\cdot\mathbf{E}\mathbb{I} \tag{3}$$

where ε is the permittivity of the fluid and $\mathbf{E}$ is the electric field. The viscous stresses for a Newtonian fluid are given by:

$$\tau_H = -pI + \mu\left[\nabla\mathbf{v} + \nabla\mathbf{v}^T\right] \tag{4}$$

where μ is the fluid viscosity and p is the fluid pressure.

The material properties, μ^+, μ^-, ε^+, ε^-, σ^+, and σ^- are assumed to be constant in the bulk, however the fluids may have a jump in viscosity, permittivity, or conductivity across the interface, Σ. The jump in electrical properties results in the accumulation of charge on the interface between the two fluids and thus, for phenomena which occur on time scales much larger than the charge relaxation time, there is no charge in the bulk. When time-varying currents are negligible, the conservation of charge can be expressed in terms of the potentials ψ^+ and ψ^-, denoting the potential inside and outside the capsule respectively, as follows:

$$\sigma^+ \Delta \psi^+ = 0 \quad \text{in} \quad \Omega^+ \tag{5}$$

$$\sigma^- \Delta \psi^- = 0 \quad \text{in} \quad \Omega^-. \tag{6}$$

The system is closed by suitable boundary conditions for the jump in the potential, $[\![\psi]\!]$, and the current, $[\![\sigma \psi_n]\!]$ across the membrane.

The modeling of biological membranes requires consideration of the membrane's electrical properties, which result in a potential difference between the internal and external BCs. The jump in potential, known as the transmembrane potential, coupled with the continuity of the electrical current across the interface, give us the following boundary conditions across the interface:

$$[\![\psi]\!] = V_m \tag{7}$$

$$[\![\sigma \psi_n]\!] = 0 \tag{8}$$

where V_m is the transmembrane potential, which is a time-dependent function defined on the surface of the interface. It should be noted that we have adopted the convention from [74], defining $V_m = \psi^+ - \psi^-$. This definition differs by a sign from the classical transmembrane potential used in [64].

In this work we use the transmembrane potential model proposed by DeBruin and Krassowska in [64]. The membrane's electrical response is characterized by the the membrane capacitance, $\bar{C}_m = \varepsilon_m / d_m$, and the membrane conductance, $\bar{G}_m / d_m$, where d_m denotes the membrane thickness. The evolution equation for the transmembrane potential is obtained by balancing the sources of

currents on each side of the interface. In the absence of surface currents and charge convection the resulting expression equates the transmembrane potential to the current density as follows:

$$\begin{aligned} \sigma^{+}\psi_{n}^{+} &= \bar{C}_{m}\frac{\partial V_{m}}{\partial t} + \bar{G}_{m}V_{m} \\ \sigma^{-}\psi_{n}^{-} &= \bar{C}_{m}\frac{\partial V_{m}}{\partial t} + \bar{G}_{m}V_{m}. \end{aligned} \tag{9}$$

2.2 MEMBRANE MECHANICS

The membrane shape is parameterized by the Lagrangian surface coordinates $\mathbf{X} = \mathbf{X}\left(\mathbf{X}^{0}, t\right)$, where $\mathbf{X}^{0}$ denotes the set of Lagrangian coordinates for the initial capsule shape. The evolution of the capsule shape can be expressed in terms of the capsule membrane velocity, $\mathbf{V}$, as follows:

$$\frac{\partial \mathbf{X}}{\partial t} = \mathbf{V}\left(\mathbf{X}, t\right). \tag{10}$$

Continuity of the fluid velocity across the interface gives us the capsule velocity, $\mathbf{V} = \mathbf{v}^{-} = \mathbf{v}^{+}$, where $\mathbf{v}^{-}$ and $\mathbf{v}^{+}$ are the Eulerian fluid velocities inside and outside the membrane respectively.

The membrane forces are given by the elastic forces, $\mathbf{f}_{e}$, due to in-plane tensions and the bending forces, $\mathbf{f}_{b}$, due to transverse shear tensions. Jumps in the viscous and electric stresses across the membrane are balanced by the membrane forces:

$$[\![(\tau_{H} + \tau_{E}) \cdot \mathbf{n}]\!] = \mathbf{f}_{e} + \mathbf{f}_{b} \tag{11}$$

where the symbol $[\![\cdot]\!]$ denotes the jump in a quantity across the membrane.

The membrane forces are obtained from the principle of virtual work [46]. For a massless two dimensional membrane the total work is given by:

$$W = \int_{\Sigma} (W + W_{b})\, dA \tag{12}$$

where W is the strain energy per unit area and W_{b} is the bending energy per unit area. W and W_{b} are determined via the selection of constitutive laws describing the elastic and bending response of the membrane respectively.

2.2.1 ELASTIC FORCES

The elastic response of the capsule is determined through the selection of a constitutive law relating the strain energy per unit area to the principle stretches. In this work we use the neo-Hookean and Skalak constitutive laws. The neo-Hookean law was originally developed for three-dimensional solids and is a function of the three dimensional principle stretches, λ_1, λ_2, and λ_3. By assuming volume incompressibility, $\lambda_1\lambda_2\lambda_3 = 1$, we can write the strain energy function in terms of the in-plane stretches, λ_1 and λ_2, in the following form:

$$W^{\mathrm{NH}} = \frac{E_s}{6}\left[\lambda_1^2 + \lambda_2^2 + \lambda_1^{-2}\lambda_2^{-2} - 3\right] \tag{13}$$

where E_s is the Young's elastic modulus of the membrane.

Skalak's law is a two-dimensional constitutive law, originally proposed by Skalak et al. in [18], which was developed to account for the resistance to surface area dilation exhibited by red blood cell membranes. The strain energy function for Skalak's law is given by:

$$W^{\mathrm{SK}} = \frac{E_s}{8}\left[(\lambda_1^2 + \lambda_2^2 - 2)^2 + 2(\lambda_1^2 + \lambda_2^2 - 2) - 2(\lambda_1^2\lambda_2^2 - 1) + C(\lambda_1^2\lambda_2^2 - 1)^2\right]. \tag{14}$$

The final term on the right hand side of Equation (14) can be used to approximate area incompressibility by selecting $C \gg 1$. Although Skalak's law was designed to capture the area-incompressible red blood cell membrane, for values of $C \sim \mathscr{O}(1)$ the law can be used to simulate a general elastic membrane [94, 95].

It should be noted that there are multiple definitions of the surface elasticity modulus in the literature, varying by a constant scalar. For the neo-Hookean law we follow the definition used in [37, 44], which results in $E_s = 3G_{nh}$, where G_{nh} is the neo-Hookean elasticity modulus defined in [95]. For Skalak's Law we follow the definition used in [44, 55], which results in $E_s = 2G_{sk}\frac{1+2C}{1+C}$, where G_{sk} is the Skalak elasticity modulus defined in [95]. Care should be taken when comparing results from different researchers as the capillary number, Ca, Skalak parameter, C, and dimensionless bending modulus, E_b, all depend on the definition of the surface elasticity modulus that is used.

The expression of the elastic forces are derived in Section 3.4 in the context of the finite element

method used in this work.

2.2.2 BENDING FORCES

The capsule's bending resistance is modeled using the quadratic shape energy functional proposed by Helfrich in [19]:

$$W_b = \frac{E_B}{2}\int_S (2\kappa - c_0)^2 dS \tag{15}$$

where κ is the mean curvature, c_0 is the spontaneous curvature, and E_B is the bending stiffness modulus of the capsule. The spontaneous curvature is a parameter that defines the reference configuration for the capsule's bending energy. The bending force density, $\mathbf{f_b}$, is obtained by taking the first variation of Equation (15), which we can express in terms of the mean curvature, κ, spontaneous curvature, c_0, and Gaussian curvature, κ_g as follows [96]:

$$\mathbf{f_b} = E_B[(2\kappa + c_0)(2\kappa^2 - 2\kappa_g - c_0\kappa) + 2\Delta_{\mathrm{LB}}\kappa]\mathbf{n} \tag{16}$$

where Δ_{LB} is the Laplace-Beltrami operator.

2.3 DIMENSIONLESS PARAMETERS

The influence of the various forces are determined by the capillary number, the electric capillary number, and the dimensionless bending stiffness. The dimensionless bending stiffness is the ratio of the bending forces to the elastic forces and is given by:

$$E_b = \frac{E_B}{a^2 E_s}. \tag{17}$$

The capillary number, also referred to as the dimensionless shear rate by some researchers, is the ratio of the viscous to elastic forces and is given by:

$$\mathrm{Ca} = \frac{\mu^+ ak}{E_s}. \tag{18}$$

The electrical capillary number is the ratio of the electric forces to the elastic forces and is given

by:

$$\mathrm{Ca}_E = \frac{a\varepsilon^+ E_0^2}{E_s}. \tag{19}$$

The ratio of the electric forces to the viscous forces, or equivalently the ratio of the electric capillary number to the capillary number, is given by the Mason number:

$$\mathrm{Mn} = \frac{\varepsilon^+ E_0^2}{k\mu^+}. \tag{20}$$

It should be noted that since $\mathrm{Mn} = \mathrm{Ca}/\mathrm{Ca}_E$, only three of E_b, Ca, Ca_E, and Mn are independent. In this work we primarily discuss Ca, Ca_E, and E_b due to their physically-intuitive meanings. For a fixed value of E_s, Ca indicates the relative strength of the shear flow, Ca_E indicates the relative strength of the electric field, and E_b indicates the relative bending rigidity of the capsule.

The capsule's fluid properties are related to the ambient fluid properties through the following ratios:

$$\lambda = \frac{\mu^-}{\mu^+} \qquad \sigma_r = \frac{\sigma^-}{\sigma^+} \qquad \varepsilon_r = \frac{\varepsilon^-}{\varepsilon^+}. \tag{21}$$

The capsule's membrane conductance and capacitance also have dimensionless forms given by:

$$C_m = \frac{a\bar{C}_m}{\varepsilon^+} \qquad G_m = \frac{a\bar{G}_m}{\sigma^+}. \tag{22}$$

The Reynolds number is the ratio of the inertial forces to the viscous forces. For shear flow the characteristic velocity is $u_c = ka$ and thus Re is given by:

$$\mathrm{Re} = \frac{\rho k a^2}{\mu^+}. \tag{23}$$

For biological and microcapsule applications $\mathrm{Re} \ll 1$ [26, 27, 34, 40] and thus, numerical studies often use the Stokes approximation [37, 48, 49, 94]. Numerical studies that do consider the fluid inertia use Reynolds numbers in the range of $\mathrm{Re} = 0.01 - 0.1$ [97, 44, 55, 83, 84, 98] unless the inertial terms are the object of study as in [99].

The leaky dielectric model has a number of important time scales. For shear flow, the characteristic time scale is given by the fluid time scale:

$$t_f = k^{-1}. \tag{24}$$

The charge relaxation time scales describe the time scales on which the charge density in the bulk vanishes due to accumulation of charge on the membrane interface [60]. These time scales are given by:

$$t_e^+ = \frac{\varepsilon^+}{\sigma^+} \qquad\qquad t_e^- = \frac{\varepsilon^-}{\sigma^-}. \tag{25}$$

The ratio of the charge relaxation time scale, t_e^+, to the characteristic time scale is given by the electric Reynolds number, which for shear flow is given by:

$$\mathrm{Re}_E = \frac{\varepsilon^+ k}{\sigma^+}. \tag{26}$$

The leaky dielectric model is derived from the assumption that all charge resides on the membrane and thus, in this work we require $\mathrm{Re}_E \ll 1$ [60].

The characteristics of the membrane also play a role in the time scales of the problem. The elastic time scale describes the time scale on which the membrane deformation evolves and is given by:

$$t_m = \frac{a\mu^+}{E_s}. \tag{27}$$

The bending time scale is given by:

$$t_b = \frac{a\mu^+}{E_b E_s}. \tag{28}$$

For the transmembrane potential model used here, the membrane charging relaxation time, t_c, is given by:

$$t_c = \frac{a\bar{C}_m}{\sigma^+}\frac{2+\sigma_r}{2+\bar{G}_m(2+\sigma_r)}. \tag{29}$$

For the case of a non-conducting membrane the charging time is given by the simpler expression:

$$t_\mathrm{c} = \frac{a\bar{C}_m}{\sigma^+}(2+\sigma_r). \tag{30}$$

2.4 CAPSULE DEFORMATION AND INCLINATION ANGLE

The capsule dynamics are analyzed by looking at the the deformation parameter, D_{xy}, and the inclination angle, θ. The inclination angle is the angle between the capsule's major axis and the x coordinate axis. Initially proposed by Taylor in [100], the deformation parameter of a two-dimensional capsule is defined as:

$$D_{xy} = \frac{L-\ell}{L+\ell}. \tag{31}$$

where L and ℓ are the lengths of the major and minor axes of the capsule, respectively. For three dimensional capsules the deformation parameter and inclination angle are computed using the method discussed in [37, 97]. First, we compute the capsule's moment of inertia:

$$I_{ij} = \int_V (r_k r_k \delta_{ij} - r_i r_j) dV, \tag{32}$$

where $\mathbf{r}$ is the radial vector, pointing outward from the capsule center. The integral in Equation (32) is calculated using the method discussed by Ramanujan and Pozrikidis in [37]. Both D_{xy} and θ are then obtained from the eigenvalues and eigenvectors of I respectively. The eigenvalues of I correspond to the lengths of the axis of an ellipsoid with moment of inertia I. The lengths of the major and minor axis for this ellipsoid are used to approximate L and ℓ in Equation (31) [97]. The inclination angle, θ, is computed by finding the principle value of the angle between the capsule's major axis and the x axis.

CHAPTER 3

NUMERICAL METHODS

The proposed numerical framework for simulation of electrohydrodynamic capsule deformation consists of an Eulerian domain, $\Omega^+ \cup \Omega^-$, on which solution of the fluid and electrostatic variables are computed and the capsule surface, Σ, where membrane forces are computed. Fluid structure interaction is mediated by the immersed boundary method (IBM) [38], in which quantities are interpolated between the Eulerian grid and capsule membrane through discrete delta functions. On the Eulerian domain, the immersed interface method (IIM) [101, 74] is used to compute the electrostatic variables and a dual time-stepping lattice Boltzmann method [102] is used to compute the fluid variables. On the capsule surface the finite element method, first proposed by Charrier et al. in [103], is used to compute the elastic forces and the bending forces are computed from the Helfrich bending functional [19, 96].

The numerical scheme proposed here requires discretization of the capsule membrane and the Eulerian domain. The membrane is discretized using a triangular surface mesh, as pictured in Figure 2. The vertices of the triangles are tracked as a set of discrete Lagrangian coordinates throughout the simulation. For the discussion that follows the discrete Lagrangian coordinates will be denoted as $\mathbf{X}_i$. The Eulerian domain is discretized using a uniform grid in each coordinate direction. Unless otherwise noted, the Eulerian coordinates for the point $[x_i, y_j, z_k]^{\mathrm{T}}$ will be denoted as $\mathbf{x}_{ijk}$. In the immersed interface method discrete points on the interface, called control points, are required for discretization of the interface conditions. These points are separate from the Lagrangian points required by the immersed boundary method and will be denoted as $\bar{\mathbf{X}}_i$.

3.1 THE LATTICE BOLTZMANN METHOD

The fluids inside and outside the capsule are assumed to be incompressible Newtonian fluids governed by the incompressible Navier-Stokes equations:

$$\rho(\partial_t \mathbf{v} + \mathbf{v} \cdot \nabla \mathbf{v}) = -\nabla \cdot \tau + \mathbf{p} \tag{33}$$

$$\nabla \cdot \mathbf{v} = \mathbf{0}. \tag{34}$$

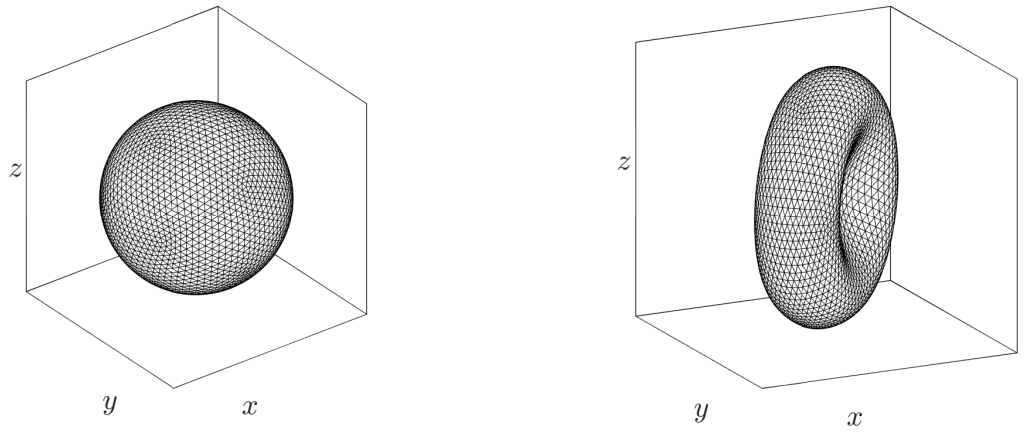

(a) (b)

Fig. 2: (a) The spherical and (b) biconcave meshes used in this work. These discretizations have 5120 triangles composed of 2562 Lagrangian nodes.

In this work Equations (33) and (34) are solved using the incompressible lattice Boltzmann method (LBM) [104]. In the incompressible LBM the fluid is modeled as a system of discrete particles whose distribution function, f, evolves based on the lattice Boltzmann equation (LBE) given by:

$$f_i(\mathbf{x}+\mathbf{c}_i\delta t, t+\delta t) - f_i(\mathbf{x},t) = \Omega_i(f),\ i = 0,1,\ldots,N \tag{35}$$

where Ω describes the collisions between particles, δt is the time step, $N+1$ is the number of discrete velocities in the model, $\mathbf{c}_i$ is the i^{th} discrete velocity, and f_i is the distribution function associated with the i^{th} velocity.

The macroscopic variables associated with Equations (33) and (34) are computed from moments of the distribution function as follows:

$$\delta\rho = \sum_{i=0}^{N} f_i \qquad\qquad \mathbf{j} = \rho_0\mathbf{v} = \sum_{i=0}^{N} f_i\mathbf{c}_i \tag{36}$$

where ρ_0 is the reference density and $\delta\rho$ denotes the density fluctuations so that $\rho = \rho_0 + \delta\rho$ is the local density. The lattice and collision operator are constructed so that the mass density, ρ, and the components of the momentum density, j_x, j_y, and j_z, are conserved up to $\mathscr{O}(Ma^2)$, and thus,

in the low Ma regime, the macroscopic variables are approximate solutions of the incompressible Navier-Stokes equations [105].

The LBE is derived from the discrete velocity Boltzmann equation when the discretization of space, time, and velocity are interrelated through the selection of a lattice constant, c, as follows:

$$\delta t = \frac{\Delta x}{c} \qquad\qquad \mathbf{c}_i = c\ \mathbf{e}_i. \tag{37}$$

The lattice constant is related to the speed of sound in the medium as follows:

$$c_s = \frac{1}{\sqrt{3}} c. \tag{38}$$

There are a number of possible lattices for the LBE, with each lattice designated by DmQn, where m indicates the number of spatial dimensions and n indicates the number of discrete velocities. In this work we use the D3Q19 lattice, which is a three dimensional lattice with 19 discrete velocities. The direction of the discrete velocities $\mathbf{e}_i$ are given as:

$[\mathbf{e}_0, \mathbf{e}_1, \mathbf{e}_2, \ldots, \mathbf{e}_{18}]^{\mathrm{T}} =$

$$\begin{pmatrix} 0 & 1 & -1 & 0 & 0 & 0 & 0 & 1 & 1 & -1 & -1 & 1 & -1 & 1 & -1 & 0 & 0 & 0 & 0 \\ 0 & 0 & 0 & 1 & -1 & 0 & 0 & 1 & -1 & 1 & -1 & 0 & 0 & 0 & 0 & 1 & 1 & -1 & -1 \\ 0 & 0 & 0 & 0 & 0 & 1 & -1 & 0 & 0 & 0 & 0 & 1 & 1 & -1 & -1 & 1 & -1 & 1 & -1 \end{pmatrix}.$$

For the above $\mathbf{e}_i$, a choice of $c = 1$ m/s results in the particle distribution functions moving exactly one grid point at each time step, eliminating the need for interpolation.

In this work, the collision term, Ω, in Equation (35) is approximated using the multiple relaxation time (MRT) collision model discussed in [106]. The MRT collision operator maps the distribution function to the physical moment space of the system where each moment is then relaxed to its corresponding equilibrium moment. The moments are linear combinations of the components of the distribution function, which can be written as $\mathbf{m} = \mathbf{M}\mathbf{f}$ where, for the D3Q19 lattice the

transformation matrix, **M**, is [106]:

$$\begin{pmatrix}
1 & 1 & 1 & 1 & 1 & 1 & 1 & 1 & 1 & 1 & 1 & 1 & 1 & 1 & 1 & 1 & 1 & 1 & 1 \\
-30 & -11 & -11 & -11 & -11 & -11 & -11 & 8 & 8 & 8 & 8 & 8 & 8 & 8 & 8 & 8 & 8 & 8 & 8 \\
12 & -4 & -4 & -4 & -4 & -4 & -4 & 1 & 1 & 1 & 1 & 1 & 1 & 1 & 1 & 1 & 1 & 1 & 1 \\
0 & 1 & -1 & 0 & 0 & 0 & 0 & 1 & -1 & 1 & -1 & 1 & -1 & 1 & -1 & 0 & 0 & 0 & 0 \\
0 & -4 & 4 & 0 & 0 & 0 & 0 & 1 & -1 & 1 & -1 & 1 & -1 & 1 & -1 & 0 & 0 & 0 & 0 \\
0 & 0 & 0 & 1 & -1 & 0 & 0 & 1 & 1 & -1 & -1 & 0 & 0 & 0 & 0 & 1 & -1 & 1 & -1 \\
0 & 0 & 0 & -4 & 4 & 0 & 0 & 1 & 1 & -1 & -1 & 0 & 0 & 0 & 0 & 1 & -1 & 1 & -1 \\
0 & 0 & 0 & 0 & 0 & 1 & -1 & 0 & 0 & 0 & 0 & 1 & 1 & -1 & -1 & 1 & 1 & -1 & -1 \\
0 & 0 & 0 & 0 & 0 & -4 & 4 & 0 & 0 & 0 & 0 & 1 & 1 & -1 & -1 & 1 & 1 & -1 & -1 \\
0 & 2 & 2 & -1 & -1 & -1 & -1 & 1 & 1 & 1 & 1 & 1 & 1 & 1 & 1 & -2 & -2 & -2 & -2 \\
0 & -4 & -4 & 2 & 2 & 2 & 2 & 1 & 1 & 1 & 1 & 1 & 1 & 1 & 1 & -2 & -2 & -2 & -2 \\
0 & 0 & 0 & 1 & 1 & -1 & -1 & 1 & 1 & 1 & 1 & -1 & -1 & -1 & -1 & 0 & 0 & 0 & 0 \\
0 & 0 & 0 & -2 & -2 & 2 & 2 & 1 & 1 & 1 & 1 & -1 & -1 & -1 & -1 & 0 & 0 & 0 & 0 \\
0 & 0 & 0 & 0 & 0 & 0 & 0 & 1 & -1 & -1 & 1 & 0 & 0 & 0 & 0 & 0 & 0 & 0 & 0 \\
0 & 0 & 0 & 0 & 0 & 0 & 0 & 0 & 0 & 0 & 0 & 0 & 0 & 0 & 0 & 1 & -1 & -1 & 1 \\
0 & 0 & 0 & 0 & 0 & 0 & 0 & 0 & 0 & 0 & 0 & 1 & -1 & -1 & 1 & 0 & 0 & 0 & 0 \\
0 & 0 & 0 & 0 & 0 & 0 & 0 & 1 & -1 & 1 & -1 & -1 & 1 & -1 & 1 & 0 & 0 & 0 & 0 \\
0 & 0 & 0 & 0 & 0 & 0 & 0 & -1 & -1 & 1 & 1 & 0 & 0 & 0 & 0 & 1 & -1 & 1 & -1 \\
0 & 0 & 0 & 0 & 0 & 0 & 0 & 0 & 0 & 0 & 0 & 1 & 1 & -1 & -1 & -1 & -1 & 1 & 1
\end{pmatrix} \tag{39}$$

The resulting moment vector **m** can be written in the following form:

$$\mathbf{m} = [\delta\rho, e, \varepsilon, j_x, q_x, j_y, q_y, j_z, q_z, 3p_{xx}, 3\pi_{xx}, p_{ww}, \pi_{ww}, p_{xy}, p_{yz}, p_{xz}, m_x, m_y, m_z]^{\mathrm{T}}. \tag{40}$$

The moments, ρ, j_x, j_y, and j_z are the conserved variables of the hydrodynamic equations computed using Equation (36), e and ε are related to the kinetic energy and the square of the kinetic energy respectively, q_x, q_y, and q_z are related to the energy flux, $3p_{xx}$, p_{ww}, p_{xy}, p_{yz}, and p_{xz} are the components of the traceless viscous stress tensor, and π_{xx}, π_{ww}, m_x, m_y, and m_z are higher order moments [106].

The equilibrium moments of the non-conserved moments are functions of the conserved moments ρ, j_x, j_y, and j_z given by:

$$\begin{gathered} e^{\mathrm{eq}} = -11\rho + \frac{19}{\rho_0}\left(j_x^2 + j_y^2 + j_z^2\right) \qquad \varepsilon^{\mathrm{eq}} = w_\varepsilon \rho + \frac{w_{\varepsilon j}}{\rho}\left(j_x^2 + j_y^2 + j_z^2\right) \\ q_x^{\mathrm{eq}} = -\frac{2}{3} j_x \qquad q_y^{\mathrm{eq}} = -\frac{2}{3} j_y \qquad q_z^{\mathrm{eq}} = -\frac{2}{3} j_z \\ p_{xx}^{\mathrm{eq}} = \frac{1}{3\rho_0}\left[2j_x^2 - \left(j_y^2 + j_z^2\right)\right] \qquad p_{ww}^{\mathrm{eq}} = \frac{1}{\rho_0}\left(j_x^2 - j_z^2\right) \\ \pi_{xx}^{\mathrm{eq}} = w_{xx} p_{xx}^{\mathrm{eq}} \qquad \pi_{ww}^{\mathrm{eq}} = w_{xx} p_{ww}^{\mathrm{eq}} \\ m_x^{\mathrm{eq}} = m_y^{\mathrm{eq}} = m_z^{\mathrm{eq}} = 0 \end{gathered} \tag{41}$$

where w_ε, $w_{\varepsilon x}$, and w_{xx} are free parameters. In this work we set $w_\varepsilon = 3$, $w_{\varepsilon x} = -5.5$, and $w_{xx} = -0.5$.

With the above discretization, the MRT collision model can be implemented in the following two-step procedure:

$$\begin{aligned} &\text{Collision: } f_i^*(\mathbf{x}) = f_i(\mathbf{x}, t_n) - M_{ij}^{-1} S_{jk}\left[M_{kl} f_l(\mathbf{x}, t_n) - m_k^{eq}(\mathbf{x}, t_n)\right] \\ &\text{Advection: } f_i(\mathbf{x} + \mathbf{c}_i \delta t, t_n + \delta t) = f_i^*(\mathbf{x}),\ i = 0, 1, \ldots, 18\ . \end{aligned} \tag{42}$$

Here m_k^{eq} is the k^{th} equilibrium moment, S_{jk} are the components of the relaxation matrix, $\mathbf{S}$, and M_{jk} are the components of the collision matrix, $\mathbf{M}$. The relaxation matrix, $\mathbf{S}$, is defined as:

$$\mathbf{S} = \mathrm{diag}(s_0, s_1, s_2, s_3, s_4, s_5, s_6, s_7, s_8, s_9, s_{10}, s_{11}, s_{12}, s_{13}, s_{14}, s_{15}, s_{16}, s_{17}, s_{18}). \tag{43}$$

s_0, s_3, s_5, and s_7 correspond to the conserved moments and hence are set equal to zero. In this work, the relaxation parameters $s_4 = s_6 = s_8 = s_9 = s_{11} = s_{13} = s_{14} = s_{15}$ are related to the kinematic viscosity, ν, as follows:

$$\nu = c_s^2 \delta t \left(\frac{1}{s_9} - \frac{1}{2}\right). \tag{44}$$

s_1 is related to the bulk viscosity, η, by:

$$\eta = \frac{2}{3} c_s^2 \delta t \left(\frac{1}{s_1} - \frac{1}{2}\right). \tag{45}$$

The parameters, s_2, s_{10}, s_{12}, s_{16}, s_{17}, s_{18} correspond to higher order moments that do not affect conservation of the hydrodynamic moments and are thus set to 1.8 [106].

To incorporate the forces, $\mathbf{p}(\mathbf{x})$, into the LBM we follow the method described in [107]. First, the momentum computed using Equation (36) is updated as follows:

$$\mathbf{j}'(\mathbf{x}) = \mathbf{j}(\mathbf{x}) + \frac{\delta t}{2}\mathbf{p}(\mathbf{x}) \; . \tag{46}$$

Next, $\mathbf{j}'$ is used to compute the equilibrium moments, $\mathbf{m}^{eq}$, in Equation (42). After computing the equilibrium moments, the momentum is updated once more using:

$$\mathbf{j}''(\mathbf{x}) = \mathbf{j}'(\mathbf{x}) + \frac{\delta t}{2}\mathbf{p}(\mathbf{x}) \tag{47}$$

Finally, $\mathbf{j}''$ is used to update the moments corresponding to the fluid momentum, m_3, m_5, and m_7.

3.1.1 THE MULTIGRID LATTICE BOLTZMANN METHOD

For steady flows the collision and advection steps of the LBM, defined in Equation (42), are conducted iteratively until the solution converges to a stationary flow. The number of iterations required for convergence of the LBM for steady flows is on the order of $\mathcal{O}(N^2)$, where N is the total number of degrees of freedom and thus, for three-dimensional applications solution of the steady-state Navier-Stokes equations using the standard LBM is prohibitively slow. The slow convergence of the iterative LBM is, in part, caused by the slow decay of low frequency errors, and thus a number of multigrid schemes have been proposed for improving the convergence rate of the LBM for steady flows [108, 88]. Multigrid methods accelerate the convergence of iterative schemes by introducing coarse grid levels whereon these low frequency errors can be dampened much more efficiently [109, 110]. In this work we use the full-approximation storage (FAS) multigrid LBM originally proposed by Mavriplis in [88], in which the full nonlinear equations of the LBM are solved on each grid level.

Following Briggs et al. [109], the FAS multigrid algorithm will be developed in the context of a two-grid method for solution of a non-linear system, $A_h(u_h) = f_h$. The residual can be expressed in terms of the non-linear operator, A_h, the source term, f_h, and the current iterative approximation,

v_h^n, as follows:

$$r_h^n(v_h^n) = A_h(v_h^n) - f_h \tag{48}$$

$$= A_h(v_h^n) - A_h(u_h) \tag{49}$$

where we have replaced f_h with $A_h(u_h)$ in going from Equation (48) to Equation (49). The key idea for the two-grid method is to obtain an approximation to the error $e_h = v_h - u_h$ through solution of Equation (49) on the coarse grid, where the equation can be solved more efficiently due to the reduced size of the system.

On the coarse grid we introduce an operator, A_H, a coarse grid solution, u_H, a grid transfer operator for the solution, $\hat{I}_h^H$, and a grid transfer operator for the residual, I_h^H. With these definitions we can write Equation (49) on the coarse grid as follows:

$$I_h^H r_h^n(v_h) = A_H\left(\hat{I}_h^H v_h^n\right) - A_H(u_H). \tag{50}$$

The coarse grid correction equation is obtained from Equation (50) by moving the known quantities $I_h^H r_h^n(v_h)$ and $A_H\left(\hat{I}_h^H v_h^n\right)$ to the right-hand side and moving the term with unknown coarse grid variable, u_H, to the left-hand side, giving us :

$$A_H(u_H) = A_H\left(\hat{I}_h^H v_h\right) - I_h^H r_h^n(v_h). \tag{51}$$

An iterative approximation to Equation (51) is obtained, denoted here as v_H, and is then used to approximate the coarse grid error: $e_H = v_H - \hat{I}_h^H v_h^n$. The coarse grid error is mapped to the fine grid through a grid transfer operator, I_H^h, and is then used to update the fine grid approximation as follows:

$$u_h^{n+1} = u_h^n + I_H^h e_H. \tag{52}$$

The coarse grid correction equation, Equation (51), can be solved by introducing even coarser grid levels, and thus a multigrid method can be defined as the successive application of the two-grid method described above. A multigrid schedule prescribes the order in which the solution procedure moves between grid levels. In this work we employ V-cycles and W-cycles. In a V-cycle the error

equation on coarse grids is solved using two-grid methods until reaching a grid level coarse enough that the solution can be approximated accurately and efficiently. A W-cycle is more complicated and can be defined recursively. When using two grid levels, the W-cycle and V-cycle are identical. A three-grid W-cycle applies the two-grid method twice to solve for the error on the coarse grid, a four grid W-cycle uses two three-grid W-cycles to obtain the coarse grid error, a five grid W-cycle uses two four-grid W-cycles to obtain the coarse grid error, and so on. This process is illustrated for W-cycles with three and four grids in Figure 3.

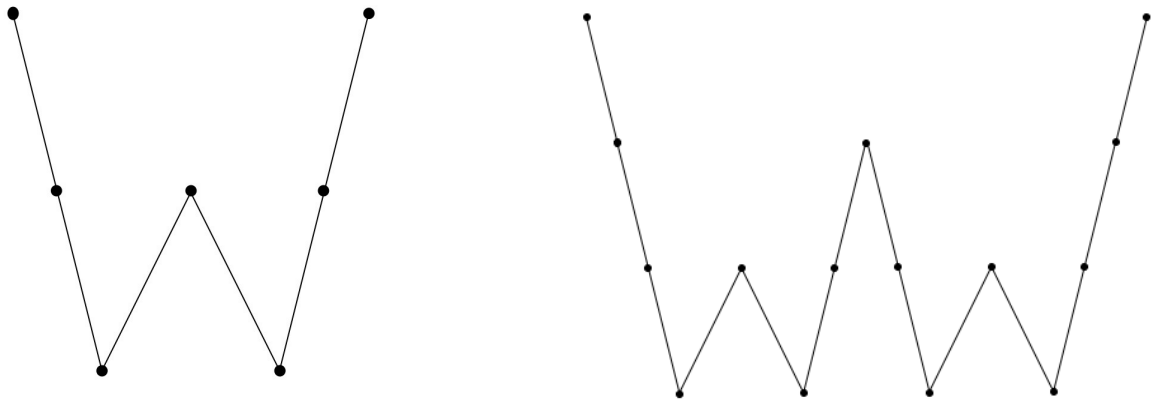

(a) (b)

Fig. 3: Schematics for three-grid and four-grid W-cycles.

In the context of the MRT LBE the i^{th} component of the residual is given by:

$$r_i(\mathbf{f}) = f_i(\mathbf{x}) - f_i(\mathbf{x} - \mathbf{e}_i\Delta x) + M_{ij}^{-1} S_{jk} \left[M_{kl} f_l(\mathbf{x} - \mathbf{e}_i\Delta x) - m_k^{eq}(\mathbf{x} - \mathbf{e}_i\Delta x) \right] \tag{53}$$

where $\mathbf{f} \coloneqq [f_0, f_2, ..., f_{18}]^T$. Following Mavriplis the LBM is modified by introducing under-relaxation after the collision and advection steps in order to improve the error dampening properties of the iterative scheme [88]. On the fine grid the under-relaxation scheme is carried out in

the following three-step procedure:

$$\begin{aligned}
&\text{Collision: } f_i^*(\mathbf{x}) = f_i^n(\mathbf{x}) - M_{ij}^{-1} S_{jk}[M_{kl} f_l(\mathbf{x}) - m_k^{eq}(\mathbf{x})] \\
&\text{Advection: } f_i^{**}(\mathbf{x} + \mathbf{e}_i \Delta x) = f_i^*(\mathbf{x}),\ i = 0, 1, \ldots, 18 \\
&\text{Relaxation: } f_i^{n+1}(\mathbf{x}) = \gamma f_i^{**}(\mathbf{x}) + (1-\gamma) f_i^n(\mathbf{x})
\end{aligned} \tag{54}$$

where γ is a relaxation parameter such that $0 < \gamma < 1$.

On the fine grid the error equation is given by:

$$r_{h,i}(\mathbf{f}_h) = 0. \tag{55}$$

After solving this system for $\mathbf{f}_h$, we compute the fine-grid residual using Equation (53). As in [88] the distribution function and residual are then mapped to the coarse grid using point-wise injection and an averaging operator respectively. On the coarse grid levels, the correction equation is written as:

$$r_{H,i}(\mathbf{f}_H) = D_{H,i} \tag{56}$$

$$D_{H,i} = r_{H,i}(\hat{I}_h^H \mathbf{f}_h) - 2 I_h^H r_{h,i}(\mathbf{f}_h) \tag{57}$$

where $r_{H,i}$ is computed using Equation (53) and $D_{H,i}$ is known as the defect correction. The factor of 2 in the second term on the right side of Equation (57) is used to scale the relaxation parameters on the coarse grids [88]. Equation (56) is solved for $\mathbf{f}_H$ in almost the same manner as Equation (54), with a modification to the relaxation step so that $D_{H,i}$ can be added to the distribution function as follows:

$$\text{Relaxation: } f_i^{n+1}(\mathbf{x}) = \gamma[f_i^{**}(\mathbf{x}) + D_{H,i}(\mathbf{x})] + (1-\gamma) f_i^n(\mathbf{x}). \tag{58}$$

After solving for the error on the coarse grid, the error is either mapped to the fine grid using an averaging operator and then is added to our approximation of the distribution function or mapped to an even coarser grid using point-wise injection, depending on the multigrid schedule.

3.2 THE IMMERSED INTERFACE METHOD

The immersed interface method (IIM), first proposed by Leveque and Li in [111], was developed to solve elliptical PDEs with discontinuities in the coefficients or source term of the PDE. These discontinuities result in discontinuities of the solution and its derivatives, which must be accounted for in the numerical scheme. Three dimensional implementation of the immersed interface method is discussed in detail by Deng et al. in [101], however the present method requires significant modifications due to the incorporation of the transmembrane potential using the method of Hu et al. from [74]. Although the leaky dielectric model requires solution of a Laplace problem across an interface, for the discussion that follows we will consider the more general case of a Poisson problem with a discontinuous source across an interface, Σ, separating a parallelepiped domain into sub-domains, Ω^+ and Ω^-.

The jump in the potential across the interface is equivalent to the transmembrane potential of DeBruin and Krassowska [64] and thus $[\![\psi]\!] = V_m$, where V_m is a function defined along the interface. In [64] it is shown that the transmembrane potential is related to the current density $\sigma\psi$ through Equation 9, re-written here for clarity:

$$\sigma^+ \psi_n^+ = \bar{C}_m \frac{\partial V_m}{\partial t} + \bar{G}_m V_m \tag{59}$$

$$\sigma^- \psi_n^- = \bar{C}_m \frac{\partial V_m}{\partial t} + \bar{G}_m V_m \tag{60}$$

where $\bar{C}_m = \varepsilon_m / d_m$ and $\bar{G}_m = \sigma_M / d_m$ are the dimensional forms of the membrane capacitance and membrane conductivity.

The jump condition $[\![\psi]\!]$ is necessary for the IIM and thus incorporation of the transmembrane potential into IIM requires solution of the temporal ODE given by Equation 9 at each time step. A number of approaches have been proposed for incorporation of the transmembrane potential ODE into the IIM (e.g. [70, 67, 73]). In this work we use the method proposed by Hu et al. in [74] where Equation (9) is solved as a system with the Poisson equation and interface equations. Toward this

end, we subtract Equation (60) from (59) giving us the following expression for $[\![\psi_n]\!]$:

$$[\![\psi_n]\!] = \frac{\bar{C}_m}{\sigma^+}\frac{\partial V_m}{\partial t} + \frac{\bar{G}_m}{\sigma^+}V_m - \frac{\bar{C}_m}{\sigma^-}\frac{\partial V_m}{\partial t} - \frac{\bar{G}_m}{\sigma^-}V_m \tag{61}$$

$$= \left(\frac{1}{\sigma^+} - \frac{1}{\sigma^-}\right)\left(\frac{\bar{C}_m}{\sigma^+}\frac{\partial V_m}{\partial t} + \frac{\bar{G}_m}{\sigma^+}V_m\right). \tag{62}$$

It's important to mention that Equation (62) should not be used for the case when $\sigma_r = 1$ since $\sigma^+ = \sigma^-$ results in the right-hand side being 0, eliminating the time dependence from the problem. For simulations in which $\sigma_r = 1$ a different discretization of Equation (9), such as the method proposed by Kolahdouz and Salac in [70], should be used.

The current density is continuous across the membrane giving us $[\![\sigma\psi]\!] = 0$ and thus, the complete system can be written as:

$$\Delta\psi^+ = \frac{f}{\sigma^+} \quad \text{in} \quad \Omega^+ \tag{63}$$

$$\Delta\psi^- = \frac{f}{\sigma^-} \quad \text{in} \quad \Omega^- \tag{64}$$

$$[\![\psi]\!] = V_m \quad \text{on} \quad \Sigma \tag{65}$$

$$[\![\psi_n]\!] = \left(\frac{1}{\sigma^+} - \frac{1}{\sigma^-}\right)\left(\frac{\bar{C}_m}{\sigma^+}\frac{\partial V_m}{\partial t} + \frac{\bar{G}_m}{\sigma^+}V_m\right) \quad \text{on} \quad \Sigma \tag{66}$$

$$[\![\sigma\psi_n]\!] = 0 \quad \text{on} \quad \Sigma. \tag{67}$$

IIM can be used to obtain a numerical solution of Equations (63) - (67) using the standard seven-point finite difference stencil and a correction term.

3.2.1 THE DISCRETE IIM EQUATIONS

The Poisson problem, given by Equations (63) and (64), is solved in a parallelepiped domain $\Omega^+ \cup \Omega^- = [a_x, b_x] \times [a_y, b_y] \times [a_z, b_z]$ discretized using a uniform grid with $\Delta x = \Delta y = \Delta z$. On this grid the Poisson equation is discretized using the seven-point Laplacian:

$$\frac{\psi_{i+1,j,k} + \psi_{i-1,j,k} + \psi_{i,j+1,k} + \psi_{i,j-1,k} + \psi_{i,j,k+1} + \psi_{i,j,k-1} - 4\psi_{i,j,k}}{\Delta x^2} = \bar{f}_{i,j,k} + c_{i,j,k} \tag{68}$$

where the subscript i, j, k indicates a function evaluation at (x_i, y_j, z_k), $\bar{f}_{i,j,k} = \frac{f^+_{i,j,k}}{\sigma^+}$ in Ω^+, $\bar{f}_{i,j,k} =$

$\frac{f^-_{i,j,k}}{\sigma^-}$ in Ω^-, and $c_{i,j,k}$ is a correction term that accounts for jumps across the interface. At grid points where the interface intersects the seven-point stencil the correction term term accounts for the jump in the solution and its derivatives across the interface. In this work the correction term is computed using the method discussed in [101], which is outlined in Appendix B.2. At grid points where the interface does not intersect the seven-point stencil, the correction term is not needed and thus we have $c_{i,j,k} = 0$.

The interface conditions, given by Equations (65)-(67), are solved on a set of discrete points located on the interface, which we will refer to as control points. The interface is defined by a levelset function, $\phi(x,y,z)$, where $\phi < 0$ indicates that a point is inside the interface, $\phi = 0$ indicates that a point is on the interface, and $\phi > 0$ indicates that a point is outside the interface. Based on the levelset function, each grid point is labelled as a regular or irregular point, with irregular points defined as points for which a correction term is required due to the intersection between the interface and the stencil of the seven-point Laplacian. At each irregular point IIM requires a nearby point located on the interface. Following Deng et al. [101], we select the projection of the irregular points onto the interface. The projection points corresponding to irregular points on the outside of the interface are the control points that are used to discretize the interface functions in Equations (65)-(67).

We will now write the discrete form of Equations (63)-(67) in terms of the solution vector, Ψ defined at the grid points, and the jump condition vectors $W = [\![\psi]\!]$ and $G = [\![\psi_n]\!]$ defined at the control points. In [111] it is shown that, to second order, the correction term, $c_{i,j,k}$, can be written as a linear combination of the values of the jump conditions W and G. Thus, if we let L denote the matrix representation of the seven-point Laplacian, C_1 denote the linear dependence of $c_{i,j,k}$ on $[\![\psi]\!]$, C_2 denote the linear dependence of $c_{i,j,k}$ on $[\![\psi_n]\!]$, and F denote $\bar{f}$, then Equation (63) can be written in matrix form as:

$$L\Psi + C_1 W + C_2 G = F. \tag{69}$$

The discrete form of the jump condition $[\![\sigma\psi_n]\!] = 0$ can be written as:

$$\sigma^+\Psi_n^+ - \sigma^-\Psi_n^- = 0 \tag{70}$$

where Ψ_n^+ and Ψ_n^- are second order approximations of ψ_n^+ and ψ_n^- defined on the control points.

Computation of Ψ_n^+ and Ψ_n^- is done using the method proposed in [101] which is outlined in Appendix B.2. In [112] it is shown that Equation (70) can be written as a linear combination of Ψ and G, which we express as follows:

$$E\Psi + DG = 0. \tag{71}$$

The last equation left to be discretized is the equation for the transmembrane potential, given by Equation (62). In this work Equation (62) is discretized using the Crank-Nicholson scheme proposed by Hu et al. in [74]. With the Crank-Nicholson discretization, the discrete equation, written in terms of the discrete jump conditions W and G, is given by:

$$\left(\frac{1}{\sigma^+} - \frac{1}{\sigma^-}\right)\left[\bar{C}_m \frac{W - W^n}{\Delta t} + \bar{G}_m \frac{W + W^n}{2}\right] = \frac{G + G^n}{2}. \tag{72}$$

Here W^n and G^n denote the discrete jump conditions at $t = t^n$, which are known and W and G denote the discrete jump conditions at $t = t^{n+1}$, which are unknown. Rearranging the equations so that the known quantities, W^n and G^n, appear on the right hand side and the unknown quantities, W and G, appear on the left gives us:

$$\left(\frac{1}{\sigma^+} - \frac{1}{\sigma^-}\right)\left(\frac{\bar{C}_m}{\Delta t} + \frac{\bar{G}_m}{2}\right) W - \frac{1}{2} G = \left(\frac{1}{\sigma^+} - \frac{1}{\sigma^-}\right)\left(\frac{\bar{C}_m}{\Delta t} - \frac{\bar{G}_m}{2}\right) W^n + \frac{G^n}{2} \tag{73}$$

where the right hand side is completely known. Equation (73) results in $O\left(\Delta t^2\right)$ temporal discretization of Equation (62).

If we make the following substitutions:

$$\alpha = \left(\frac{1}{\sigma^+} - \frac{1}{\sigma^-}\right)\left(\frac{\bar{C}_m}{\Delta t} + \frac{\bar{G}_m}{2}\right) \tag{74}$$

$$\beta = -\frac{1}{2} \tag{75}$$

$$F_0 = \left(\frac{1}{\sigma^+} - \frac{1}{\sigma^-}\right)\left(\frac{\bar{C}_m}{\Delta t} - \frac{\bar{G}_m}{2}\right) W^n + \frac{G^n}{2}. \tag{76}$$

Equation (73) can be succinctly written as:

$$\alpha W + \beta G = F_0. \tag{77}$$

Appending this equation to the discretization of Poisson's Equation, given by Equation (69), and the discretization of the known jump condition for $[\![\sigma\psi_n]\!]$, given by Equation (71) gives us the following system of equations:

$$L\Psi + C_1 W + C_2 G = F \tag{78}$$

$$E\Psi + DG = 0 \tag{79}$$

$$\alpha W + \beta G = F_0. \tag{80}$$

The system given by Equations (78)-(80) has 3 equations and 3 unknowns and thus, provided that the requisite inverse matrices exist, we can reduce this to a single matrix equation. First, we solve Equation (80) for G giving us:

$$G = \frac{1}{\beta}\left(F_0 - \alpha W\right). \tag{81}$$

Next we solve Equation (78) for Ψ giving us:

$$\Psi = L^{-1}\left(F - C_1 W - C_2 G\right). \tag{82}$$

Inserting Equations (81) and (82) into Equation (79) gives us the following equation for W:

$$\begin{aligned} -\left[EL^{-1}\left(C_1 - \frac{\alpha}{\beta}C_2\right) + \frac{\alpha}{\beta}D\right]W &= -EL^{-1}\left(F - \frac{1}{\beta}C_2 F_0\right) - \frac{1}{\beta}DF_0 \\ &= \bar{V} \end{aligned} \tag{83}$$

3.2.2 ITERATIVE SOLUTION OF THE DISCRETE IIM EQUATIONS

As in the standard IIM, Equation (83) is solved iteratively using GMRES. For an iterative approximation to W, which we will denote as W^*, we can obtain the current iterative approximation to G as:

$$G(W^*) = \frac{1}{\beta}\left(F_0 - \alpha W^*\right) \tag{84}$$

where the notation $G(W^*)$ emphasizes the dependence on W^*. Similarly, we can define the current

approximation to Ψ as:

$$\Psi(W^*) = L^{-1}\left[F - C_1 W^* - \frac{1}{\beta} C_2 \left(F_0 - \alpha W^*\right)\right] \tag{85}$$

where we have used Equation (84) to represent $G(W^*)$.

The matrix multiplications in Equation (83) are computed without constructing the required matrices through introduction of the residual, $R(W^*)$ defined as:

$$R(W^*) = -\left[\sigma^+ \Psi_n^+(W^*) - \sigma^- \Psi_n^-(W^*)\right] \tag{86}$$

$$= -E\Psi(W^*) - DG(W^*). \tag{87}$$

Computation of the right hand side, $\bar{V}$, is given by inserting $G(0) = \frac{1}{\beta} F_0$ and $\Psi(0) = L^{-1}\left(F - \frac{1}{\beta} C_2 F_0\right)$ into $R(0)$ as follows:

$$R(0) = -\left[\sigma^+ \Psi_n^+(0) - \sigma^- \Psi_n^-(0)\right] \tag{88}$$

$$= -E\Psi(0) - DG(0) \tag{89}$$

$$= -EL^{-1}\left(F - \frac{1}{\beta} C_2 F_0\right) - \frac{1}{\beta} D F_0 \tag{90}$$

$$= \bar{V}. \tag{91}$$

Computation of the matrix-vector multiplication on the left hand side of Equation (83) can be obtained by evaluating the residual $R(W^*)$:

$$\begin{aligned} R(W^*) &= -E\Psi(W^*) - DG(W^*) \\ &= -EL^{-1}\left[F - C_1 W^* - \frac{1}{\beta} C_2 \left(F_0 - \alpha W^*\right)\right] - \frac{1}{\beta} D\left(F_0 - \alpha W^*\right) \\ &= -EL^{-1}\left(F - \frac{1}{\beta} F_0\right) - \frac{1}{\beta} D F_0 + EL^{-1}\left(C_1 W^* - \frac{\alpha}{\beta} C_2 W^*\right) + \frac{\alpha}{\beta} D W^* \\ &= \bar{V} + \left[EL^{-1}\left(C_1 - \frac{\alpha}{\beta} C_2\right) + \frac{\alpha}{\beta} D\right] W^* \end{aligned}$$

and thus we have:

$$-\left[EL^{-1}\left(C_1 - \frac{\alpha}{\beta} C_2\right) + \frac{\alpha}{\beta} D\right] W^* = \bar{V} - R(W^*). \tag{92}$$

With the matrix computations above the algorithm for solving Equations (63)-(67) can be summarized as follows:

1. Compute F_0 from Equation (76) using values of W and G from previous time step
2. Compute $\bar{V}$
   i) Apply one step of the Immersed Interface Method with $W = 0$ and $G = G(0) = \frac{1}{\beta}F_0$ to obtain $\Psi(0)$
   ii) Use $\Psi(0)$ and $G(0)$ to compute $\Psi_n^+(0)$ and $\Psi_n^-(0)$
   iii) Compute $\bar{V} = R(0)$ using Equation (88)
3. While $R(W^*) >$ tol:
   i) Apply one step of the Immersed Interface Method with $W = W^*$ and $G = G(W^*)$ to obtain $\Psi(W^*)$
   ii) Compute $G(W^*)$ using Equation (84)
   iii) Use $\Psi(W^*)$ and $G(W^*)$ to compute $\Psi_n^+(W^*)$ and $\Psi_n^-(W^*)$
   iv) Compute $R(W^*)$ using Equation (86).

3.2.3 COMPUTATION OF THE ELECTRIC FIELD

The electric field is computed from the electric potential, ψ, using the scheme proposed in [113] where a correction term is added to the standard second order central finite difference scheme for first derivatives so that second order accuracy is retained even when the interface intersects the finite difference stencil. Here, the correction term is derived for the case where $(x_{i+1}, y_j, z_k) \in \Omega^+$ and $(x_{i-1}, y_j, z_k), (x_i, y_j, z_k) \in \Omega^-$ however other cases are derived in a similar manner. Since $(x_i, y_j, z_k) \in \Omega^-$ we want to compute E_x^-, and thus our correction term must account for the fact that $\psi(x_{i+1}, y_j, z_k) = \psi^+(x_{i+1}, y_j, z_k)$.

Let $\widetilde{\psi}$ be an extension of ψ^- from Σ^- to Σ^+ so that $[\![\widetilde{\psi}]\!] = 0$, $[\![\nabla\widetilde{\psi}]\!] = 0$, and $[\![\mathrm{He}(\widetilde{\psi})]\!] = 0$. We

can write the central difference scheme for first derivatives as follows:

$$\begin{aligned} E_x^- \left(\mathbf{x}_{ijk}\right) &= -\frac{\psi^+_{i+1,j,k} - \psi^-_{i-1,j,k}}{2\Delta x} + \frac{\widetilde{\psi}_{i+1,j,k} - \widetilde{\psi}_{i+1,j,k}}{2\Delta x} \\ &= -\frac{\widetilde{\psi}_{i+1,j,k} - \psi^-_{i-1,j,k}}{2\Delta x} + \frac{\widetilde{\psi}_{i+1,j,k} - \psi^+_{i+1,j,k}}{2\Delta x} \\ &= -\frac{\partial \psi}{\partial x}^- + O(\Delta x^2) + \frac{\widetilde{\psi}_{i+1,j,k} - \psi^+_{i+1,j,k}}{2\Delta x} \end{aligned}$$

where we have used the fact that $\frac{\widetilde{\psi}_{i+1,j,k} - \psi^-_{i-1,j,k}}{2\Delta x}$ is a second order approximation to $\frac{\partial \psi}{\partial x}^-$ at (x_i, y_j, z_k). The term $\frac{\widetilde{\psi}_{i+1,j,k} - \psi^+_{i+1,j,k}}{2\Delta x}$ is the correction term for $E_x^- \left(\mathbf{x}_{ijk}\right)$.

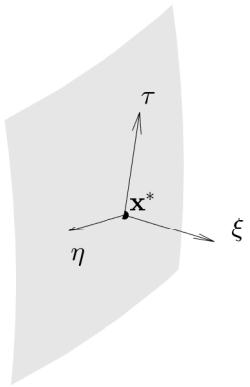

Fig. 4: The local coordinates at the interface point, $\mathbf{X}^*$. $\hat{\xi}$ is normal to the surface at $\mathbf{X}^*$. $\hat{\eta}$ and $\hat{\tau}$ span the plane tangent to the surface at $\mathbf{X}^*$.

Since the interface lies between (x_{i+1}, y_j, z_k) and (x_i, y_j, z_k) there exists a point on the interface, denoted here as $\mathbf{X}^*$, corresponding to the point (x_{i+1}, y_j, z_k). Using Taylor's theorem we can expand

$\widetilde{\psi}_{i+1,j,k}$ and $\psi^+_{i+1,j,k}$ about $\mathbf{X}^*$ as follows:

$$\widetilde{\psi}_{i+1,j,k} = \widetilde{\psi}_* + (\mathbf{x}_{i+1} - \mathbf{X}^*)^T \nabla \widetilde{\psi}_* + \frac{1}{2} (\mathbf{x}_{i+1} - \mathbf{X}^*)^T \, \mathrm{He}(\widetilde{\psi}_*) \, (\mathbf{x}_{i+1} - \mathbf{X}^*)$$
$$\psi^+_{i+1,j,k} = \psi^+_* + (\mathbf{x}_{i+1} - \mathbf{X}^*)^T \nabla \psi^+_* + \frac{1}{2} (\mathbf{x}_{i+1} - \mathbf{X}^*)^T \, \mathrm{He}(\psi^+_*) \, (\mathbf{x}_{i+1} - \mathbf{X}^*)$$

where the shorthand notations $\mathbf{x}_{i+1} = (x_{i+1}, y_j, z_k)$, $\widetilde{\psi} = \widetilde{\psi}(\mathbf{X}^*)$, and $\psi^+ = \psi^+(\mathbf{X}^*)$ are used. Introducing local coordinates, (ξ, η, τ), depicted in Figure 4, at $\mathbf{X}^*$ and defining $(\mathbf{x}_{i+1} - \mathbf{X}^*) = (\xi_{i+1}, \eta_{i+1}, \tau_{i+1})$, the expansion for $\psi^+_{i+1,j,k}$ can be re-written as:

$$\begin{aligned}\psi^+_{i+1,j,k} = \psi^+ &+ \xi_{i+1}\psi^+_\xi + \eta_{i+1}\psi^+_\eta + \tau_{i+1}\psi^+_\tau + \frac{1}{2}\xi^2_{i+1}\psi^+_{\xi\xi} + \frac{1}{2}\eta^2_{i+1}\psi^+_{\eta\eta} \\ &+ \frac{1}{2}\tau_{i+1}\psi^+_{\tau\tau} + \xi_{i+1}\eta_{i+1}\psi^+_{\xi\eta} + \xi_{i+1}\tau_{i+1}\psi^+_{\xi\tau} + \eta_{i+1}\tau_{i+1}\psi^+_{\eta\tau}.\end{aligned}$$

Since $\widetilde{\psi}$ is an extension of ψ^- across the interface and $\mathbf{X}^*$ is on the interface, we have that $\widetilde{\psi}(\mathbf{X}^*) = \psi^-(\mathbf{X}^*)$ and thus, in the local coordinates, the expansion of $\widetilde{\psi}_{i+1,j,k}$ is given by:

$$\begin{aligned}\widetilde{\psi}_{i+1,j,k} = \psi^- &+ \xi_{i+1}\psi^-_\xi + \eta_{i+1}\psi^-_\eta + \tau_{i+1}\psi^-_\tau + \frac{1}{2}\xi^2_{i+1}\psi^-_{\xi\xi} + \frac{1}{2}\eta^2_{i+1}\psi^-_{\eta\eta} \\ &+ \frac{1}{2}\tau_{i+1}\psi^-_{\tau\tau} + \xi_{i+1}\eta_{i+1}\psi^-_{\xi\eta} + \xi_{i+1}\tau_{i+1}\psi^-_{\xi\tau} + \eta_{i+1}\tau_{i+1}\psi^-_{\eta\tau}.\end{aligned}$$

Subtracting the expansion of $\widetilde{\psi}_{i+1,j,k}$ from the expansion of $\psi^+_{i+1,j,k}$ gives us the following result:

$$\begin{aligned}\psi^+_{i+1,j,k} - \widetilde{\psi}_{i+1,j,k} = [\![\psi]\!] &+ \xi_{i+1}[\![\psi_\xi]\!] + \eta_{i+1}[\![\psi_\eta]\!] + \tau_{i+1}[\![\psi_\tau]\!] + \frac{1}{2}\xi^2_{i+1}[\![\psi_{\xi\xi}]\!] + \frac{1}{2}\eta^2_{i+1}[\![\psi_{\eta\eta}]\!] \\ &+ \frac{1}{2}\tau_{i+1}[\![\psi_{\tau\tau}]\!] + \xi_{i+1}\eta_{i+1}[\![\psi_{\xi\eta}]\!] + \xi_{i+1}\tau_{i+1}[\![\psi_{\xi\tau}]\!] + \eta_{i+1}\tau_{i+1}[\![\psi_{\eta\tau}]\!]\end{aligned}$$

where the jumps, $[\![\cdot]\!]$, are understood to be evaluated at $\mathbf{X}^*$. The jump conditions are given by Equations (158)-(167). In practice, the jumps are computed during the Immersed Interface computation and thus, the correction term adds minimal cost to the scheme.

3.3 ELECTRIC FORCES

Electrical forces arise due to a jump in the electric stresses across the interface. The electrical forces are incorporated into the immersed boundary framework as an additional force in Equation (113). For the leaky dielectric fluids considered in this work the electric stress is given by Equation (3) and thus, the force arising from the jump in electric stress is given by:

$$\mathbf{f}_e = \left(\tau_E^+ - \tau_E^-\right)\hat{\mathbf{n}} \tag{93}$$

$$= \left\{\varepsilon^+\left[\mathbf{E}^+\left(\mathbf{E}^+\right)^{\mathrm{T}} - \frac{1}{2}\mathbf{E}^+\cdot\mathbf{E}^+\mathbb{I}\right] - \varepsilon^-\left[\mathbf{E}^-\left(\mathbf{E}^-\right)^{\mathrm{T}} - \frac{1}{2}\mathbf{E}^-\cdot\mathbf{E}^-\mathbb{I}\right]\right\}\hat{\mathbf{n}} \tag{94}$$

where $\mathbf{E}^+$ is the electric field outside the capsule and $\mathbf{E}^-$ is the electric field inside the capsule.

The electric potential and electric field are computed at the Eulerian grid points, requiring interpolation of $\mathbf{E}^+$ and $\mathbf{E}^-$ to the Lagrangian nodes. The following discussion will focus on computation of E_x^+, however, the computation of E_y^+, E_z^+, E_x^-, E_y^-, and E_z^- are done in an analogous manner. An interpolation of E_x^+ at the Lagrangian node, $\mathbf{X}_\ell$, is obtained from a linear combination of the values of E_x^+ at nearby Eulerian nodes, $\mathbf{x}_{ijk} \in \Omega^+$, giving us the following expression:

$$E_x^+(\mathbf{X}_\ell) = \sum_{|\mathbf{X}_\ell - \mathbf{x}_{ijk}| \le R} \alpha_{ijk} E_x^+(\mathbf{x}_{ijk}) \tag{95}$$

where R is a user-defined radius and the interpolating coefficients α_{ijk} are as yet unknown. To obtain the coefficients, α_{ijk}, we expand E_x^+ in a Taylor series approximation about $\mathbf{X}_\ell$ giving us the following equation:

$$E_x^+(\mathbf{X}_\ell) = \sum_{|\mathbf{X}_\ell - \mathbf{x}_{ijk}| \le R} \alpha_{ijk}\big\{E_x^+(\mathbf{X}_\ell) + (\mathbf{X}_\ell - \mathbf{x}_{ijk})\cdot\nabla E_x^+(\mathbf{X}_\ell) + (\mathbf{X}_\ell - \mathbf{x}_{ijk})^T H[E_x^+(\mathbf{X}_\ell)](\mathbf{X}_\ell - \mathbf{x}_{ijk}) + \text{H.O.T}\big\}$$

where $H[E_x^+(\mathbf{X}_\ell)]$ represents the Hessian matrix of E_x^+ and H.O.T. represents the higher order terms.

At each Lagrangian node, $\mathbf{X}_\ell$, we compute an orthonormal basis $\{\xi, \eta, \tau\}$, where ξ is normal to the interface at $\mathbf{X}_\ell$ and η and τ are in the plane perpendicular to ξ. We can then write Equation (95)

in terms of the local coordinates of the nearby Euelrian coordiantes, $\mathbf{x}_{ijk}$, denoted $(\xi_{ijk}, \eta_{ijk}, \tau_{ijk})$, as follows:

$$\begin{aligned} E_x^+(\mathbf{X}_\ell) = \sum_{|\mathbf{X}_\ell - \mathbf{x}_{ijk}| \le R} \alpha_{ijk} \big\{ & E_x^+(\mathbf{X}_\ell) + \xi_{ijk}\partial_\xi E_x^+(\mathbf{X}_\ell) + \eta_{ijk}\partial_\eta E_x^+(\mathbf{X}_\ell) + \tau_{ijk}\partial_\tau E_x^+(\mathbf{X}_\ell) \\ & + \xi_{ijk}\eta_{ijk}\partial_{\xi\,\eta} E_x^+(\mathbf{X}_\ell) + \xi_{ijk}\tau_{ijk}\partial_{\xi\,\tau} E_x^+(\mathbf{X}_\ell) + \eta_{ijk}\tau_{ijk}\partial_{\eta\,\tau} E_x^+(\mathbf{X}_\ell) \\ & + \frac{1}{2}\xi_{ijk}^2\partial_{\xi\,\xi} E_x^+(\mathbf{X}_\ell) + \frac{1}{2}\eta_{ijk}^2\partial_{\eta\,\eta} E_x^+(\mathbf{X}_\ell) + \frac{1}{2}\tau_{ijk}^2\partial_{\tau\tau} E_x^+(\mathbf{X}_\ell) + \text{H.O.T} \big\}. \end{aligned}$$

Requiring the right and left sides of the above equation to match to second order gives us the following ten equations:

$$\begin{aligned} \sum \alpha_{ijk} &= 1 & \sum \alpha_{ijk}\xi_{ijk} &= 0 & \sum \alpha_{ijk}\eta_{ijk} &= 0 \\ \sum \alpha_{ijk}\tau_{ijk} &= 0 & \frac{1}{2}\sum \alpha_{ijk}\xi_{ijk}^2 &= 0 & \frac{1}{2}\sum \alpha_{ijk}\eta_{ijk}^2 &= 0 \\ \frac{1}{2}\sum \alpha_{ijk}\tau_{ijk}^2 &= 0 & \sum \alpha_{ijk}\xi_{ijk}\eta_{ijk} &= 0 & \sum \alpha_{ijk}\xi_{ijk}\tau_{ijk} &= 0 \\ & & \sum \alpha_{ijk}\eta_{ijk}\tau_{ijk} &= 0. & & \end{aligned}$$

Assuming that there are N Eulerian points in the Neighborhood, $|\mathbf{X}_\ell - \mathbf{x}_{ijk}| \le R$, we can re-write this as a system of equations for the interpolating coefficients as follows:

$$\begin{pmatrix} 1 & 1 & \dots & 1 & 1 \\ \xi_{ijk_1} & \xi_{ijk_2} & \cdots & \xi_{ijk_{N-1}} & \xi_{ijk_N} \\ \eta_{ijk_1} & \eta_{ijk_2} & \cdots & \eta_{ijk_{N-1}} & \eta_N \\ \tau_{ijk_1} & \tau_{ijk_2} & \cdots & \tau_{ijk_{N-1}} & \tau_N \\ \frac{1}{2}\xi_{ijk_1}^2 & \frac{1}{2}\xi_{ijk_2}^2 & \cdots & \frac{1}{2}\xi_{ijk_{N-1}}^2 & \frac{1}{2}\xi_{ijk_N}^2 \\ \frac{1}{2}\eta_{ijk_1}^2 & \frac{1}{2}\eta_{ijk_2}^2 & \cdots & \frac{1}{2}\eta_{ijk_{N-1}}^2 & \frac{1}{2}\eta_{ijk_N}^2 \\ \frac{1}{2}\tau_{ijk_1}^2 & \frac{1}{2}\tau_{ijk_2}^2 & \cdots & \frac{1}{2}\tau_{ijk_{N-1}}^2 & \frac{1}{2}\tau_{ijk_N}^2 \\ \xi_{ijk_1}\eta_{ijk_1} & \xi_{ijk_2}\eta_{ijk_2} & \cdots & \xi_{ijk_{N-1}}\eta_{ijk_{N-1}} & \xi_{ijk_N}\eta_{ijk_N} \\ \xi_{ijk_1}\tau_{ijk_1} & \xi_{ijk_2}\tau_{ijk_2} & \cdots & \xi_{ijk_{N-1}}\tau_{ijk_{N-1}} & \xi_{ijk_N}\tau_{ijk_N} \\ \eta_{ijk_1}\tau_{ijk_1} & \eta_{ijk_2}\tau_{ijk_2} & \cdots & \eta_{ijk_{N-1}}\tau_{ijk_{N-1}} & \eta_{ijk_N}\tau_{ijk_N} \end{pmatrix} \begin{pmatrix} \alpha_{ijk_1} \\ \alpha_{ijk_2} \\ \vdots \\ \alpha_{ijk_{N-1}} \\ \alpha_{ijk_N} \end{pmatrix} = \begin{pmatrix} 1 \\ 0 \\ 0 \\ 0 \\ 0 \\ 0 \end{pmatrix}. \qquad (96)$$

In the system above the coefficient α_{ijk_m} corresponds to the mth term in the sum defined by Equation (95). Typically, $N > 10$ and the over-determined system is solved in the least squares sense. In practice we select a maximum of $N = 27$, which results in second order accurate interpolation of the electric field. The interpolation of E_y^+ and E_z^+ are done in an identical manner. The interpolation of E_x^-, E_y^-, and E_z^- are conducted based on the values at the Eulerian nodes, $\mathbf{x}_{ijk} \in \Omega^-$.

3.4 ELASTIC FORCES

The elastic forces are computed at the Lagrangian nodes of the capsule mesh using the linear finite element method proposed by Charrier et al. in [103], which has been used in a number of capsule deformation models [44, 83, 55, 84]. The elastic forces arise due to planar deformation of the individual triangular elements away from their reference configuration. To facilitate a comparison between the current and reference configurations of the elements, each deformed triangular element is mapped into a common plane with its initial configuration as illustrated in Figure 5. From here, the in-plane displacements, u_x and u_y, can be easily computed at each vertex of the triangle.

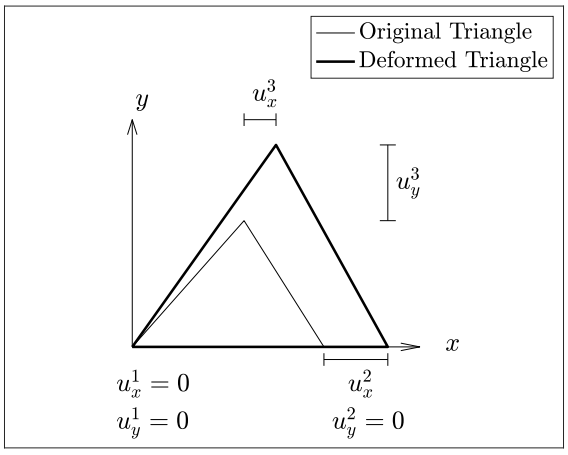

Fig. 5: The initial and current configurations of a triangular element.

An expression for the nodal forces, P_x^i and P_y^i, is obtained via the principle of virtual work for a triangular element, which in terms of the virtual displacements, δu_x^i and δu_y^i, can be expressed as:

$$\delta W_e = \sum_{i=1}^{3} \left(\delta u_x^i P_x^i + \delta u_y^i P_y^i \right) \tag{97}$$

where, as in Figure 5, we use the superscripts $i = 1,2,3$ to label quantities defined at the three vertices of the triangle.

The work due to in-plane stretches can be expressed in terms of a constitutive law describing the strain energy per unit area of the element. In this work the areal strain energy density is assumed to be a function of the principle stretch ratios, λ_1 and λ_2, and is given by either Equation (13) or Equation (14) for neo-Hookean or Skalak membranes respectively. The stretch ratios are constant on a given element and thus the virtual work for an element is given by $\delta W_e = A_o \delta W$ where A_0 is the initial area of the element and δW is the first variation of the selected strain energy law.

The first variation of the strain energy function, δW, is computed using the chain rule resulting in the following expression for virtual work of a triangular element due to displacements, δu_x^i and δu_y^i:

$$\delta W_e = A_o \sum_{k=1}^{3} \left[\delta u_x^k \left(\frac{\partial \lambda_1}{\partial u_x^k} \frac{\partial W}{\partial \lambda_1} + \frac{\partial \lambda_2}{\partial u_x^k} \frac{\partial W}{\partial \lambda_2} \right) + \delta u_y^k \left(\frac{\partial \lambda_1}{\partial u_y^k} \frac{\partial W}{\partial \lambda_1} + \frac{\partial \lambda_2}{\partial u_y^k} \frac{\partial W}{\partial \lambda_2} \right) \right]. \tag{98}$$

Equating the right hand sides of Equations (97) and (98) and invoking the arbitrary nature of the virtual displacements gives us the following expression for the nodal forces due to in-plane tensions:

$$\begin{aligned} P_x^i &= A_0 \frac{\partial W}{\partial \lambda_1} \frac{\partial \lambda_1}{\partial u_x^i} + A_0 \frac{\partial W}{\partial \lambda_2} \frac{\partial \lambda_2}{\partial u_x^i}, \quad i = 1,2,3 \\ P_y^i &= A_0 \frac{\partial W}{\partial \lambda_1} \frac{\partial \lambda_1}{\partial u_y^i} + A_0 \frac{\partial W}{\partial \lambda_2} \frac{\partial \lambda_2}{\partial u_y^i}, \quad i = 1,2,3. \end{aligned} \tag{99}$$

The forces P_x^i and P_y^i are expressed in terms of the local basis, which is then mapped back to the physical coordinates and added to the node's Lagrangian force term as discussed in in [103]. For a mesh with 5120 triangles, each node is the vertex of 5 or 6 triangles and thus the full elastic force at a given Lagrangian node, $\mathbf{P}_m$, is the sum of the forces at each of these 5 or 6 triangles.

Computation of the derivatives in Equation (99) is done using a linear finite element method,

with linear shape functions, N^1, N^2, and N^3. The shape function, N^1, is defined by:

$$N^1(x,y) = \frac{1}{2A_0}\left[(y^2 - y^3k)x + (x^3 - x^2)y + x^2y^3k - x^3y^2\right] \tag{100}$$

and N^2 and N^3 can be obtained by cycling the indices from $1 \to 2 \to 3 \to 1$. $2A_0$ is the twice the area of the element and is computed as follows:

$$2A_0 = |(y^2 - y^3)x^1 + (x^3 - x^2)y^1 + x^2y^3 - x^3y^2|. \tag{101}$$

The spatial dependence of the displacement on the element can be expressed as follows:

$$\begin{aligned} u_x(x,y) &= N^1(x,y)u_x^1 + N^2(x,y)u_x^2 + N^3(x,y)u_x^3 \\ u_y(x,y) &= N^1(x,y)u_y^1 + N^2(x,y)u_y^2 + N^3(x,y)u_y^3. \end{aligned} \tag{102}$$

The only remaining quantities needed for computation of the elastic forces are the principle stretch ratios, λ_1 and λ_2. These are obtained from the eigenvalues of the two-dimensional right Cauchy-Green tensor, $\mathbf{G}$, whose components are given by:

$$G_{11} = \left(1 + \frac{\partial u_x}{\partial x}\right)^2 + \left(\frac{\partial u_y}{\partial x}\right)^2 \tag{103}$$

$$G_{22} = \left(1 + \frac{\partial u_y}{\partial y}\right)^2 + \left(\frac{\partial u_x}{\partial y}\right)^2 \tag{104}$$

$$G_{21} = G_{12} = \left(1 + \frac{\partial u_x}{\partial x}\right)\left(\frac{\partial u_y}{\partial y}\right) + \left(1 + \frac{\partial u_y}{\partial x}\right)\left(\frac{\partial u_x}{\partial y}\right). \tag{105}$$

The derivatives of the in-plane displacements, u and v, in Equation (105) are computed by differentiating their linear representations given by Equation (102). Finally, the principle stretch ratios are expressed in terms of the components of $\mathbf{G}$ as follows:

$$\begin{aligned} \lambda_1^2 &= \frac{1}{2}\left[G_{11} + G_{22} + \sqrt{(G_{11} - G_{22})^2 + 4G_{12}^2}\right] \\ \lambda_1^2 &= \frac{1}{2}\left[G_{11} + G_{22} - \sqrt{(G_{11} - G_{22})^2 + 4G_{12}^2}\right]. \end{aligned} \tag{106}$$

3.5 BENDING FORCES

The areal bending force density is obtained from Helfrich's bending energy functional, given by Equation (16). In terms of the mean curvature, κ, spontaneous curvature, c_0, Gaussian curvature, κ_g, Laplace-Beltrami operator, Δ_{LB}, and normal vector, $\hat{\mathbf{n}}$, the membrane bending force at the Lagragnian node, $\mathbf{X}_i$, is given by:

$$\mathbf{f}_b(\mathbf{X}_i) = E_B[(2\kappa + c_0)(2\kappa^2 - 2\kappa_g - c_0\kappa) + 2\Delta_{\mathrm{LB}}\kappa]\hat{\mathbf{n}} \tag{107}$$

where it is understood that each of these quantities is evaluated at the Lagrangian node, $\mathbf{X}_i$.

In this work we define the mean curvature of a sphere to be positive, however both sign conventions are used in the literature. Numerical approximations of Equation (16) have been the subject of reviews by Guckenberg et al. in [114, 115] and are computationally challenging due to the fourth order derivatives required by $\Delta_{\mathrm{LB}}\kappa$. In this work we compute the curvatures in Equation (16) using the method proposed by Garimella and Swartz [116] where, at each node, a quadratic surface is fitted to the node and its nearest neighbors. The mean and Gaussian curvatures, as well as the normal vector, of the Lagrangian nodes, can then be approximated from their analytical expressions using the standard formulae for an implicit surface [116].

Computation of the surface Laplacian of the mean curvature, $\Delta_{\mathrm{LB}}\kappa$, is done using the Cotangent Laplacian approximation outlined in the review by Reuter et al. [117]. At a Lagrangian node $\mathbf{X}_i$, $\Delta_{\mathrm{LB}}\kappa$ is computed using the following formula:

$$\Delta_{\mathrm{LB}}\kappa(\mathbf{X}_i) = \frac{1}{2A_{vor}} \sum_{j \in N(\mathbf{X}_i)} \left(\cot\alpha_{ij} + \cot\beta_{ij}\right)[\kappa(\mathbf{X}_i) - \kappa(\mathbf{X}_j)] \tag{108}$$

where $N(\mathbf{X}_i)$ is the set of Lagrangian nodes that share an edge with $\mathbf{X}_i$, α_{ij} and β_{ij} are the exterior angles of the two triangles containing the edge created by $\mathbf{X}_j$ and $\mathbf{X}_i$ [118] (see Figure 6), and A_{vor} is the area of the Voronoi region.

The Voronoi region of $\mathbf{X}_i$ is the region containing all points that are nearer to $\mathbf{X}_i$ than any other point of the triangulation, depicted in Figure 6 as the grey shaded region. The Voronoi region of

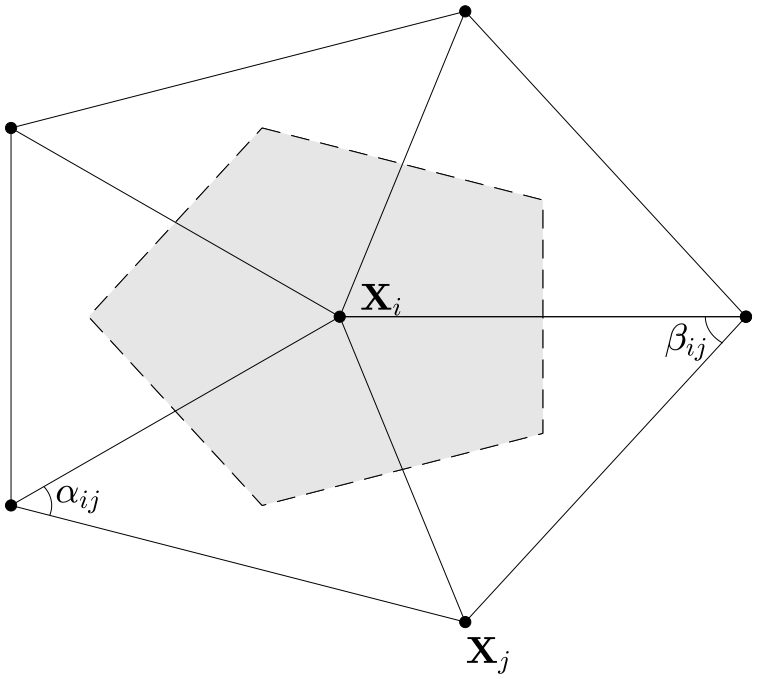

Fig. 6: The Lagrangian node $\mathbf{X}_i$ and its nearest neighbors. The node $\mathbf{X}_i$ and its neighboring nodes $\mathbf{X}_j$ are fit to a quadratic surface which is used to approximate the curvature of the capsule at the point $\mathbf{X}_i$. The shaded region is the Voronoi regoin for $\mathbf{X}_i$.

$\mathbf{X}_i$ can be computed as follows [119]:

$$A_{\text{vor}}(\mathbf{X}_i) = \frac{1}{8} \sum_{j \in N(\mathbf{X}_i)} \left(\cot \alpha_{ij} + \cot \beta_{ij}\right) \|\mathbf{X}_i - \mathbf{X}_j\|^2 \tag{109}$$

where α_{ij} and β_{ij} are the same angles from Equation (108). For triangulations without any obtuse triangles the sum of the Voronoi regions surrounding each node will be equivalent to the surface area of the mesh and thus, the Voronoi region [119].

3.6 THE IMMERSED BOUNDARY METHOD

The fluid structure interaction coupling the membrane and the surrounding fluid is computed using the immersed boundary method (IBM) [38]. In IBM the capsule membrane is described by Lagrangian coordinates suspended in a fluid-filled domain, which is described using Eulerian coordinates. The capsule surface is discretized through the tracking of a discrete set of Lagrangian coordinates, $\mathbf{X}_\ell$, that describe the instantaneous position of the membrane interface. Forces due

to the membrane mechanics are computed at the discrete Lagrangian coordinates and are then interpolated to the Eulerian grid for use in computation of the fluid velocity. The Eulerian fluid velocity is then interpolated to the Lagrangian coordinates, where it is used to update the Lagrangian coordinates.

The Lagrangian force term, denoted by $\mathbf{P}$, has contributions due to the elastic, bending, and electric forces so that:

$$\mathbf{P} = -\mathbf{f}_m - \mathbf{f}_b + \mathbf{f}_e. \tag{110}$$

The negative signs of the membrane forces, $\mathbf{f}_m$ and $\mathbf{f}_b$, reflects the fact that these forces are exerted by the capsule on the fluid [114], whereas the electric force, $\mathbf{f}_e$, is exerted on the membrane by the fluid [60]. The Eulerian grid forces, denoted by $\mathbf{p}$, are interpolated from the Lagrangian forces through the following integral:

$$\mathbf{p}(\mathbf{x}) = \int_\Sigma \mathbf{P}(\mathbf{X})\delta(\mathbf{X}-\mathbf{x})\, \mathrm{d}\mathbf{X} \tag{111}$$

where $d\mathbf{X}$ denotes surface integration over the Lagrangian coordinates describing the capsule membrane, Σ.

Discretization of the integral in Equation (111) uses the following discrete delta function:

$$\delta_h(x) = \begin{cases} \frac{1}{4\Delta x}[1+\cos\frac{\pi x}{2\Delta x}] & |x| \le 2\Delta x \\ 0 & |x| > 2\Delta x\,. \end{cases} \tag{112}$$

Defining $\delta_h(\mathbf{X}) = \delta_h(x)\delta_h(y)\delta_h(z)$, we can write the discretization of the integral in Equations (111) as:

$$\mathbf{p}(\mathbf{x}_{ijk}) = \sum_\ell \left[A_{\mathrm{vor}}(\mathbf{X}_\ell)\mathbf{f}_e(\mathbf{X}_\ell) - A_{\mathrm{vor}}(\mathbf{X}_\ell)\mathbf{f}_b(\mathbf{X}_\ell) - \mathbf{P}_m(\mathbf{X}_\ell)\right]\delta_h(\mathbf{X}_\ell - \mathbf{x}_{ijk}) \tag{113}$$

where A_{vor} is the Voronoi area computed using Equation (109). The elastic force, $\mathbf{P}_m$, is computed using Equation (99) and has already been multiplied by the differential area, and thus does not need to be multiplied by A_{vor}. The Eulerian forces, $\mathbf{p}$, computed from Equation (113), are then incorporated into the lattice Boltzmann method through Equations (46) and (47), allowing us to

compute the Eulerian fluid velocity as described in Section 3.1.

The Eulerian fluid velocity, denoted by $\mathbf{v}$, is interpolated to the Lagrangian coordinates, giving us the capsule velocity, $\mathbf{V}$, through the following integral:

$$\mathbf{V}(\mathbf{X}) = \int_{\Omega^+ \cup \Omega^-} \mathbf{v}(\mathbf{x}) \delta(\mathbf{X} - \mathbf{x}) \, d\mathbf{x} \tag{114}$$

where $d\mathbf{x}$ denotes the three dimensional integral over the Eulerian coordinates in the domain $\Omega^+ \cup \Omega^-$. As with the force integral, the delta function in Equation (114) is approximated using Equation (112), allowing us to compute the membrane velocity at the discrete Lagrangian coordinates as follows:

$$\mathbf{V}(\mathbf{X}_\ell) = \sum_{ijk} \mathbf{v}(\mathbf{x}_{ijk}) \delta_h(\mathbf{X}_\ell - \mathbf{x}_{ijk}) \Delta x^3. \tag{115}$$

The discrete membrane velocity, $\mathbf{V}(\mathbf{X}_\ell)$, is then used for numerical integration of the membrane shape equation, given by Equation (10) and re-stated here as:

$$\frac{\partial \mathbf{X}}{\partial t} = \mathbf{V}(\mathbf{X}, t). \tag{116}$$

In this work we use 2$^{\text{nd}}$ order Adams-Bashforth to integrate Equation (116), giving us the following formula for updating the capsule nodes:

$$\mathbf{X}_\ell(t_{n+1}) = \mathbf{X}_\ell(t_n) + \frac{\Delta t}{2} \left[3\mathbf{V}(\mathbf{X}_\ell, t_{n+1}) - \mathbf{V}(\mathbf{X}_\ell, t_n) \right]. \tag{117}$$

Note that in our multigrid implementation, Δt is not the same value as δt, the time step in the lattice Boltzmann equation. In fact, as discussed below, values of Δt several orders of magnitude larger than δt are sufficient to produce physically accurate results using the dual time-stepping scheme outlined in Section 3.8.

For explicit numerical integration of the capsule position, such as the scheme proposed here, the stability of the algorithm is given as follows [120, 121, 28]:

$$\Delta t < \alpha \frac{\mathrm{Ca} \cdot h}{ka} \tag{118}$$

where h is the size of the mesh elements and α is a constant that depends on the method of

integration used to solve Equation (116).

3.6.1 COUPLING THE IMMERSED INTERFACE METHOD AND THE IMMERSED BOUNDARY METHOD

The interface in the Immersed Interface Method is represented by the levelset function, ϕ. In this work an approximation to ϕ must be computed at each time step based on the location of the Lagrangian nodes. At an Eulerian node, $\mathbf{x}_{ijk}$, the levelset function is computed in the following manner:

$$\phi(x_i, y_j, z_k) = \mathbf{n}_\ell \cdot \frac{\mathbf{x}_{ijk} - \mathbf{X}_\ell}{\|\mathbf{x}_{ijk} - \mathbf{X}_\ell\|} \|\mathbf{X}_\ell - \mathbf{x}_{ijk}\| \tag{119}$$

where $\mathbf{X}_\ell$ is the Lagrangian node nearest to $\mathbf{x}_{ijk}$ and $\mathbf{n}_\ell$ is the outward normal vector at $\mathbf{X}_\ell$.

Temporal intergration of the transmembrane potential equation, Equation (73), with the Crank-Nicholson method requires knowledge of W and G at the previous time step. As the membrane deforms, location of the intersection between the Eulerian grid and the membrane change and thus, the location of the control points on which W and G are defined change at each time step. In order to store previous values of W and G for the next time step, these quantities must be interpolated from the control points used by the Immersed Interface Method to the Lagrangian nodes used by the Immersed Boundary method. Interpolating functions of the following form are desired:

$$w(\mathbf{X}_\ell) = \sum_{i=1}^{N} \alpha_i w\left(\bar{\mathbf{X}}_i\right) \tag{120}$$

$$g(\mathbf{X}_\ell) = \sum_{i=1}^{N} \beta_i g\left(\bar{\mathbf{X}}_i\right) \tag{121}$$

where α_i and β_i are interpolating coefficients to be determined at each time step, $\mathbf{X}_\ell$ represents a Lagrangian node, and $\bar{\mathbf{X}}_i$ represents the i^{th} control point in the interpolation. In this work the interpolating coefficients are computed using the method discussed in Appendix B.1.

At each time step the values of W and G must also be interpolated from the Lagrangian nodes onto the new control points for the Immersed Interface Method. In this work we follow the interpolation proposed in [49], originally proposed for the interpolation of curvature on a triangular surface mesh. In this scheme the values of W and G at the Lagrangian node and its nearest neighbors are fit to a quadratic function using least squares. At each Lagrangian node, $\mathbf{X}_\ell$, a local

coordinate system (ξ, η, τ) is constructed, where ξ represents the normal coordinate and η and τ represent coordinates in the plane tangent to the surface at $\mathbf{X}_\ell$. Using Taylor's theorem we can expand the value of w at the i^{th} neighbor of $\mathbf{X}_\ell$, denoted here as $\mathbf{X}_\ell^i$, in terms of the local coordinates, (η_i, τ_i), as follows:

$$w^i = w^0 + \eta_i \partial_\eta w^0 + \tau_i \partial_\tau w^0 + \frac{1}{2}\eta_i^2 \partial_{\eta\eta} w^0 + \eta_i \tau_i \partial_{\eta\tau} w^0 + \frac{1}{2}\tau_i^2 \partial_{\tau\tau} w^0 \tag{122}$$

$$= w^0 + a\eta_i + b\tau_i + c\eta_i^2 + d\eta_i\tau_i + e\tau_i^2 \tag{123}$$

where $w^0 = w(\mathbf{X}_\ell)$ and $w^i = w\left(\mathbf{X}_\ell^i\right)$. The expansion of w^i at neighboring Lagrangian nodes allows us to construct the following system:

$$\begin{pmatrix} \eta_1 & \tau_1 & \frac{1}{2}\eta_1^2 & \eta_1\tau_1 & \frac{1}{2}\tau_1^2 \\ \eta_2 & \tau_2 & \frac{1}{2}\eta_2^2 & \eta_2\tau_2 & \frac{1}{2}\tau_2^2 \\ \vdots & \vdots & \vdots & \vdots & \vdots \\ \eta_{N-1} & \tau_{N-1} & \frac{1}{2}\eta_{N-1}^2 & \eta_{N-1}\tau_{N-1} & \frac{1}{2}\tau_{N-1}^2 \\ \eta_N & \tau_N & \frac{1}{2}\eta_N^2 & \eta_N\tau_N & \frac{1}{2}\tau_N^2 \end{pmatrix} \begin{pmatrix} a \\ b \\ c \\ d \\ e \end{pmatrix} = \begin{pmatrix} w^1 - w^0 \\ w^2 - w^0 \\ \vdots \\ w^{N-1} - w^0 \\ w^N - w^0 \end{pmatrix}. \tag{124}$$

For the meshes used in this work, $N = 5$ or $N = 6$, depending on the node in question and the system is solved with either Gaussian elimination or a least squares fit.

Solution of the system given by Equation (124) gives us the coefficients for a quadratic approximation to w at each of the Lagrangian nodes with $O(h^2)$, where h is the typical mesh edge length. To compute the value of w at the control point, $\bar{\mathbf{X}}_i$, we find the Lagrangian node, $\mathbf{X}_\ell$, that is closest to $\bar{\mathbf{X}}_i$, compute the local coordinates, (η_i, τ_i), giving us the following representation of $w\left(\bar{\mathbf{X}}_i\right)$:

$$w\left(\bar{\mathbf{X}}_i\right) = w(\mathbf{X}_\ell) + a\eta_i + b\tau_i + c\eta_i^2 + d\eta_i\tau_i + e\tau_i^2. \tag{125}$$

The same process is repeated for the jump in ψ_n. These interpolations are then used in Equation (76) as W^n and G^n.

3.7 FLUID VISCOSITY

When there is a jump between the viscosity inside the capsule, μ^-, and the viscosity of the ambient fluid, μ^+, we use the front-tracking method originally proposed by Zhang et al. in [122] for LBM-IBM models. A smoothed Heaviside function is used to compute the viscosity at points near the capsule membrane. For the Eulerian point, $\mathbf{x}_{ijk}$, the viscosity is given by:

$$\mu(\mathbf{x}_{ijk}) = \mu^- + (\mu^+ - \mu^-)H[d(\mathbf{x}_{ijk})] \tag{126}$$

where $d(\mathbf{x}_{ijk})$ is the signed distance between a given Eulerian point, $\mathbf{x}_{ijk}$, and the nearest Lagrangian node. As in [122], the following discrete approximation to the Heaviside function in Equation (126) is used in this work:

$$H(d) = \begin{cases} 0 & d < -2\Delta x \\ \frac{1}{2}(1 + \frac{d}{2\Delta x} + \frac{1}{\pi}\sin\frac{\pi d}{2\Delta x}) & -2\Delta x \leq d \leq 2\Delta x \\ 1 & d > 2\Delta x \end{cases} \tag{127}$$

With the viscosity updated we can use $\mu(\mathbf{x}_{ijk})$ in Equation (44) to update the corresponding relaxation parameters associated with the LBM.

3.8 DUAL TIME STEPPING SCHEME

The typical Reynolds number for numerical simulations of capsule deformation are on the order of 10^{-2}, and thus the inertial terms in the Navier-Stokes equations have only a small effect on the flow field. In order to de-couple the physical time step from the LBM algorithm we propose a quasi-steady, dual time-stepping LBM scheme, which neglects the transient term in Equation (1) and instead solves the steady-state Navier-Stokes equations given by:

$$\rho\mathbf{v}\cdot\nabla\mathbf{v} = -\nabla p + \mu\nabla^2\mathbf{v} + \mathbf{p} \tag{128}$$

$$\nabla\cdot\mathbf{v} = 0. \tag{129}$$

At each physical time step, Equations (128) and (129) are solved iteratively using the multigrid

lattice Boltzmann method [88, 123, 124] discussed in Section 3.1.1. The LBM time step, δt, defined in Equation (37) becomes a pseudo-time step related to the iterative LB scheme, allowing us to introduce a new physical time step, Δt, used to update the capsule position in Equation (117). With this change, Δt can be selected based on the stability constraints and time scales of capsule deformation without compromising the lattice structure of the LBM discretization.

In order to demonstrate the potential for speed-up offered by a dual time-stepping (DTS) scheme, we first estimate the physical time scales of capsule deformation in shear flow using k, μ^+, E_s, E_b, and a. The fluid time scale is given by $t_f = k^{-1}$, the elastic time scale is given by $t_m = \mu^+ a/E_s = \mathrm{Ca} \cdot k^{-1}$ and, when bending stiffness is considered, the bending modulus time scale is given by $t_b = \mu^+ a/(E_b E_s) = \mathrm{Ca} \cdot k^{-1}/E_b$. Since typical parameter ranges are given by $\mathrm{Ca} \sim 10^{-2} - 1$ and $E_b \sim 10^{-3} - 10^{-1}$, t_m is the most restrictive time scale.

To illustrate the large separation of scales between the standard LBM-IBM time step and the time scales of capsule deformation, consider the ratio of t_m to the LBM time step, δt:

$$\frac{t_m}{\delta t} = \frac{\mathrm{Ca}}{k \delta t}. \tag{130}$$

In the LBM-IBM capsule model, δt is determined by the grid resolution based on Equation (37), and thus, for a fixed value of Ca and a fixed grid resolution, $t_m/\delta t$ can only be adjusted by the shear rate, k. The shear rate is restricted by the stability constraint given by Equation (118). In this work we find that a shear rate, k, on the order of 10^{-4} s^{-1} is required for numerical stability. Inserting $k = 10^{-4}$ s^{-1} and the time step determined by the Eulerian grid resolution, $\delta t = 0.1$ s, into the ratio given by Equation (130) results in $t_m/\delta t \sim 10^5 \cdot \mathrm{Ca}$. The large value of $t_m/\delta t$ indicates that there is a large separation between the physical and LBM time scales of the problem.

3.8.1 CONVERGENCE CRITERION

For iterative solution of the fluid velocity the convergence criterion is given by:

$$\frac{\left\| \mathbf{v}^{n+1} - \mathbf{v}^n \right\|_2}{\left\| \mathbf{v}^{n+1} \right\|_2} \leq \varepsilon \tag{131}$$

where ε is a user-defined tolerance. For computation of the flow using the DTS scheme proposed

in this work, the flow is computed iteratively until Equation (131) is satisfied, at which point the fluid velocity is assumed to have converged to the correct flow field. In order to determine the choice of ε in Equation (131) simulations of a capsule in simple shear flow were conducted for $\mathrm{Re} = 0.05$, $\mathrm{Ca} = 0.05$, $\lambda = 1$, $E_b = 0$, $k = 2 \times 10^{-4}$ s^{-1}, and $k\Delta t = 0.02$. The results can be seen in Figure 7a where the deformation parameter, D_{xy}, is plotted as a function of dimensionless time, kt, for values of ε ranging from 10^{-3} to 10^{-7}. As can be seen in the figure, the deformation converges to the correct final deformation for all of the values shown, however, the intermediate dynamics show slight deviations for larger tolerances, ε. For $\varepsilon = 10^{-3}$ and $\varepsilon = 10^{-4}$ the deformation occurs at a slightly faster pace, however, the curves for $\varepsilon \leq 10^{-5}$ are all nearly identical.

This is best seen in the inset of Figure 7a, which shows the differences between the values of D_{xy} between $kt = 0.9$ and $kt = 1.1$. The curves for $\varepsilon = 10^{-5}$, $\varepsilon = 10^{-6}$ and $\varepsilon = 10^{-7}$ exhibit close agreement. The curves for $\varepsilon = 10^{-3}$ and $\varepsilon = 10^{-4}$ deviate from the curves for smaller values of ε, with $\varepsilon = 10^{-4}$ showing better agreement than $\varepsilon = 10^{-3}$, indicating convergence of D_{xy} as $\varepsilon \to 0$. Similar results were obtained for other values of λ, E_b, Ca and Δt as well as for other initial capsule geometries.

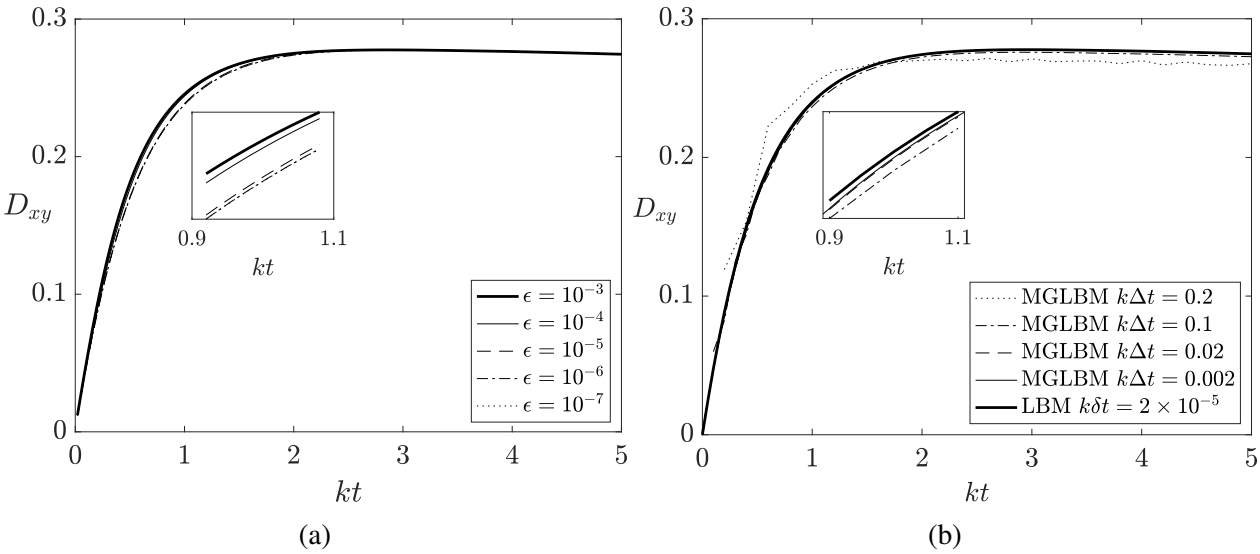

Fig. 7: The effect of the iterative tolerance and time step on the evolution of D_{xy}. (a) D_{xy} for various choices of the iterative tolerance, ε. (b) D_{xy} for various time steps, Δt.

3.8.2 TIME STEP SELECTION

Because Δt is no longer linked to the spatial discretization, selection of the time step can be determined based on the desired accuracy of the simulation. In Figure 7b the deformation parameter is plotted for various values of the dimensionless time step, $k\Delta t$, along with the deformation parameter from the standard MRT LBM for simulations of an initially spherical capsule with $\mathrm{Ca} = 0.05$, $\lambda = 1$, $E_b = 0$, and $k = 2 \times 10^{-4}$ s^{-1}. For the multigrid LBM simulations a tolerance of $\varepsilon = 10^{-5}$ was used.

From the figure it's clear that, while $k\Delta t = 0.2$ captures the qualitative behavior of the deformation, the time step is too large to accurately resolve the dynamics. $k\Delta t = 0.1$, $k\Delta t = 0.02$ and $k\Delta t = 0.002$, however, all closely follow the deformation curve of the standard LBM simulation, with convergence to the standard LBM method as $k\Delta t \to k\delta t = 2 \times 10^{-5}$. From the inset to Figure 7b it can be seen that the curves for $k\Delta t = 0.002$ and $k\Delta t = 0.02$ fall on top of each other, with only a slight deviation from the deformation obtained from the standard LBM model, while the curve for $k\Delta t = 0.1$ shows slightly larger deviations from the standard LBM curve. Similar results are also found for larger values of Ca.

For a fixed value of k, the elastic time scale, $t_m = \mathrm{Ca} \cdot k^{-1}$, is proportional to Ca. To account for this we set $k\Delta t = 0.02$ for $\mathrm{Ca} \geq 0.05$, while for $\mathrm{Ca} < 0.05$ the time step is decreased proportionally with the capillary number. This can be summarized by the following equation:

$$k\Delta t = \min\left(0.4 \cdot \mathrm{Ca}, 0.02\right). \tag{132}$$

For simulations of simple shear flow Equation (132) has been found to be sufficient for accurate and stable simulations.

When an electric field is considered the membrane charging time scale, t_c, must also be resolved. For some parameter regimes t_c may be more restrictive than the elastic time scale, t_m and thus, for electrohydroydnamic simulations an additional constraint on the time step must be applied. In this work we find the following constraint on the dimensionless time step, Δt, to be sufficient for resolution of t_m and t_c.

$$k\Delta t = \min\left(0.4 \cdot \mathrm{Ca}, 0.05 \cdot t_c, 0.02\right). \tag{133}$$

CHAPTER 4

CAPSULES IN SHEAR FLOW

Shear-induced capsule deformation has been studied extensively with analytical, experimental, and numerical results widely reported in the literature [28, 26]. As such the dynamics are well-known and will be used as a test case for the accuracy and efficiency of the dual time-stepping scheme proposed here. An illustration of the capsule in the $x-y$ plane, which is plane of shear for this work, can be seen in Figure 8. The capsule is placed in the center of the fluid domain with its major axis aligned $\pi/4$ radians above the x-axis. In terms of the shear rate, k, domain height, H, the far-field condition for the fluid velocity, $\mathbf{v}$, is given by:

$$\mathbf{v} = \left[k\left(y - \frac{1}{2}H\right), 0, 0\right]^{\mathrm{T}} \tag{134}$$

The boundary conditions for the flow field are periodic in the x and z coordinates and are $v_x = -\frac{1}{2}Hk$ at $y = 0$ and $v_x = \frac{1}{2}Hk$ at $y = H$.

The simulations are conducted with a Reynolds number of $\mathrm{Re} = 0.05$, a capsule radius of $a = 1$ m, a density of $\rho = 1\ \mathrm{kg}\cdot\mathrm{m}^{-3}$, and a shear rate of $k = 2\times 10^{-4}\ \mathrm{s}^{-1}$. A range of simulations with varying values of the capillary number, Ca, bending stiffness, E_b, and viscosity ratio, λ, are conducted for spherical, spheroidal, and biconcave capsules. The simulations are primarily assessed based on the deformation parameter, D_{xy}, and inclination angle, $\frac{\theta}{\pi}$, however, the evolution of the capsule shape and flow field are also considered.

The fluid domain used here is $[0, 12.8a]\times[0, 12.8a]\times[0, 12.8a]$ where a is the capsule's equivalent radius. The Eulerian grid is discretized into a 129^3 grid, which results in a step size of $\Delta x = \Delta y = \Delta z = 0.1a$. The simulations presented here were conducted with the time step, Δt, selected using Equation (132). The convergence criterion for the multigrid LBM was set to $\varepsilon = 10^{-5}$ based on the results from Section 3.8.1. Each multigrid cycle uses a 5 grid level w-cycle multigrid schedule. The capsule mesh consists of 5120 triangular elements composed of 2562 Lagrangian nodes.

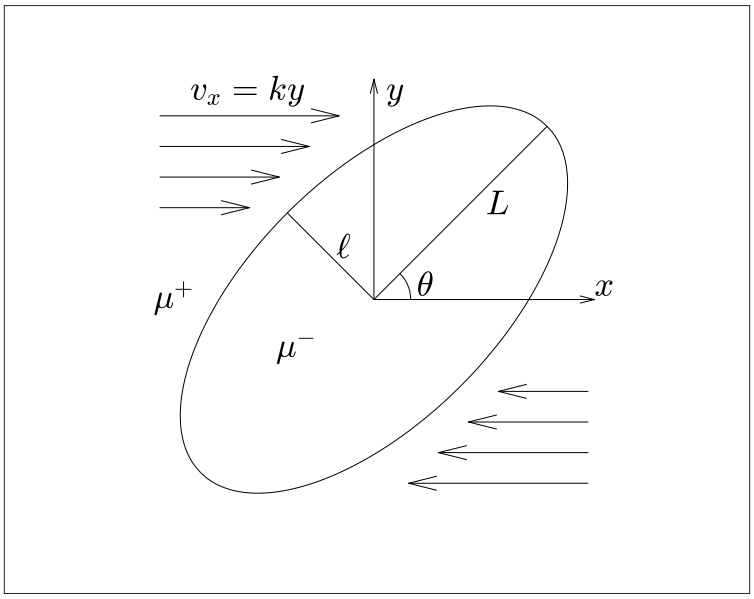

Fig. 8: The initial configuration for a spheroidal capsule in shear flow.

The MRT relaxation parameters s_4 and s_1 are set according to Equations (44) and (45) respectively. The parameters s_0, s_3, s_5, and s_7 correspond to the conserved moments and are thus set equal to zero. The remaining relaxation parameters are set equal to 1.8.

4.1 SPHERICAL CAPSULES

The dynamics of spherical capsules in shear flow have been studied theoretically [31, 32], experimentally [34, 35, 40], and numerically (e.g. [37, 39, 97, 44, 83]) and are well-known. At moderate capillary numbers (Ca $\lesssim 0.2$ for neo-Hookean membranes) the capsule will deform until reaching an approximately constant equilibrium shape [31, 32]. After reaching a constant shape, the flow causes the membrane to rotate around the internal fluid without further deformation. This phenomenon, known as tank-treading, has also been observed experimentally for spherical [40] and biconcave [22] capsules. In general, increasing values of Ca result in more deformation and greater rotation of the capsule toward the x-axis. For large values of Ca, capsule breakup will occur [34]. Unless otherwise noted the results for spherical capsules are for a neo-Hookean membrane.

In Figure 9 the results for simulations of initially spherical capsules are given for a variety of capillary numbers, Ca, with $E_b = 0$ and $\lambda = 1$. Figures 9a and 9b plot the deformation parameter

and inclination angle of the capsule as a function of time. The results are compared to the published results in [37] and [44] showing close agreement. As can be seen in the figures, the flow causes the sphere to gradually deform and rotate toward the x-axis. This process occurs until the capsule obtains a steady shape and inclination, as can be seen by the constant values of D_{xy} and θ/π at large values of the dimensionless time, kt. Increased values of Ca result in greater deformation and more rotation.

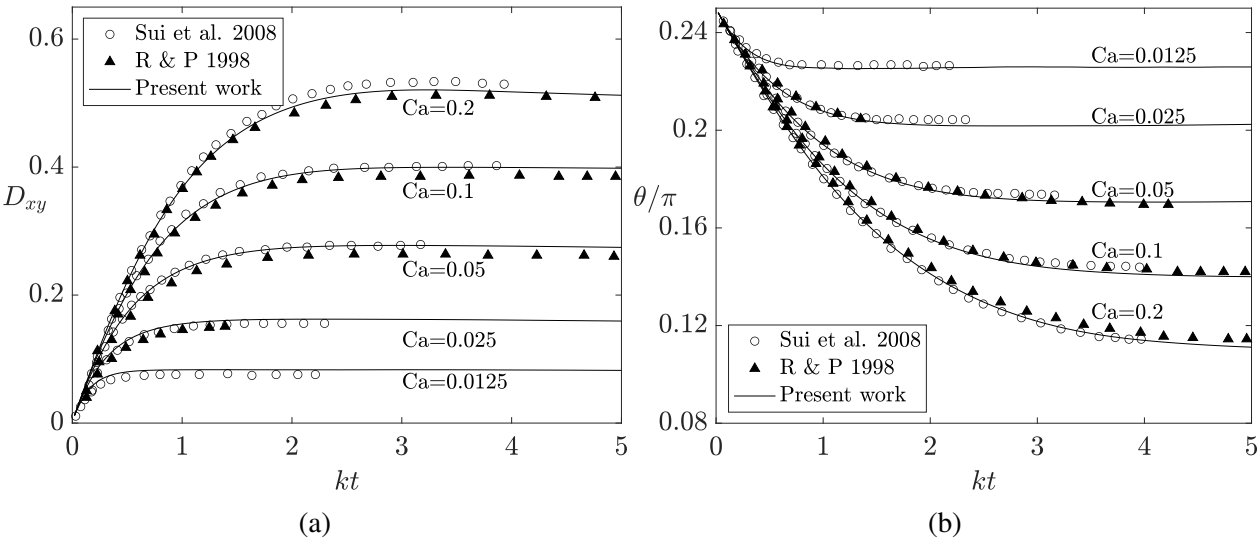

Fig. 9: (a) The deformation parameter and (b) inclination angle of an initially spherical capsule for various values of Ca with $\lambda = 1$ and $E_b = 0$.

Figure 10a shows the final shapes obtained from our simulations as a function of the capillary number. As can be seen the final shapes move farther away from a sphere as Ca is increased. In Figure 10b the trajectory of a particle on the membrane surface is tracked for a capillary number of Ca=0.05. As can be seen, once the capsule reaches its final shape the particle rotates around the capsule in the tank-tread motion discussed above.

In Figure 11 the results from simulations for a spherical Skalak membrane with area dilation modulus, $C = 1$, are shown for for a variety of capillary numbers, Ca. Figures 11a and 11b plot the deformation parameter and inclination angle of the capsule as a function of time. The results are

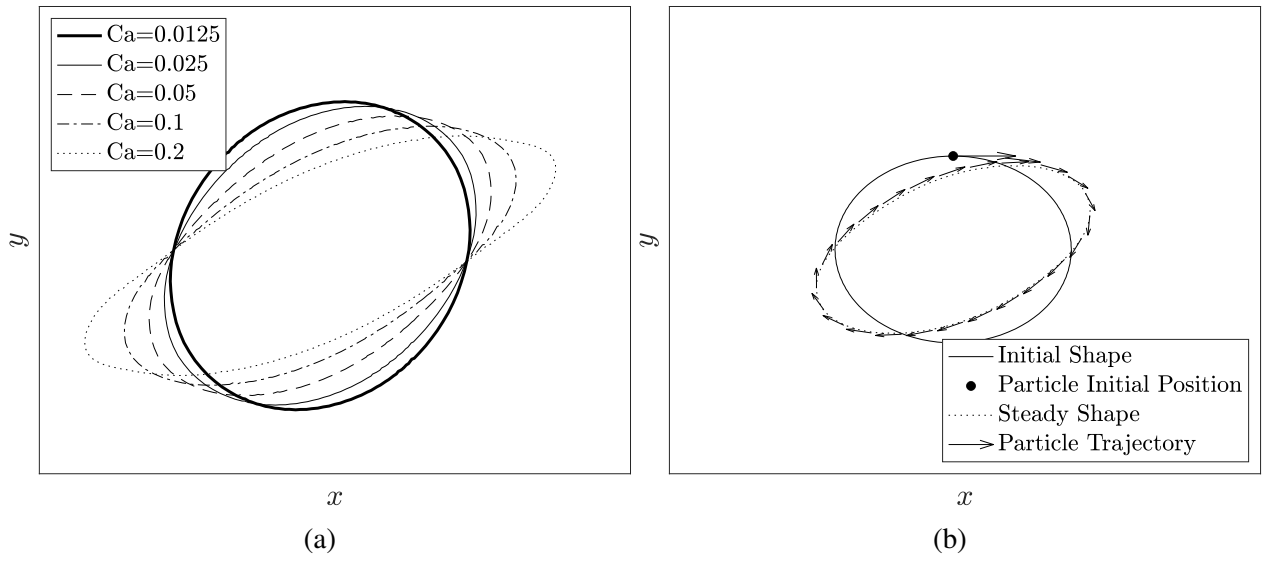

Fig. 10: The tank-treading behavior of initially spherical capsules in a shear flow. (a) Steady state shape of capsules for various values of Ca. (b) The trajectory of a particle for an initially spherical capsule with Ca=0.05.

compared to the published results by Sui et al. in [44] and show close agreement. As can bee seen in the figure, the behavior of a Skalak membrane is qualitatively similar to that of a neo-Hookean membrane, reaching an equilibrium shape and exhibiting tank-treading behavior. The effect of the strain-hardening behavior of Skalak's law can be seen when comparing the results in Figure 11 with the results for the strain-softening neo-Hookean membranes seen in Figure 9, as the Skalak membrane deforms less for a given capillary number. It should be noted that for large values of the area dilation modulus, C, a spherical capsule will remain spherical, since any deformation from a sphere will result in an increase in the capsule's surface area.

In Figure 12 the evolution of D_{xy} is plotted for initially spherical capsules with varying values of the dimensionless bending modulus, E_b. The capillary number is fixed at Ca$= 0.05$, the viscosity ratio is fixed at $\lambda = 1$, and the spontaneous curvature is set at $c_0 = 0$. The capsules exhibit the same tank-treading behavior discussed above with close agreement between results from the present study and the results published by Le in [46]. For a fixed capillary number, increasing E_b results in reduced deformation.

In Figure 13 the internal to external viscosity ratio is set to $\lambda = 5$ for varying values of the

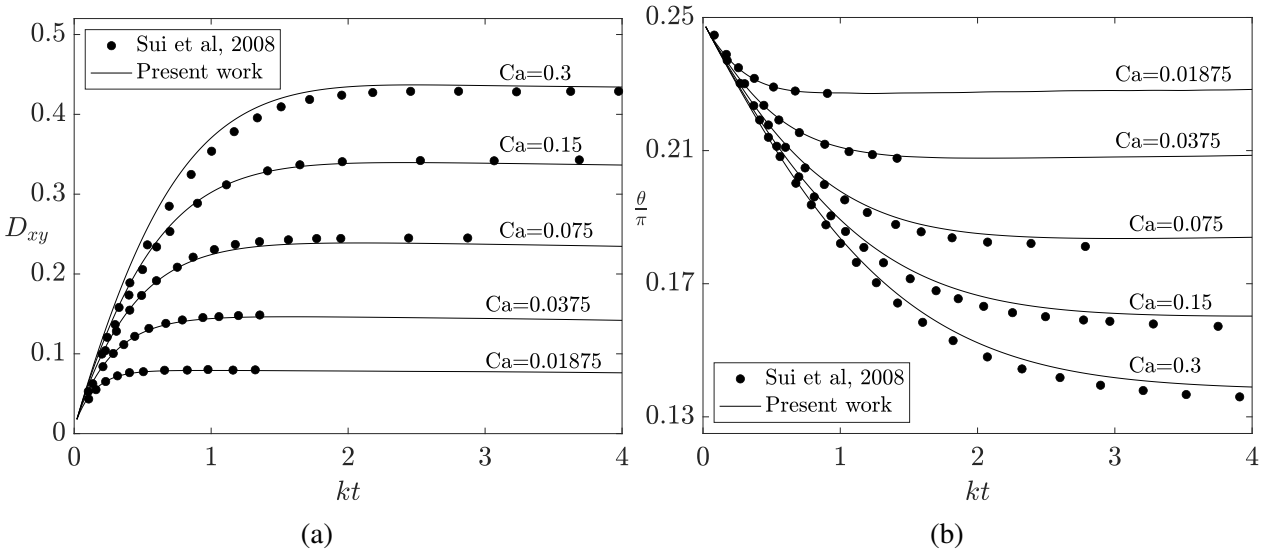

Fig. 11: (a) The deformation parameter and (b) inclination angle of an initially spherical Skalak capsule for various values of Ca with $\lambda = 1$ and $E_b = 0$.

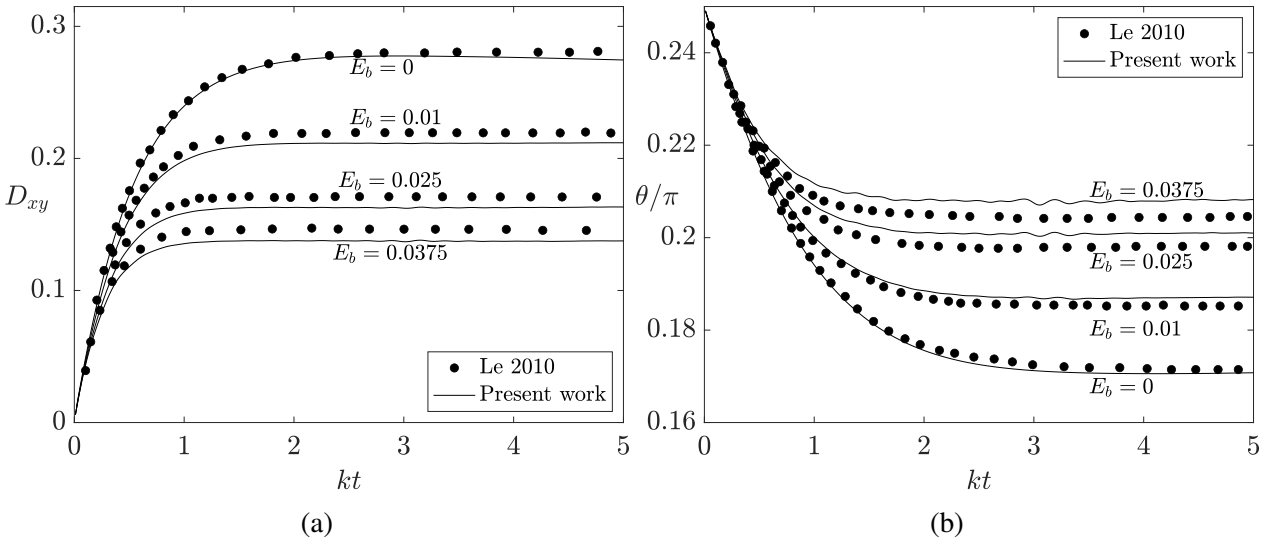

Fig. 12: (a) The deformation parameter and (b) inclination angle of an initially spherical capsule for various values of E_b with Ca= 0.05 and $\lambda = 1$.

capillary number. The effects of the membrane's bending stiffness are ignored by setting $E_b = 0$. Close agreement can be seen between the present results and those published by Le and Tan in

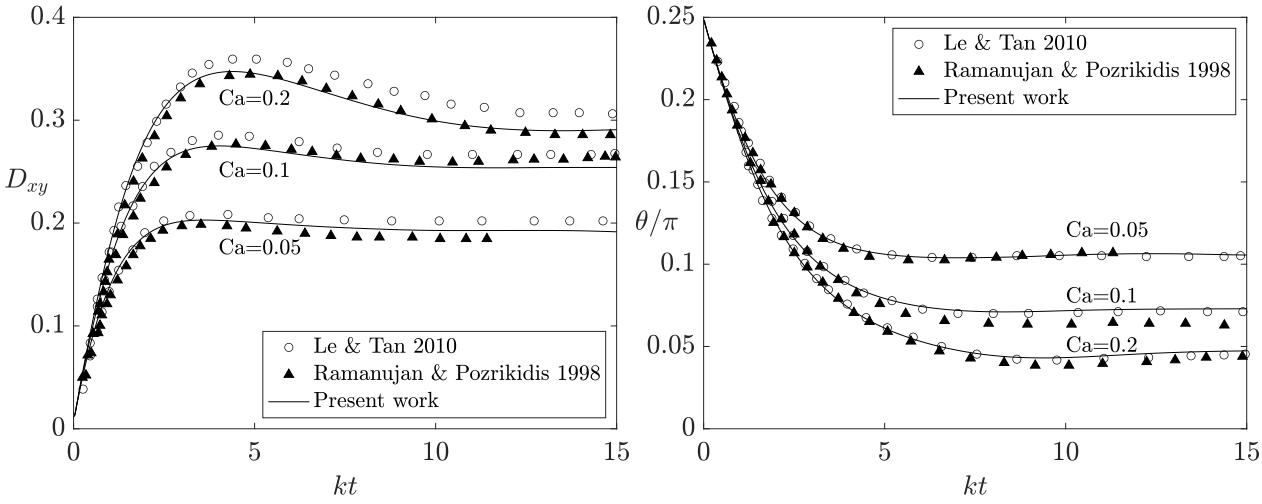

Fig. 13: (a) The deformation parameter and (b) inclination angle of an initially spherical capsule for various values of Ca with $\lambda = 5$ and $E_b = 0$.

[54] and Ramanujan and Pozrikidis in [37]. The capsules exhibit tank-treading behavior, however the increased viscosity ratio results in reduced deformation of the capsule when compared with the deformation seen for $\lambda = 1$.

In order to assess the range of validity for the quasi-steady approach proposed here, Figure 14 compares D_{xy} and θ/π for Re=0.05, Re=0.1, and Re=0.25 using the standard LBM, which solves the time-dependent incompressible Navier-Stokes equations, and the quasi-steady approach proposed here. In this figure the thin lines are the deformation parameter and the bold face lines are the inclination angle. Both simulations are conducted for spherical capsules with Ca $= 0.05$, $\lambda = 1$, and $E_b = 0$ for a Neo-Hookean membrane. In Figure 14a, for Re=0.05, the two numerical schemes are seen to produce nearly equivalent results, suggesting that for Re=0.05 neglecting the transient term of the Navier-Stokes equations does not affect the dynamics of the capsule deformation. In Figures 14b and 14c, the deformation parameter and inclination angles are seen to reach the same equilibrium values for both fluid solvers, which is unsurprising since the capsule's attainment of an equilibrium shape results in a steady flow pattern. Before reaching the equilibrium shape, however, the deformation and inclination of the quasi-steady simulation can be seen to deviate from the standard LBM, with larger deviations occurring for the case with the larger Reynolds

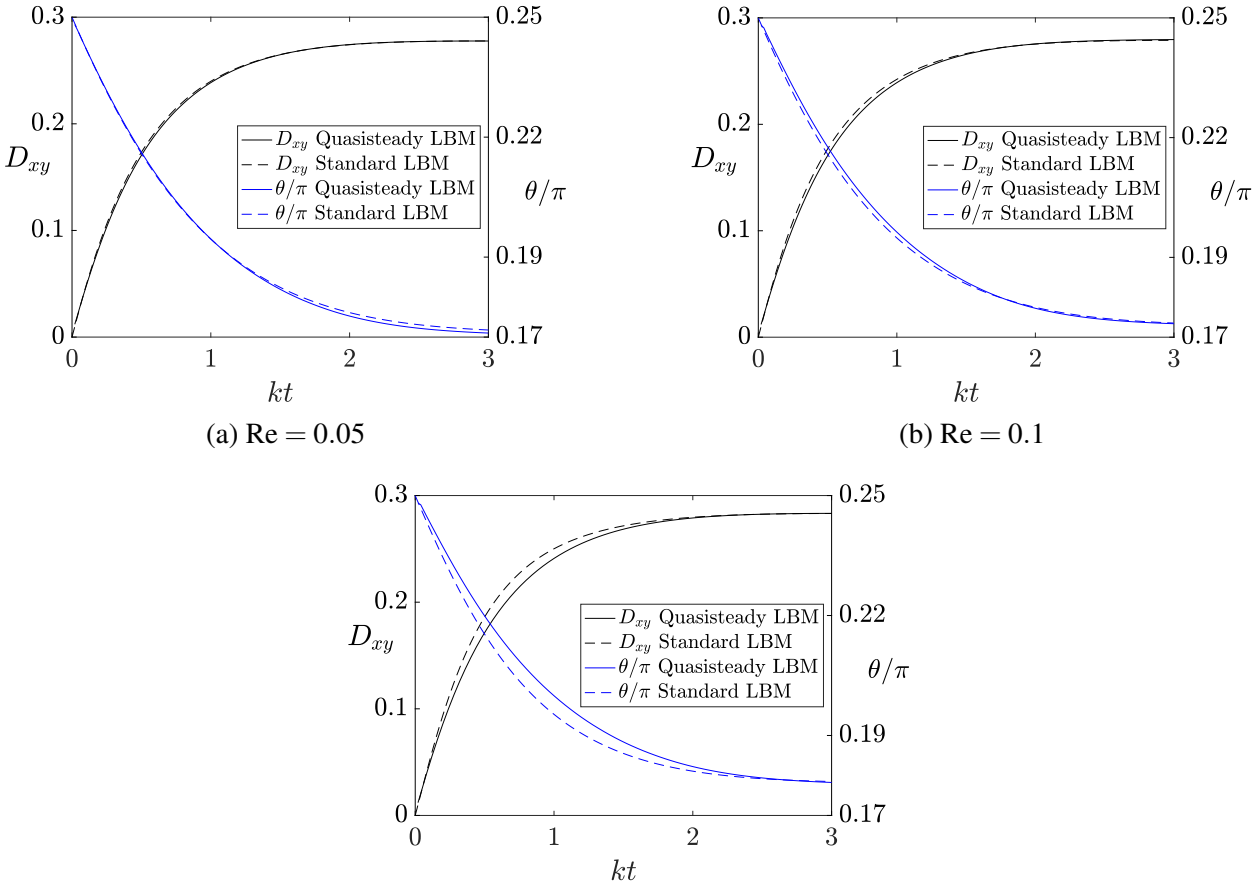

(a) Re $= 0.05$

(b) Re $= 0.1$

(c) Re $= 0.25$

Fig. 14: The deformation parameter and inclination angle of an initially spherical capsule for various values of Re with Ca$= 0.05$, $E_b = 0$, and $\lambda = 1$.

number, Re $= 0.25$. Based on these results, care should be taken when simulating the dynamics of phenomena with Re ≥ 0.1, as neglecting the transient term in the Navier-Stokes equations may affect the dynamics.

4.2 SPHEROIDAL CAPSULES

To further demonstrate the efficacy of our method we consider the deformation of an oblate spheroid in shear flow. An oblate spheroid resembles a flattened sphere, with two axes of equal length and the length of the third axis less than that of the other two. The parametrization for an

oblate spheroid can be given in terms of the azimuthal angle, ϕ, and polar angle, θ, as follows:

$$x = R\sin\theta\cos\phi \qquad z = R\sin\theta\sin\phi \qquad y = R\frac{b}{a}\cos\theta. \tag{135}$$

The polar angle is measured from the y axis and the azimuthal angle is the angle in the $x-z$ plane, with $\phi = 0$ corresponding to the positive x axis. In Equation (135) R is used to adjust the radius so that the spheroid has a volume equivalent to the volume of a sphere with radius 1.

Unlike initially spherical capsules, the spheroids do not reach a constant steady shape. Instead, the capsule's shape and inclination oscillate while the membrane rotates around the interior fluid. In weak shear flows and at high viscosity ratios, the capsule's motion will transition from tank-treading to a tumbling motion [125, 126, 127].

In Figure 15 D_{xy} and θ/π are shown for a spheroid with $b/a = 0.9$ for $\lambda = 1$, $E_b = 0$ and capillary numbers, Ca=0.05, Ca=0.1 and Ca=0.2. These simulations have been conducted by a number of authors including [37, 44, 98, 54, 56]. Here, the results are plotted alongside those reported by Le and Tan in [54]. Close agreement is observed between the present simulations and those in [54].

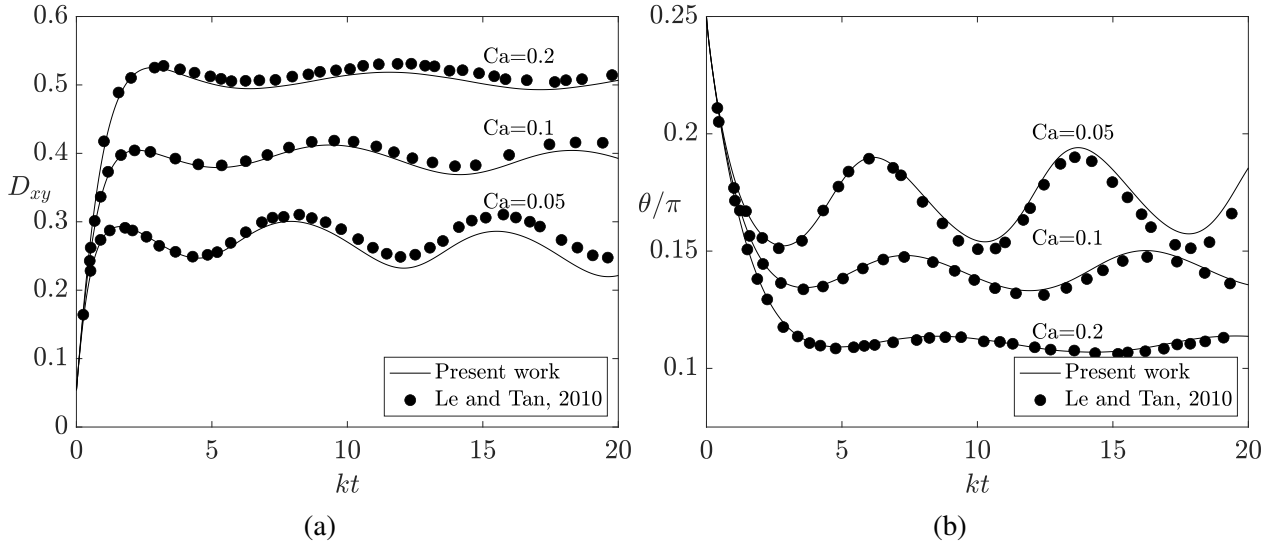

Fig. 15: (a) The deformation parameter and (b) inclination angle of an initially spheroidal capsule with $b/a = 0.9$ for various values of Ca with $\lambda = 1$ and $E_b = 0$.

In Figure 16 D_{xy} and θ/π are shown for a spheroid with $b/a = 0.5$ for $\lambda = 1$, $E_b = 0$ and capillary numbers, Ca=0.05, Ca=0.1 and Ca=0.2. For Ca=0.2 the results are compared with those reported by Sui et al. in [44], with close agreement seen between the two studies. For Ca=0.05 and Ca=0.1 Figure 16 provides a comparison between D_{xy} and θ/π for two fluid solvers: the quasi-steady method proposed in this work and the standard MRT lattice Boltzmann method. As can be seen in the figures, the results using the two fluid solvers are indistinguishable. This finding was true for all of the simulations of capsules in shear flow, further suggesting that the quasi-steady approach is valid for Re $= 0.05$.

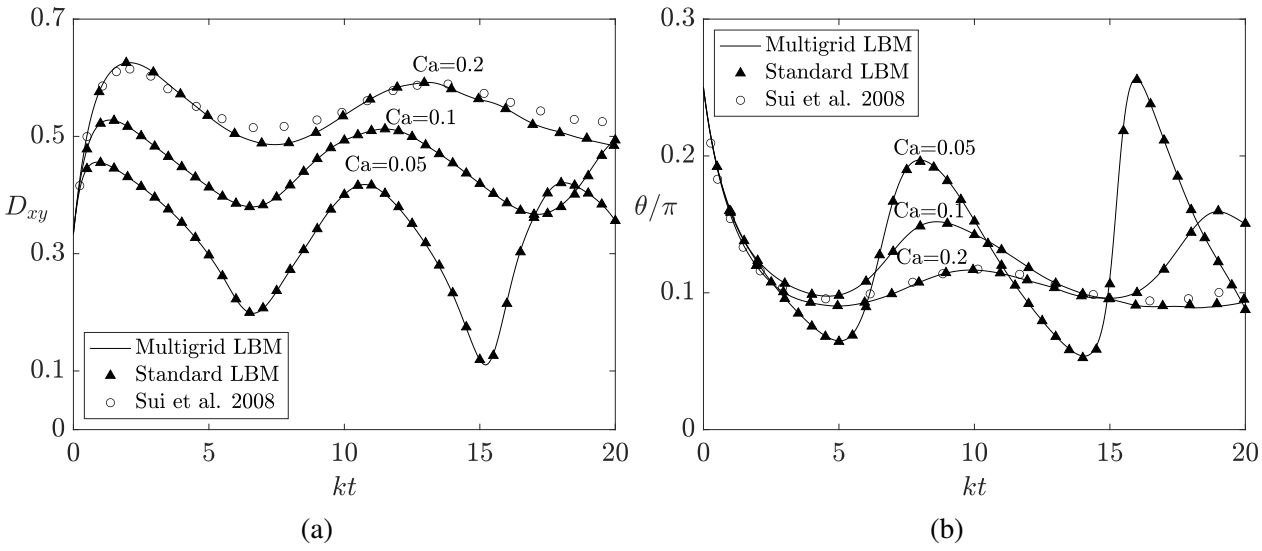

Fig. 16: (a) The deformation parameter and (b) inclination angle of an initially spheroidal capsule with $b/a = 0.5$ for various values of Ca with $\lambda = 1$ and $E_b = 0$.

In Figures 17a and 17b the trajectory of a sinlge Lagrangian node on the capsule membrane is plotted for a simulation up to $kt = 20$ with Ca=0.05, $\lambda = 1$ and $E_b = 0$ for spheroids with $b/a = 0.9$ and $b/a = 0.5$ respectively. Each arrow represents the particles current velocity for the duration of the simulation. The particle completes more than one rotation around the capsule membrane during the simulation, illustrating the deviations in capsule shape and inclination angle for spheroidal capsules. In Figure 17a, the shape of a capsule with $b/a = 0.9$ exhibits slight deviations as the

particle revolves around the interior fluid. In Figure 17b the capsule's shape and inclination angle oscillate more dramatically during tank treading. The larger deviations seen in Figure 17b are due to the larger difference between the major and minor axis of the spheroid, indicated by the lower value of b/a.

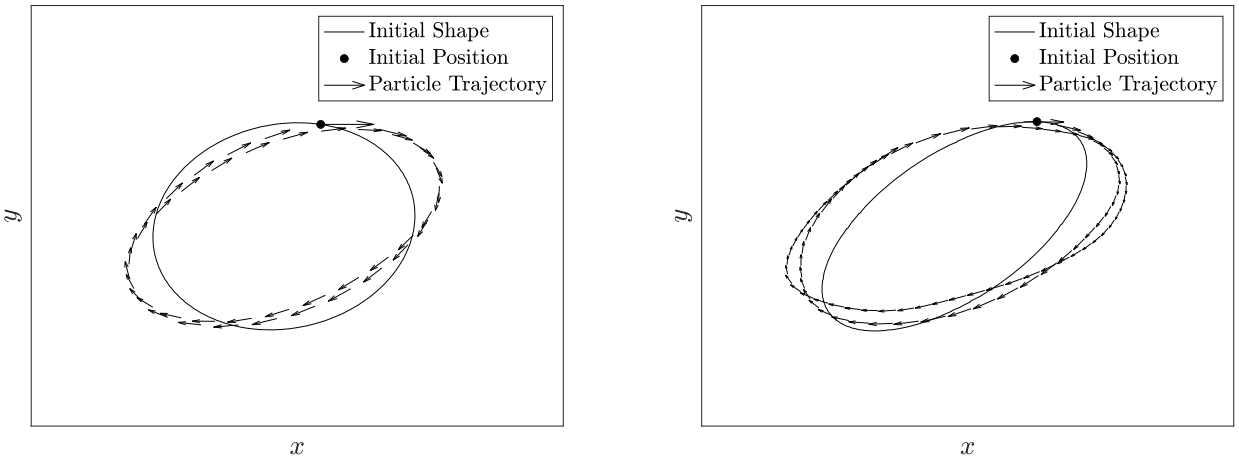

Fig. 17: The tank-treading behavior of initially spheroidal capsules. (a) The trajectory of a particle on an initially spheroidal capsule with b/a=0.9. (b) The trajectory of a particle on an initially spheroidal capsule with b/a=0.5. The dimensionless parameters are Ca= 0.05, $E_b = 0$, and $\lambda = 1$ for both cases.

4.3 BICONCAVE CAPSULES

Next we consider the deformation of an initially biconcave capsule in shear flow. The parametrization for the initial shape of the biconcave capsule used here is given by Fung in [128] in terms of the polar angle, θ, and azimuthal angle, ϕ, as:

$$x = a\alpha \sin\theta\cos\phi \qquad y = \frac{a\alpha}{2}(k_0 + k_1\sin^2\theta - k_2\sin^4\theta)cos\theta \qquad z = a\alpha\sin\theta\sin\phi \tag{136}$$

where $\alpha = 1.3858$, $k_0 = 0.207$, $k_1 = 2.003$, and $k_2 = 1.123$, and a is the radius of a sphere with the same volume as the capsule. The resulting mesh can be seen in Figure 2b.

A variety of values of the spontaneous curvature, c_0, can be found in the literature. In [55, 129] a constant negative value is used for the spontaneous curvature whereas in [53, 130] c_0 is a function of the initial curvature of the membrane, selected so as to minimize the Helfrich bending energy from Equation (15). We have followed [53, 130] and set the spontaneous curvature, c_0, in Equation (16) to $c_0 = -2H_0$, where H_0 is the initial curvature of the capsule. This selection of the spontaneous curvature facilitates comparison between the present work and [53, 130].

Although [53] and [130] used the same spontaneous curvature, they chose different values for E_b. In this work we use the values reported by Sinha and Graham in [53], which are $E_b = 0.03$ and $C = 10$. The surface elasticity modulus, G_s, used in [53] corresponds to $E_s \approx 2G_s$, and thus we re-scale C and E_b by 1/2. Thus, in this work, the bending stiffness was held fixed at $E_b = 0.015$ and Skalak's strain energy functional was used with a value of $C = 5$, matching the values used in [53].

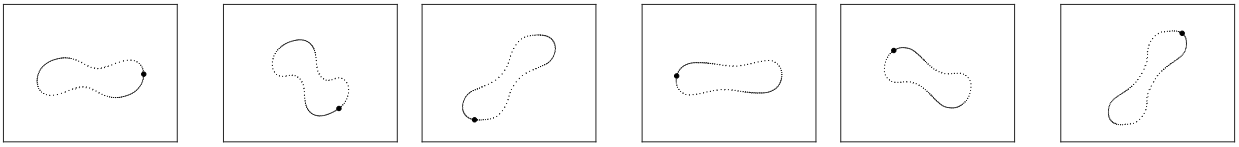

(a) $kt = 5$ (b) $kt = 8$ (c) $kt = 11$ (d) $kt = 15$ (e) $kt = 18$ (f) $kt = 21$

Fig. 18: The profile of an initially biconcave capsule with Ca= 0.25, $E_b = 0.015$, and $\lambda = 4$ at various times. The black dot is the location of a marker point on the membrane.

The dynamics of biconcave capsules in shear flow can be broadly grouped into two categories: a tumbling phase and a tank-treading phase. The tumbling phase typically occurs at low shear rates and high viscosity ratios. In the tumbling phase the capsule's shape remains roughly constant while the capsule undergoes rotations in the plane of shearing. Figure 18 shows the profile of an initially biconcave capsule with $E_b = 0.015$, Ca=0.25, and $\lambda = 4$ undergoing the tumbling motion. As can be seen in the figure, the capsule retains the biconcave shape while rotating around in the center of the domain.

The tank-treading phase, which typically occurs at higher shear rates and lower viscosity ratios,

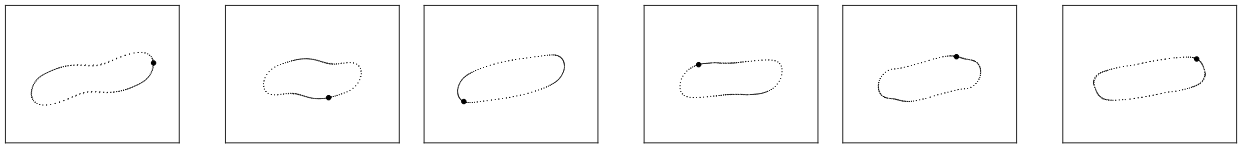

(a) $kt = 4$ (b) $kt = 10$ (c) $kt = 16$ (d) $kt = 22$ (e) $kt = 28$ (f) $kt = 30$

Fig. 19: The profile of an initially biconcave capsule with Ca= 0.75, $E_b = 0.015$, and $\lambda = 4$ at various times. The black dot is the location of a marker point on the membrane.

is characterized by a rotation of the capsule membrane around the interior fluid. Figure 19 shows the profile of an initially biconcave capsule with $E_b = 0.015$, Ca=0.75, and $\lambda = 4$ undergoing the tank-treading motion. As can be seen, the shape and inclination angle remain roughly constant throughout the motion, while the membrane rotates around the interior fluid. In between these two phases are transition phases, where a capsule will oscillate between these two behaviors or exhibit more complicated dynamics that combine the two motions [51, 53, 55, 57].

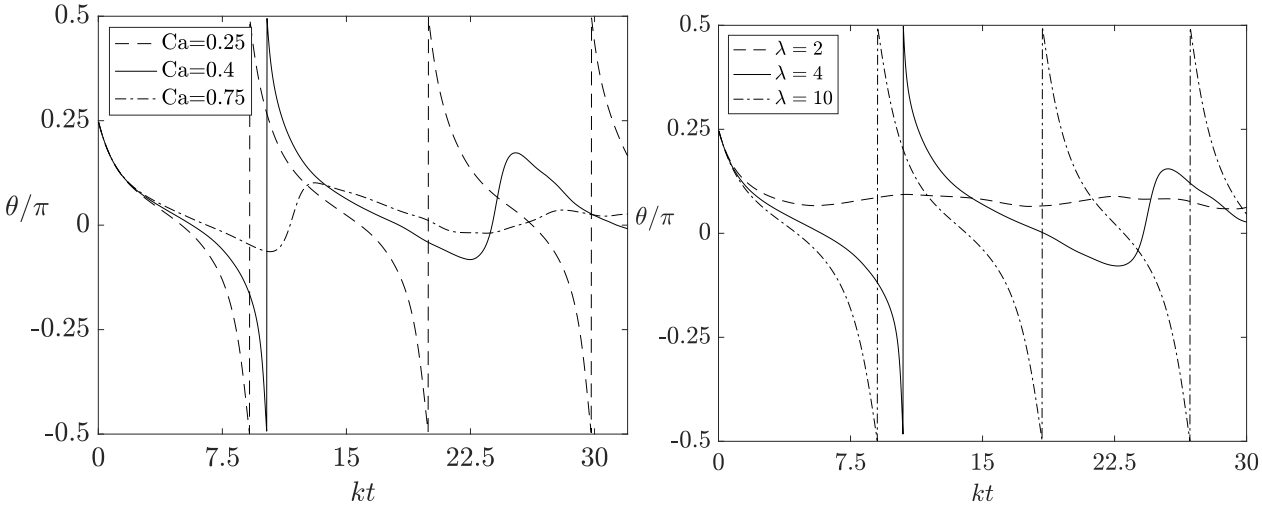

(a) (b)

Fig. 20: The effect of the shear rate and viscosity ratio on the inclination angle of an initially biconcave capsule. (a) The inclination angle for capsules with various dimensionless shear rates for a fixed viscosity ratio of $\lambda = 4$. (b) The inclination angle for capsules with various viscosity ratios for a fixed capillary number Ca= 0.4. The bending stiffness was held fixed at $E_b = 0.015$ for both figures.

Figure 20 shows the inclination angle for biconcave capsules in shear flow with $E_b = 0.015$, $C = 5$ and spontaneous curvature $c_0 = -2H_0$. Figure 20a illustrates the effect of increased capillary numbers. The viscosity ratio for the simulations in Figure 20a is held fixed at $\lambda = 4$. At Ca=0.25 the capsule undergoes tumbling motion. At Ca=0.4 the capsule first begins a tumbling motion, rotating π radians before reaching a roughly constant inclination angle with a tank-treading motion. At Ca=0.75 the capsule undergoes tank-treading motion throughout the simulation.

Figure 20b illustrates the effect of increasing the viscosity ratio. The capillary number for the simulations in Figure 20b are Ca=0.4. At $\lambda = 2$ the capsule undergoes tank-treading motion, at $\lambda = 4$ the capsule is in a transition phase, and at $\lambda = 10$ the capsule undergoes tumbling motion. As can be seen, increasing the viscosity ratio has a similar effect to decreasing the capillary number.

A number of numerical [55, 130, 129, 53] and experimental [27] studies have been conducted on the motion of red blood cells as a function of the capillary number and viscosity ratio. In order to assess the fidelity of our model we ran simulations with viscosity ratios ranging from $\lambda = 0.5$ to $\lambda = 10$ and capillary numbers ranging from Ca=0.05 to Ca=1. The simulations were then categorized as undergoing a tank-treading phase, a tumbling phase, or a transitional phase.

The results from these simulations can be seen in Figure 21. The plot also includes the boundaries between the tank-treading and tumbling phases found by Sinha and Graham in [53] and Le and Tan in [130]. The boundaries between the different phases of motion exhibit close qualitative and quantitative agreement.

4.4 COMPUTATIONAL EFFICIENCY STUDY

To demonstrate the efficiency gains attained with the dual-time stepping strategy proposed in this work, we have conducted simulations for spherical and biconcave capsules for a variety of dimensionless parameters using the standard LBM-IBM capsule model and the DTS method proposed in this work. The simulations were run on the Turing High Performance Computing Cluster at Old Dominion University using 2.3 GHz CPUs with 128 GB RAM. The resolution on the fine grid was $N = 129$ in each dimension for both the single grid and multigrid simulations. The Eulerian domain used was $[0, 12.8a]^3$ for both simulations which, coupled with the resolution of $N = 129$ in each direction, results in a time step of $\delta t = 0.1a$ s for the standard LBM simulation. As in previous sections, the simulations in this section are normalized by setting Re=0.05, $a = 1$ m,

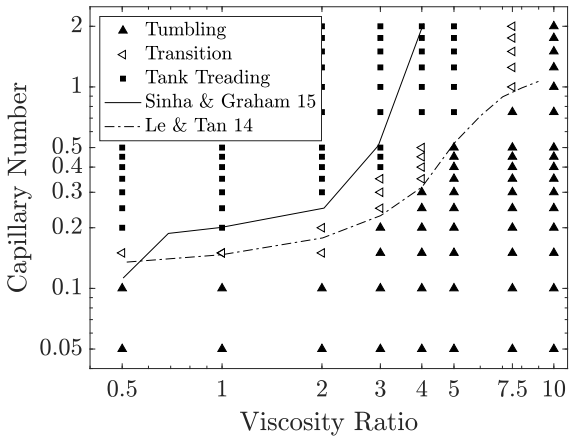

Fig. 21: Classification of simulations with biconcave capsules for a variety of capillary numbers and viscosity ratios.

and $\rho = 1\ \mathrm{kg}\cdot\mathrm{m}^{-3}$. The capsule mesh consists of 5120 triangular elements composed of 2562 Lagrangian nodes. For the DTS scheme the time step was chosen using Equation (132) and an iterative tolerance of $\varepsilon = 10^{-5}$ was used.

4.4.1 EFFICIENCY FOR SPHERICAL SIMULATIONS

To study the speed-up offered by the newly proposed method we conduct simulations for spherical capsules using the standard LBM-IBM capsule model and the DTS scheme proposed here. The capsules were assumed to have Neo-Hookean membranes with $\lambda = 1$ and $E_b = 0$ with capillary numbers ranging from 0.00625 to 0.2 and shear rates ranging from $2\times10^{-4}\ \mathrm{s}^{-1}$ to $1.6\times10^{-3}\ \mathrm{s}^{-1}$. To facilitate comparison across capillary numbers, we alter the duration of the simulations based on the capillary number. For simulations with $\mathrm{Ca} = 0.00625$ the simulations are run up to $kT = 0.5$, for $\mathrm{Ca} = 0.0125$ simulations are run up to $kT = 1$, for $\mathrm{Ca} = 0.025$ simulations are run up to $kT = 2$, and for $\mathrm{Ca} \geq 0.05$ we simulate up to $kT = 4$. This accounts for the smaller elastic time scales and smaller values of $k\Delta t$ used at smaller values of Ca.

In Figure 22a the speed-up achieved by the DTS method is plotted against the shear rate. As can be seen in the figure, the speed-up offered by the DTS method is proportional to Ca and inversely proportional to k. Both of these relationships can be understood by examining the time

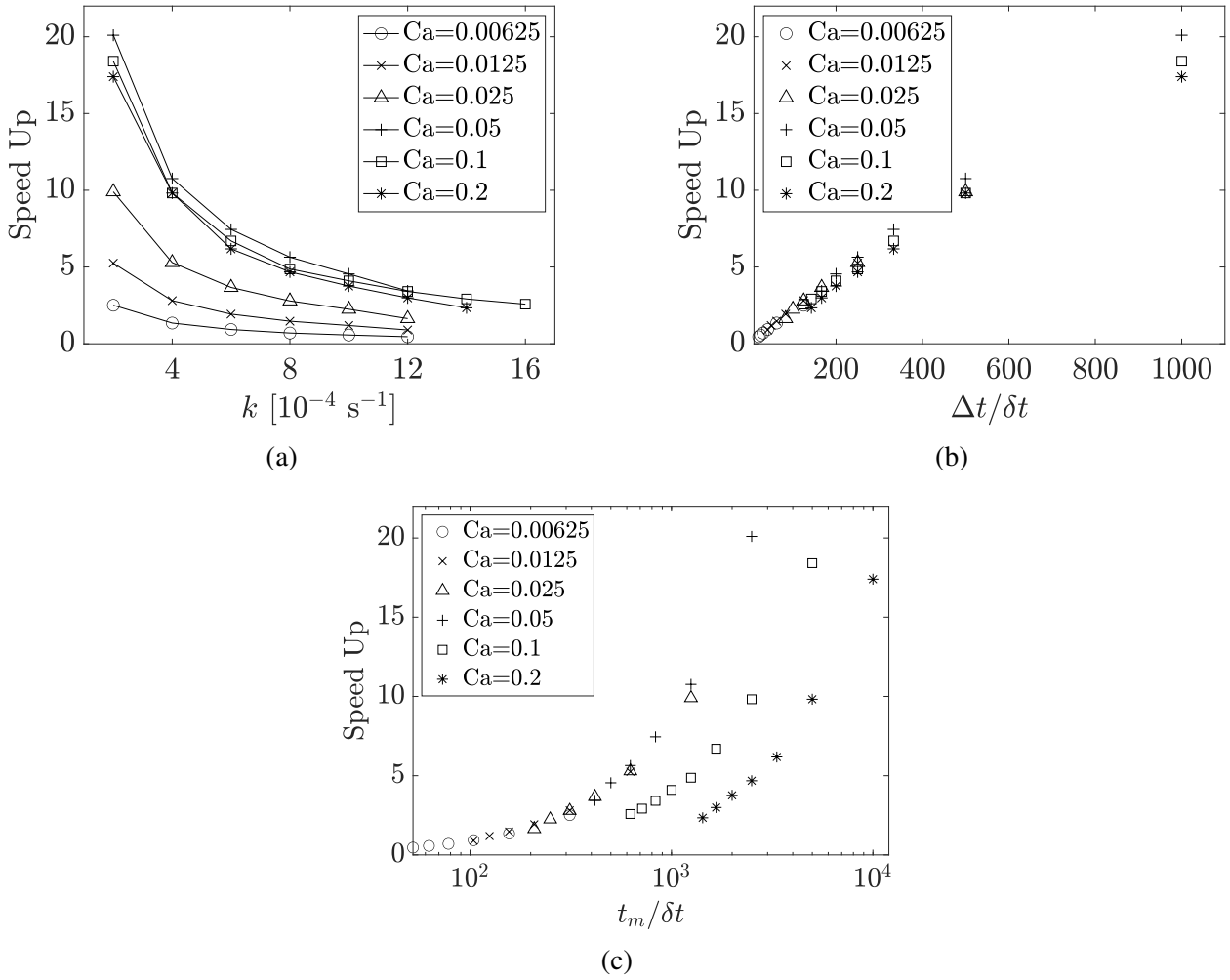

Fig. 22: The effect of physical parameters on the speed-up obtained from the dual time-stepping scheme. (a) The speed-up as a function of the shear rate, k. (b) The speed-up as a function of the ratio $\Delta t/\delta t$. (c) The speed-up as a function of the ratio $t_m/\delta t$.

step constraint for the DTS scheme given by Equation (132). The dimensionless time step for the standard LBM, $k\delta t$, is determined by k for a fixed value of Ca, whereas for the DTS scheme the dimensionless physical time step, $k\Delta t$, varies with Ca for a fixed value of k.

As would be expected, the size of the physical time step, Δt, is a strong predictor of the potential speed-up obtained by the DTS scheme. This relationship can be seen in Figure 22b, which plots the speed-up against the ratio $\Delta t/\delta t$. As can be seen in the figure, when $\Delta t/\delta t = 100$ a speed-up of 2 is achieved with the DTS scheme. The speed-up increases proportionally as $\Delta t/\delta t$ increases,

with peak efficiencies on the order of 20 for larger values of Ca. Based on this, the physical time scale and accuracy of the scheme should allow for increases of the physical time step by a factor of 100 or more for efficient application of the DTS scheme proposed here.

To demonstrate the limiting effects of the physical time scales and the accuracy requirements we have plotted the speed-up achieved by the DTS method against the ratio, $t_m/\delta t$ using a logarithmic scale for the x axis in Figure 22c. The ratio $t_m/\delta t$ indicates the separation of scale between the physical time scales and the LBM time step. From Equation (132) we see that for $\mathrm{Ca} \leq 0.05$ Δt is limited by the elastic time scale of the problem, whereas for $\mathrm{Ca} = 0.1$ and $\mathrm{Ca} = 0.2$ the time step is limited by the desired accuracy of the simulation. This relationship is apparent in the figure, where the speed-up curves for $\mathrm{Ca} \leq 0.05$ are nearly identical, while $\mathrm{Ca} = 0.1$ and $\mathrm{Ca} = 0.2$ have distinct speed-up curves. From the figure we recommend that $t_m/\delta t$ be on the order of 200 or more for efficient implementation of the DTS scheme proposed here.

While the speed-up achieved using the DTS scheme diminishes as k increases, for long simulations and non-spherical geometries k is limited by the stability constraint in Equation (118). Indeed, even for the spherical simulations discussed here $k > 1.2 \times 10^{-3}$ s^{-1} resulted in instability for some values of Ca. It should also be mentioned that, since small values of Ca reach equilibrium in a shorter time frame, declines in efficiency with the DTS scheme for small values of Ca are not a major concern because the standard LBM-IBM capsule model can simulate these in a reasonable amount of time. The most dramatic speed-up from the DTS scheme occur for $\mathrm{Ca} \geq 0.0125$ where simulation with the standard LBM-IBM capsule model can be much more expensive. In this regime, speed-up between 4 and 20 times the standard LBM-IBM capsule model are achieved.

4.4.2 EFFICIENCY FOR BICONCAVE SIMULATIONS

Simulating the dynamics of non-spherical capsules require much longer simulations because the capsules do not reach an equilibrium shape or flow field. These long simulations place more stringent constraints on the shear rate k, increasing the potential speed-up offered by the DTS scheme. We find that $k \leq 2 \times 10^{-4}$ s^{-1} is required for simulations long enough to capture the dynamics of biconcave capsules. For the standard LBM-IBM capsule model this results in a dimensionless time step of $k\delta t = 2 \times 10^{-5}$, which is far below the time step of the DTS scheme, which is set to $k\Delta t = 0.02$ for the simulations in this section.

To study the efficiency gains for capsule simulations where the flow does not reach a steady state, we have run simulations with a biconcave capsule for each of the cases illustrated in Figure 20a. As in the figure, the viscosity ratio was set to $\lambda = 4$, the bending stiffness was set to $E_b = 0.015$, and Skalak's modulus was set to $C = 5$. Simulations were run up to $kt = 30$ for Ca=0.25, Ca=0.4 and Ca=0.75. These three cases were chosen to demonstrate the effect that the different capsule behaviors has on the computational efficiency of the model, as Ca=0.25 results in a tumbling capsule, Ca=0.4 results in a transient regime, and Ca=0.75 results in a tank-treading capsule.

TABLE I: CPU time comparison for a biconcave capsule with $\lambda = 4$ and $E_b = 0.015$ for the cases shown in Figure 20a run until $kt = 30$.

	Ca=0.25		Ca=0.4		Ca=0.75	
	LBM	mgLBM	LBM	mgLBM	LBM	mgLBM
Time (s)	322,339	43,693	322,373	16,661	322,423	9147
Efficiency	1.0	7.4	1.0	19.3	1.0	35.2

The results for these tests can be seen in Table I. As can be seen, the efficiency gains of the simulation improve as the capillary number increases. It should be noted that unlike the spherical case above, the relationship between Ca and CPU time is not related to Δt. As mentioned above, $k\Delta t = 0.02$ for each value of Ca considered here. Instead the relationship between Ca and CPU time is due to the behavior of the capsule at the various capillary numbers as illustrated in Figure 20a.

In the tumbling regime at Ca=0.25, the position of the capsule within the fluid changes at each time step. This alters the flow field near the capsule, requiring more iterations of the multigrid LBM algorithm at each time step. In the transient regime at Ca=0.4, the capsule begins by tumbling before oscillating slightly around $\theta = 0$ with minimal deformation. Thus, after the tumbling phase is completed and changes in the capsule's inclination angle are reduced, variations in the flow field decrease allowing faster convergence with the multigrid LBM at each time step. Finally, in the

tank-treading regime at Ca=0.75, the capsule's angle remains roughly constant as the membrane rotates around the capsule. Thus, after reaching the steady shape, variation in the flow field is reduced between time steps, requiring fewer iterations of the fluid solver at each time step.

CHAPTER 5

CAPSULES IN A DC ELECTRIC FIELD

Validation of the numerical methods used for computation of the electric field and membrane electric forces is conducted by comparing our numerical simulations to results from small deformation theory and from the numerical simulations of Das and Thaokar [80]. In the absence of an external flow the deformation of an axisymmetric capsule will remain axisymmetric allowing for small deformation theory estimates of the deformation of the capsule [78, 79]. A schematic of capsule deformation due to a DC electric field can be seen in Figure 23. The capsule is placed in the center of the fluid domain, $\Omega^+ \cup \Omega^- = [0,H]^3$, with no-slip boundary conditions imposed at each of the fluid boundaries. A potential difference $-HE_0$ is applied in the y-direction, resulting in an approximately uniform electric field, $\mathbf{E} = E_0\hat{\mathbf{y}}$, far from the capsule. The fluid inside the capsule has permittivity, ε^-, and conductivity, σ^-, the ambient fluid has permittivity, ε^+, and conductivity, σ^+, and the membrane has permittivity, ε_m, and conductivity, σ_m.

Discontinuities in the material properties across the membrane interface result in electrical stresses that are balanced by the viscous and membrane stresses. The stress balance will result in capsule deformation and the development of a flow field near the membrane. The resulting flow will have a characteristic fluid velocity given by $v_c = \frac{\varepsilon^+ E_0^2}{\mu^+}$ and thus the Reynolds number for the flow is given by:

$$\mathrm{Re} = \frac{\rho a \varepsilon^+ E_0^2}{(\mu^+)^2}. \tag{137}$$

As in the the case of shear flow, the characteristic length is the capsule's equivalent radius, a, and thus, the characteristic time scale of the flow is obtained from a/v_c resulting in, $t_f = a\mu^+/\varepsilon^+ E_0^2$. For brevity we will denote dimensionless times as $\tilde{t} = t/t_f$ in this chapter. The charge relaxation times are the same as in Equation (25) and thus the electric Reynolds number, defined as the ratio of the characteristic time scale to the charge relaxation time scale is given by:

$$\mathrm{Re}_E = \frac{(\varepsilon^+ E_0)^2}{a\mu^+\sigma^+}. \tag{138}$$

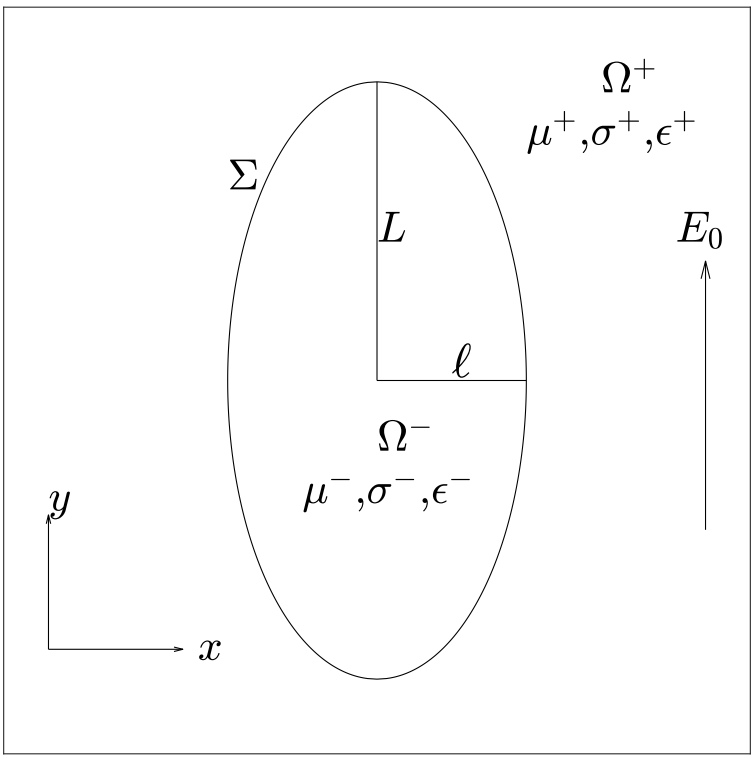

Fig. 23: A Schematic Depicting a Capsule in a Quiescent Flow.

The dimensionless versions of the elastic, charge relaxation, and membrane charging time scales are denoted by $\tilde{t}_m$, $\tilde{t}_e^+$, $\tilde{t}_e^-$, and $\tilde{t}_c$ respectively.

The capsule mesh used in this chapter is the same as was used in Chapter 4 and thus, the mesh consists of 5120 triangular elements composed of 2562 Lagrangian nodes. Resolution of the electric field requires a finer mesh resolution. Here we use an Eulerian grid with 161^3 nodes to discretize a domain of $[0,8.0a]$ in x, y and z, resulting in a step size of $\Delta x = \Delta y = \Delta z = 0.05a$. Each multigrid cycle uses a 6 grid level w-cycle multigrid schedule, with the coarsest grid having a resolution of 5^3. The time step was selected using Equation (133). The convergence criterion for the multigrid LBM was set to $\varepsilon = 10^{-5}$ based on the results from Section 3.8.1.

The MRT relaxation parameters s_4 and s_1 are set according to Equations (44) and (45) respectively. The parameters s_0, s_3, s_5, and s_7 correspond to the conserved moments and are thus set equal to zero. The remaining relaxation parameters are set equal to 1.8.

As in Chapter 4 the simulations below are conducted with a Reynolds number of $\mathrm{Re} = 0.05$. The simulations are normalized by setting $a = 1$ m, $\rho = 1$ kg$\cdot$m^{-3}, $\varepsilon^+ = 1$ F$\cdot$m^{-1}, $\sigma^+ = 1$ S$\cdot$m^{-1},

and $E_s = 1.6 \times 10^{-4}\ \mathrm{N \cdot m^{-1}}$. The remaining parameters are determined from the dimensionless parameters Re, Ca_E, E_b, λ, σ_r, ε_r, G_m, and C_m.

5.1 SPHERICAL CAPSULES

As in shear flow, initially spherical capsules in a DC electric field will reach an equilibrium shape provided that Ca_E is not large enough to induce capsule burst. The capsule's equilibrium shape will be that of either a prolate or oblate spheroid depending on the material properties of the fluids and the capsule. The inclination angle of the capsule will remain constant at $\theta = \frac{\pi}{2}$ for prolate capsules or $\theta = 0$ for oblate capsules, and thus the inclination angle will not be discussed for these simulations. In terms of the major and minor axis lengths, L and ℓ, from Figure 23, $L > \ell$ indicates that the capsule is elongated along the y axis and is a prolate spheroid. Conversely, $L < \ell$ indicates that the capsule is elongated along the x axis and is an oblate spheroid. Consequently, the deformation parameter, D_{xy}, will be positive for prolate deformation and negative for oblate deformation.

The deformation of the capsule depends on the ratios of the conductivities and permittivities, σ_r and ε_r, as well as the membrane capacitance, C_m, and conductance, G_m. For an electrically neutral membrane (i.e. $C_m = 0$ and $G_m = 0$) the capsule's equilibrium shape can be determined by looking at the ratio of the charge relaxation times, t_e^+/t_e^-, or equivalently, the ratio of the material parameters, σ_r/ε_r [62]. For $\sigma_r/\varepsilon_r > 1$, charge relaxation occurs more quickly inside the capsule, and thus charge accumulates on the inside of the capsule membrane, polarizing the capsule in the direction of the electric field. The capsule polarization results in electric stresses that drive a flow from the equator to the poles of the capsule, and prolate deformation occurs. For $\sigma_r/\varepsilon_r < 1$ charge relaxation occurs more quickly outside the capsule and charge accumulates on the outside of the capsule membrane, polarizing the capsule in the direction perpendicular to the electric field. In this case, the electric stresses drive a flow from the poles to the equator, resulting in oblate deformation.

5.1.1 NEUTRAL MEMBRANES

Capsules with electrically neutral membranes have been used to model the behavior of oil droplets [75, 76, 77] and coated droplets [78]. For spherical capsules at small capillary numbers, analytical estimates of the capsule's final deformation can be obtained [75, 76, 78]. Jumps in the

material properties across the interface result in the exertion of electrical stresses on the membrane. These stresses are balanced by the elastic and fluid stresses, resulting in fluid motion inside and outside the membrane [62]. The deformed capsule takes either a prolate or oblate spheroidal shape depending on whether σ_r/ε_r is greater than or less than 1, with the degree of deformation dependent on Ca_E.

In [78] Ouriemi and Vlahovska predict the equilibrium deformation of an inextensible capsule in a flow due to a DC electric field as follows:

$$D_{xy} = \frac{9}{32}\mathrm{Ca}_E \frac{(\sigma_r+1)^2 - 4\varepsilon_r}{(\sigma_r^2+2)^2}. \tag{139}$$

The equilibrium deformation of a Hookean membrane is given by:

$$D_{xy} = \frac{9}{32}\mathrm{Ca}_E \frac{11\sigma_r^2 + 18\sigma_r + 11 - 40\varepsilon_r}{(\sigma_r^2+2)^2}. \tag{140}$$

To the best of the present authors' knowledge the deformation of Hookean membranes in a DC electric field has not been derived for leaky dielectric fluids and thus a derivation is presented in Appendix C. The proposed scheme for electrohydrodynamic capsules is validated by comparing the final deformation from our numerical simulations to the linear estimates given by Equations (139) and (140). The simulations presented here were conducted with the time step, $\Delta t = 100a$, which results in a dimensionless time step $\Delta\tilde{t} = 0.02$.

In Figure 24 the deformation of an initially spherical neo-Hookean capsule with $\varepsilon_r = 1$, $\lambda = 1$, and $E_b = 0$ is studied for two different conductivity ratios. In the first case the conductivity ratio is set to $\sigma_r = 2$, indicating that the interior fluid is twice as conducting as the exterior fluid. In this case $\sigma_r/\varepsilon_r > 1$ and thus prolate deformation is expected. In the second case $\sigma_r = 0.5$, giving us $\sigma_r/\varepsilon_r < 1$ and thus, oblate deformation is expected to occur.

In Figure 24a the equilibrium deformation is plotted for simulations with electric capillary numbers, Ca_E ranging from 0.005 to 0.1. The numerical simulations are plotted against the predictions from linear theory for Hookean membranes, given by Equation (140), and Inextensible membranes, given by Equation (139). As can be seen from the figure, close agreement between

the numerical simulations is observed, especially for small values of Ca_E. In Figure 24b, the deformation parameter is plotted as a function of time for $\mathrm{Ca}_E = 0.025$, 0.05, and 0.1 for $\sigma_r = 2$ and $\sigma_r = 0.5$. As can be seen in the figure, the capsule deforms until reaching a constant deformation parameter.

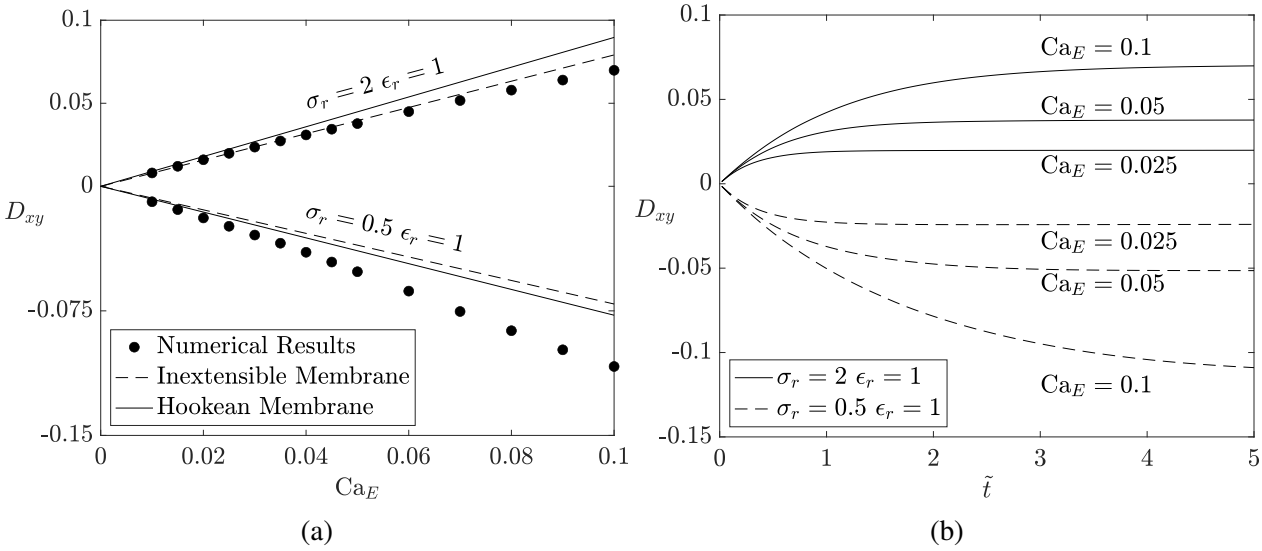

Fig. 24: The deformation of initially spherical capsules with $\sigma_r = 2$ and $\varepsilon_r = 1$ and $\sigma_r = 0.5$ and $\varepsilon_r = 1$. (a) The equilibrium deformation as a function of Ca_E. (b) D_{xy} as a function of time for various Ca_E.

In Figure 25 the deformation of capsules with a jump in the fluid permittivity is studied for initially spherical neo-Hookean capsules with $E_b = 0$, $\sigma_r = 1$ and $\lambda = 1$. In the first case considered $\varepsilon_r = 2$ giving us $\sigma_r/\varepsilon_r < 1$ and thus the capsules will undergo oblate deformation. Conversely, for $\varepsilon_r = 0.5$ the ratio $\sigma_r/\varepsilon_r > 1$ and the capsules will undergo prolate deformation. Figure 25a plots the deformation parameter of the capsule after it reaches its steady shape for Ca_E ranging from 0.01 to 0.1. The results are compared to the linear estimates for neo-Hookean and inextensible membranes, exhibiting close agreement. Figure 25b plots the deformation parameter as a function of time for $\mathrm{Ca}_E = 0.025$, 0.05, and 0.1.

In Figure 26 the deformation parameter of capsules with jumps in both the fluid conductivity

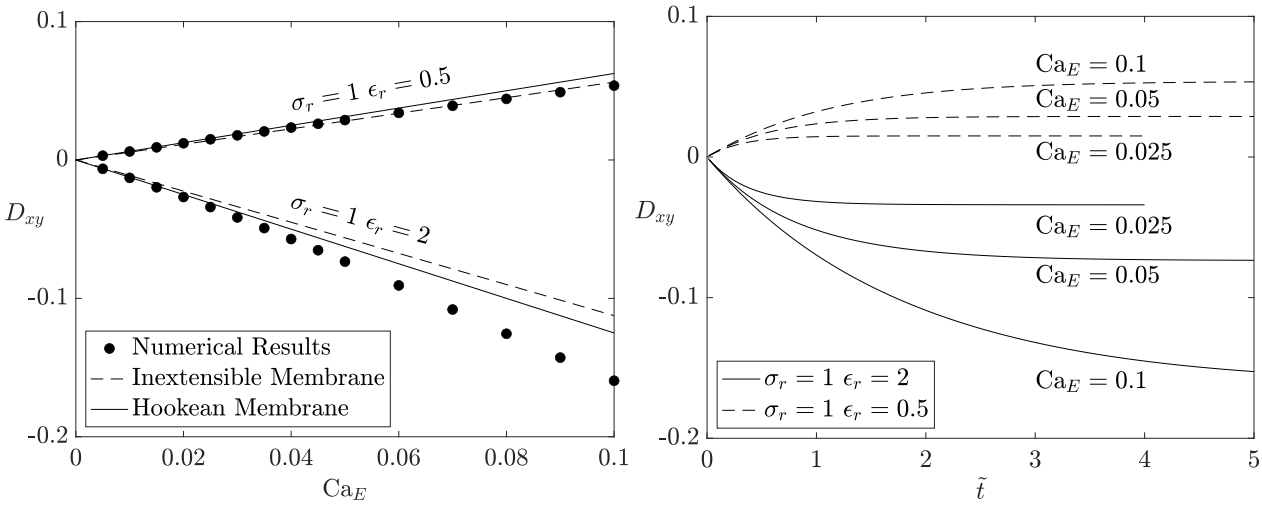

Fig. 25: The deformation of initially spherical capsules with $\sigma_r = 1$ and $\varepsilon_r = 2$ and $\sigma_r = 1$ and $\varepsilon_r = 0.5$. (a) The equilibrium deformation as a function of Ca_E. (b) D_{xy} as a function of time for various Ca_E.

and permittivity is studied for an initially spherical neo-Hookean membrane. As in Figures 24 and 25, the viscosity ratio is fixed at $\lambda = 1$ and $E_b = 0$. For $\sigma_r = 4.75$ and $\varepsilon_r = 3.5$ we have $\sigma_r/\varepsilon_r > 1$ and prolate deformation is expected, whereas for $\sigma_r = 1.75$ and $\varepsilon_r = 3.5$, we have $\sigma_r/\varepsilon_r < 1$ and oblate deformation is expected. In Figure 26a the deformation parameter at equilibrium is plotted as a function of the electric capillary number and compared with the linear estimates from Equations (139) and (140). The simulations show close agreement with the linear theory. It is interesting to note that the cases where prolate deformation is observed, the linear theory for inextensible membranes agrees most closely with the numerical results, whereas when oblate deformation is observed, the linear theory for Hookean membranes agrees most closely with the numerical results. Figure 26b is a plot of the deformation parameter as a function of time for $\mathrm{Ca}_E = 0.025$, 0.05, and 0.1.

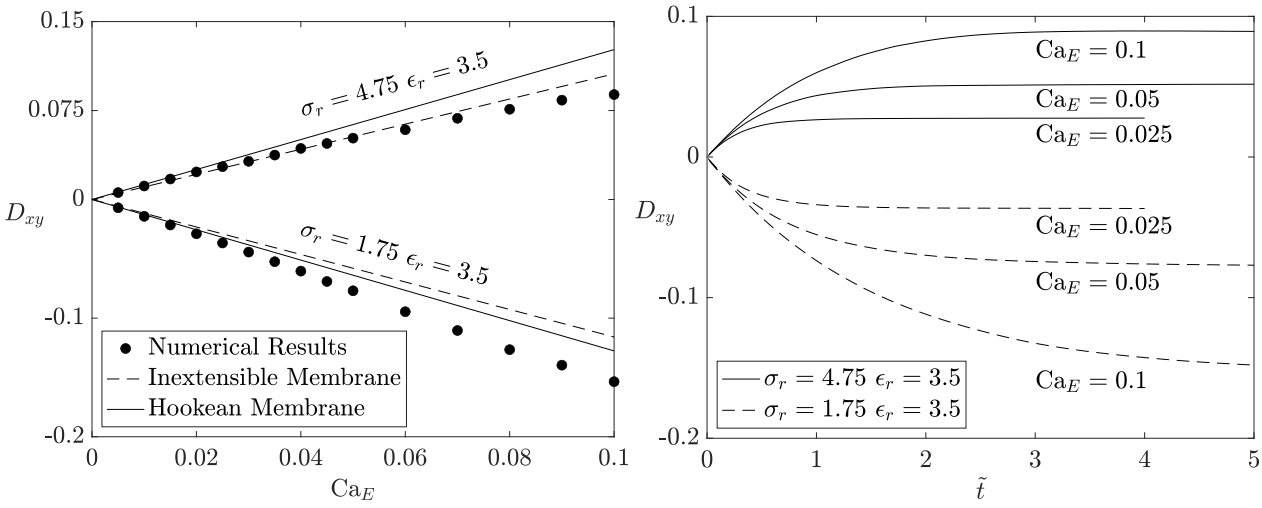

Fig. 26: The deformation of initially spherical capsules with $\sigma_r = 1.75$ and $\varepsilon_r = 3.5$ and $\sigma_r = 4.75$ and $\varepsilon_r = 3.5$. (a) The equilibrium deformation as a function of Ca_E. (b) D_{xy} as a function of time for various Ca_E.

5.1.2 ELECTRICALLY CHARGED MEMBRANES

The transmembrane potential model proposed by DeBruin and Krassowska in [64] considers the membrane's electrical response due to the membrane's capacitance, C_m, and conductance, G_m. Analytical studies on the effects of the transmembrane potential on vesicles were studied by Vlahovska and co-workers in [131, 65, 62]. For a fixed value of C_m, large values of G_m cause the capsule to behave as an electrically neutral membrane, whereas small values of G_m, cause the membrane to acts as a capacitor, shielding the interior fluid from the electrical field. For a non-conducting membrane, $G_m = 0$, once the membrane is fully charged, the interior fluid is perfectly shielded from the external electric field and prolate deformation occurs regardless of the conductivity ratio [80]. Even for the case of $G_m = 0$, however, the conductivity ratio will affect the transient dynamics of the membrane deformation [80]. For $\sigma_r < 1$ the capsule will initially undergo an oblate deformation as in the case for a neutral membrane. Once the membrane is fully charged, however, the capsule will transition to a steady prolate spheroid.

Validation of the IIM model of the transmembrane potential is done by comparing the steady

state deformation of a spherical neo-Hookean capsule obtained through the proposed numerical scheme to the steady-state deformation predicted by Das and Thaokar in [80]. For the parameters $G_m = 0$, $C_m = 50$, $\lambda = 1$, $E_b = 0$, and $\sigma_r = 0.1$ the steady state deformation is given by:

$$D_{xy} = 0.703\text{Ca}_E. \tag{141}$$

In Figure 27a, the steady deformation obtained from numerical simulations by the present authors are plotted against the electric capillary number. The numerical results are compared with Equation (141) and with the boundary element simulations published by Das and Thaokar in [80]. The numerical results show close agreement with the linear theory at small values of Ca_E and exhibit close agreement with the numerical simulations in [80] for all Ca_E.

In Figure 27b the deformation parameter is plotted as a function of dimensionless time for the parameters from Figure 27a for $\text{Ca}_E = 0.05$ and $\text{Ca}_E = 0.1$ for $\sigma_r = 0.1$ and $\sigma_r = 10$. As is predicted by the theory, the equilibrium value of D_{xy} for $\sigma_r = 0.1$ and $\sigma_r = 10$ are identical. The transient dynamics of the simulations with $\sigma_r = 0.1$ are affected by the charging of the membrane and the resulting flow field. Initially, the membrane is uncharged and the dynamics are identical to a neutral membrane. For $\sigma_r = 10$ prolate deformation, indicated by $D_{xy} > 0$, occurs. For $\sigma_r = 0.1$ oblate deformation, indicated by $D_{xy} < 0$, occurs. As the membrane charges, the capsule polarizes parallel to the electric field, resulting in a steady prolate shape irrespective of σ_r.

In Figure 28 the deformation of capsules with $\sigma_r = 0.1$ and $\sigma_r = 10$ is plotted for $\text{Ca}_E = 0.5$, $C_m = 50$, $G_m = 0$, $\varepsilon_r = 1$, $\lambda = 1$, and $E_b = 0$. The large value of Ca_E is selected to investigate the large deformation regime where the linear approximations from Equation (141) are not suitable. In Figure 28a the deformation parameter is plotted as a function of time for $\sigma_r = 0.1$ and $\sigma_r = 10$. As in the small deformation simulations, for $\sigma_r = 0.1$ the capsule initially undergoes oblate deformation before transitioning to a prolate deformation as the membrane charges. In Figure 28b the equilibrium shape for capsules with $\sigma_r = 0.1$, $\varepsilon_r = 1$, $\lambda = 1$, $E_b = 0$, and $C_m = 50$, and $G_m = 0$ are plotted for various values of Ca_E. As expected increasing the electric capillary number results in increased deviation from the initial spherical capsule.

In Figure 29 the capsule profile, flow streamlines, and membrane electric forces at the z-coordinate centerline in the $x-y$ plane are plotted at various times for $\text{Ca}_E = 0.5$, $\sigma_r = 10$, $\varepsilon_r = 1$,

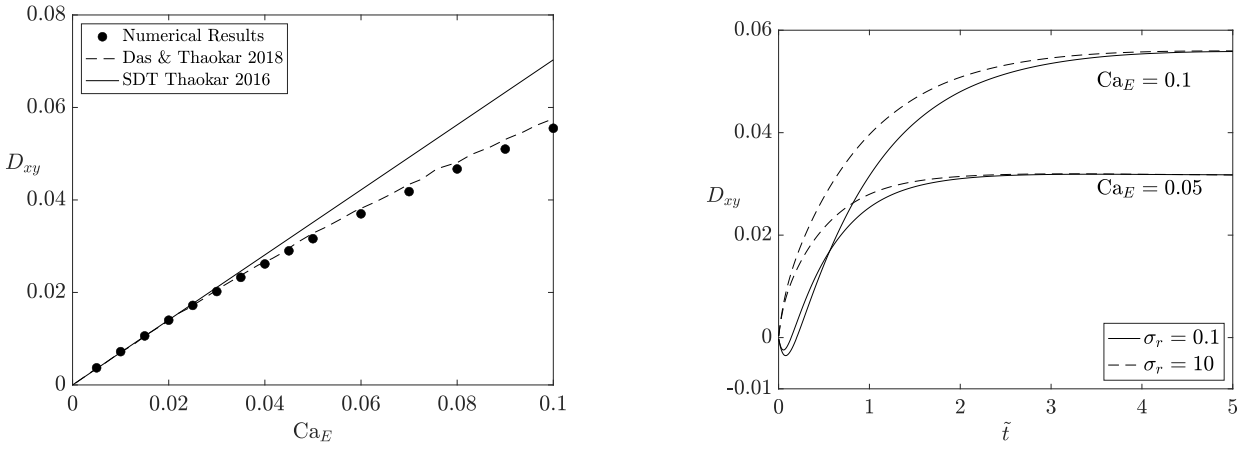

(a) (b)

Fig. 27: The deformation of initially spherical capsules with $C_m = 50$ and $G_m = 0$. (a) The equilibrium deformation of a capsule with conductivity ratio $\sigma_r = 0.1$ as a function of the electrical capillary number, Ca_E. (b) The evolution of D_{xy} for capsules with $\sigma_r = 0.1$ and $\sigma_r = 10$ for Ca_E=0.05 and $\mathrm{Ca}_E = 0.1$. The remaining parameters are fixed at $\varepsilon_r = 1$, $\lambda = 1$, $E_b = 0$.

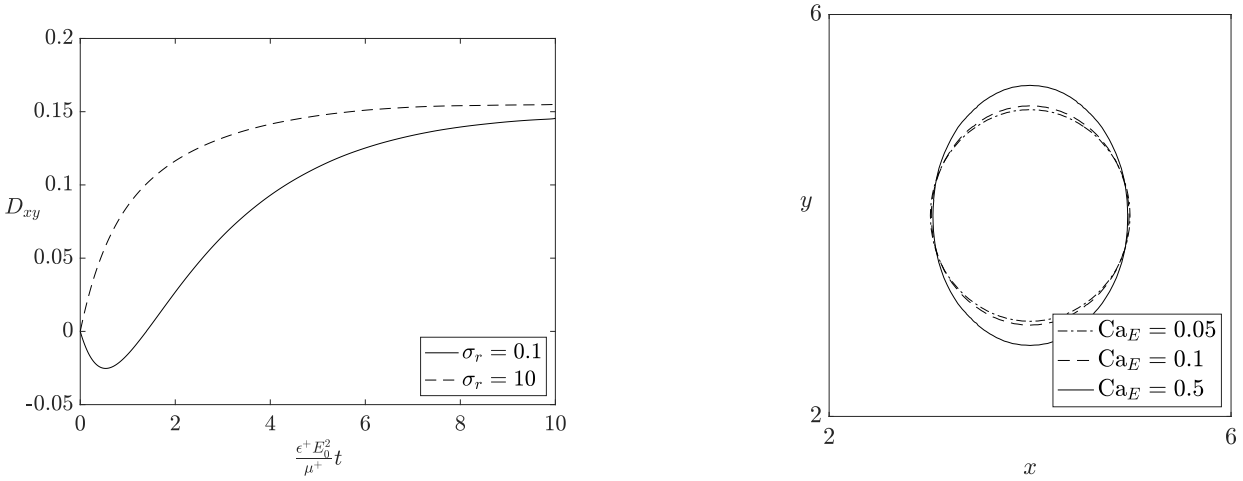

(a) (b)

Fig. 28: The deformation and steady shape of initially spherical capsules with $C_m = 50$ and $G_m = 0$. (a) Evolution of D_{xy} for capsules with $\sigma_r = 0.1$ and $\sigma_r = 10$ for $\mathrm{Ca}_E = 0.5$. (b) Equilibrium shape for capsules with $\sigma_r = 10$ for various values of Ca_E. The remaining parameters are fixed at $\varepsilon_r = 1$, $\lambda = 1$, $E_b = 0$.

$\lambda = 1$, $E_b = 0$, $C_m = 50$, and $G_m = 0$. The flow streamlines are denoted by the blue arrows and the electrical forces are denoted by the red arrows. In Figure 29a, at $\tilde{t} = 0$, the streamlines flow from

the equators to the poles of the capsule. The membrane is uncharged and thus behaves as a neutral membrane which, for $\sigma_r/\varepsilon_r > 1$, results in tensile electric stress at the poles that causes prolate deformation. In Figure 29b and 29c the capsule profile, flow streamlines, and electrical forces are plotted at $\tilde{t} = 0.5$ and $\tilde{t} = 0.7$, respectively. The effects of the charging membrane appear as a compressive force at the equators of the capsule. In Figures 29e and 29f the capsule has reached equilibrium, with the compressive electric forces at the equator in balance with the compressive elastic forces, denoted by the black arrows, at the poles. The stress balance results in a stationary fluid indicated in the figures by the absence of streamlines.

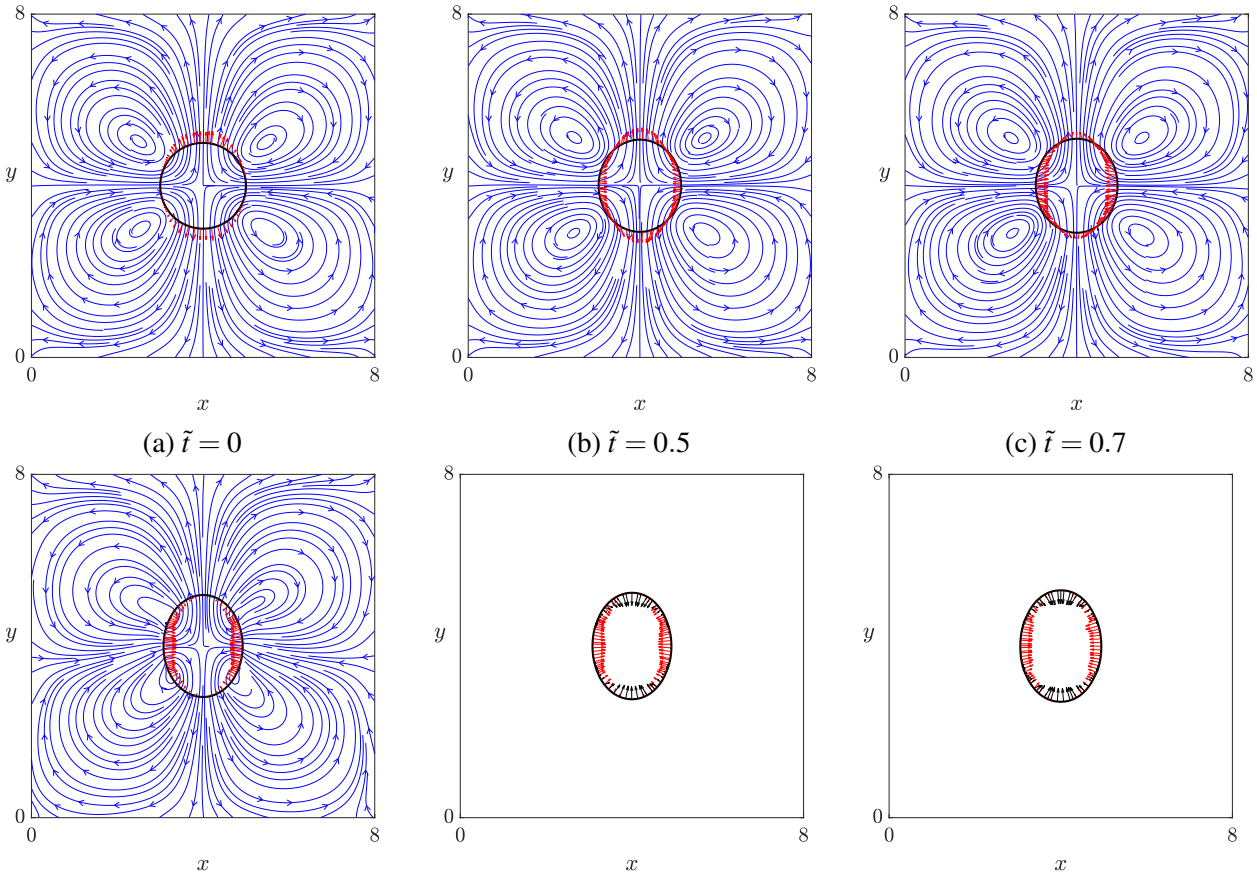

(a) $\tilde{t} = 0$ (b) $\tilde{t} = 0.5$ (c) $\tilde{t} = 0.7$

(d) $\tilde{t} = 2.5$ (e) $\tilde{t} = 5$ (f) $\tilde{t} = 10$

Fig. 29: The flow field and membrane forces for an initially spherical capsule with $\mathrm{Ca}_E = 0.5$, $\sigma_r = 10$, $\varepsilon_r = 1$, $\lambda = 1$, $E_b = 0$, $C_m = 50$, and $G_m = 0$ at various times. The figure depicts the capsule profile, streamlines (blue arrows), electric forces (red arrows) and elastic forces (black arrows).

In Figure 30 the capsule profile, flow streamlines, and membrane electric forces at the z-coordinate centerline in the $x-y$ plane are plotted at various times for $\mathrm{Ca}_E = 0.5$, $\sigma_r = 0.1$, $\varepsilon_r = 1$, $\lambda = 1$, $E_b = 0$, $C_m = 50$, and $G_m = 0$. The flow streamlines are denoted by the blue arrows, the electrical forces by the red arrows, and the elastic forces by the black arrows. In Figure 30a, the flow at $\tilde{t} = 0$ is plotted, where it can be seen to flow from the poles to the equators of the capsule. At $\tilde{t} = 0$ the membrane is uncharged and thus the capsule behaves as a neutral membrane which, since $\sigma_r/\varepsilon_r < 1$, results in compressive electric stresses at the poles that cause oblate deformation. In Figure 30b, at $\tilde{t} = 0.5$, the effects of the charging membrane appear as compressive forces at the equator. The competition between electric and elastic forces drives fluid circulation inside the capsule. In Figure 30c the capsule profile, flow streamlines, and electrical forces are plotted at $\tilde{t} = 0.7$. The interior circulation is seen to have caused the flow to change directions, with the fluid now flowing from the equator to the poles. As in the case with $\sigma_r = 10$, the effect of the charged membrane appears as a compressive force at the equators. In Figures 30d and 30e the compressive forces at the pole disappear, while the compressive forces at the equator result in prolate deformation. In Figure 30f the capsule has reached equilibrium, with the compressive electric forces at the equator in balance with the compressive elastic forces at the poles. The stress balance results in a stationary fluid indicated here by the absence of streamlines.

In Figure 31 the electric field is plotted at the initial and final time steps to demonstrate the effect of the transmembrane potential on the electric field for a capsule with $\sigma_r = 0.1$. Figure 31a is a plot of the initial electric field. As mentioned above, the membrane is uncharged at $\tilde{t} = 0$ and thus, the electric field is the same as the field expected for a neutral membrane, which can be computed analytically as follows [75]:

$$\mathbf{E}^-(\phi) = \frac{3}{\sigma_r + 2} E_0 \hat{\mathbf{y}}. \tag{142}$$

Figure 31b is a plot of the electric field at $\tilde{t} = 10$ when the membrane is fully charged. As can be seen in the figure, the charged membrane acts as a capacitor, shielding the interior fluid from the electrical field, resulting in an approximately constant electric potential of $\psi^- = -4aE_0$, and thus an electric field of approximately 0, inside the capsule.

Figure 31c plots the transmembrane potential as a function of the polar angle for a capsule

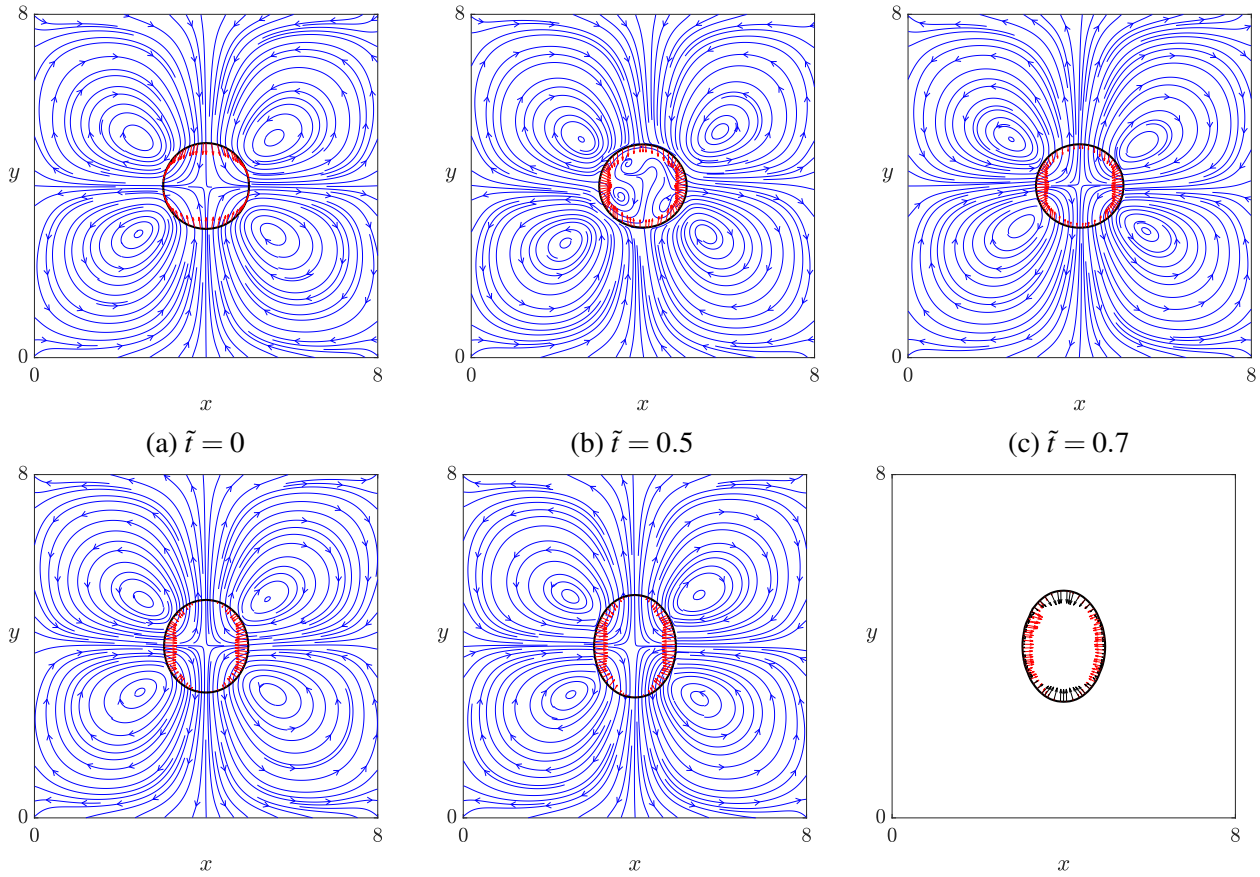

(a) $\tilde{t} = 0$ (b) $\tilde{t} = 0.5$ (c) $\tilde{t} = 0.7$

(d) $\tilde{t} = 2.5$ (e) $\tilde{t} = 5$ (f) $\tilde{t} = 10$

Fig. 30: The flow field and membrane forces for an initially spherical capsule with $\mathrm{Ca}_E = 0.5$, $\sigma_r = 0.1$, $\varepsilon_r = 1$, $\lambda = 1$, $E_b = 0$, $C_m = 50$, and $G_m = 0$ at various times. The figure depicts the capsule profile, streamlines (blue arrows), electric forces (red arrows) and elastic forces (black arrows).

with $\sigma_r = 0.1$. In the figure, the polar angle is measured from the x axis with $-\pi/2$ and $\pi/2$ corresponding to the negative and positive y axes, respectively. As can be seen in the figure, the transmembrane potential is initially zero. As $\tilde{t}$ increases the transmembrane potential approaches an approximately sinusoidal shape. This agrees with the analytical theory for perfectly spherical membranes in a DC electric field where it has been shown [65] that the transmembrane potential of a fully charged membrane can be expressed in terms of the polar angle, ϕ, as follows:

$$V_m(\phi) = -\frac{3}{2}\cos\phi. \tag{143}$$

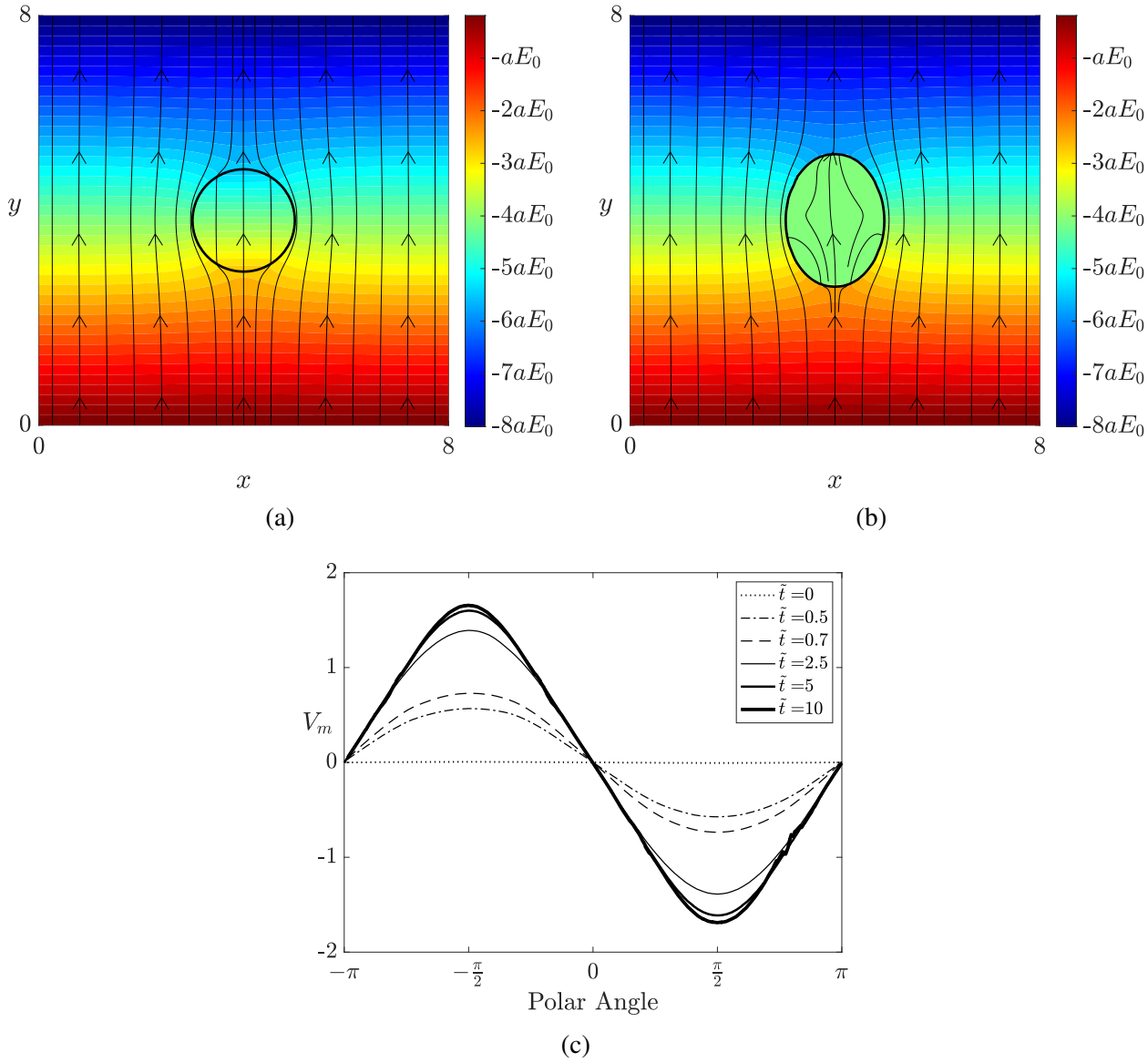

Fig. 31: The electric field and transmembrane potential of an initially spherical capsule with $\mathrm{Ca}_E = 0.5$, $\sigma_r = 0.1$, $\varepsilon_r = 1$, $\lambda = 1$, $E_b = 0$, $C_m = 50$, and $G_m = 0$ at various times. The profile of the electric potential and the field lines at (a) $\tilde{t} = 0$ and (b) $\tilde{t} = 10$. (c) The transmembrane potential as a function of the polar angle for various times.

The transmembrane potential can be seen to deviate from Equation (143), as the maximum in our figure is approximately 1.57, which is due to the prolate spheroidal shape of our capsule.

5.2 PROLATE OBLATE PROLATE TRANSITION

As demonstrated above, a charged, non-conducting membrane will fully shield the interior fluid from the external electric field, resulting in compressive electric stresses at the equator of the capsule. At steady state, these stresses cause the capsule to deform to a prolate spheroid irrespective of the conductivity ratio. For an initially prolate capsule with $\sigma_r/\varepsilon_r < 1$, the capsule will initially experience compressive electric forces at the poles. This results in a flow from the poles to the equator and deformation towards an oblate capsule. As the membrane charges, compressive electric stresses develop at the equators, causing the flow to reverse directions. The resulting flow from the equator to the poles causes deformation towards a steady prolate capsule. It has been shown for vesicles [67, 72, 74] that, for strong enough electric fields, this will result in an initially prolate capsule deforming into an oblate capsule before returning to a prolate capsule after the membrane charges, in a phenomenon known as the prolate-oblate-prolate (POP) transition.

Given the similarity between capsules and vesicles, it is expected that capsules would also exhibit the POP transition however, to the best of the present authors' knowledge, simulations of the POP transition for capsules have not yet been reported. In this section we will present simulations of the POP transition for elastic capsules to further demonstrate the efficacy of our numerical scheme. The field strength required for the POP transition is dependent on the initial shape, as well as the dimensionless parameters σ_r, ε_r, λ, C_m, and G_m [72]. In this section we consider a prolate spheroid with $b/a = 10/9$ in Equation (135) and dimensionless parameters $\sigma_r = 0.1$, $\varepsilon_r = 1$, $E_b = 0$, $\lambda = 1$, $C_m = 50$, and $G_m = 0$. For these parameters the field strength required for the POP transition was between $\mathrm{Ca}_E = 1$ and $\mathrm{Ca}_E = 2$. As in the previous section the Reynolds number is set to Re$= 0.05$.

In Figure 32a the deformation parameter of the capsule is shown as a function of dimensionless time, $\tilde{t}$. Initially $D_{xy} > 0$, indicating the prolate shape of the capsule. As the simulation commences D_{xy} decreases, reaching a minimum approximately -0.02 before increasing back towards the positive values exhibited by a prolate spheroid. After reaching a minimum at approximately $\tilde{t} = 1.5$ D_{xy} is seen to increase for the duration of the simulation.

In Figure 32b the transmembrane potential is plotted as a function of the capsule's polar angle.

As in Figure 31c, the polar angle is measured from the x-axis, with $-\pi/2$ and $\pi/2$ corresponding to the negative and positive y-axes respectively. During the early stages of deformation, the transmembrane potential exhibits the sinusoidal shape seen for spheres. However as deformation continues the amplitude of the transmembrane potential increases and the shape deviates from a sinusoidal wave. This increase in amplitude is caused by the prolate deformation, which causes the capsule membrane to elongate along the y axis. As the capsule membrane elongates in the y-coordinate direction the potential outside the capsule at $\phi = \pm\pi/2$ increases, requiring a larger transmembrane potential to offset the jump in potential between the interior and exterior fluids.

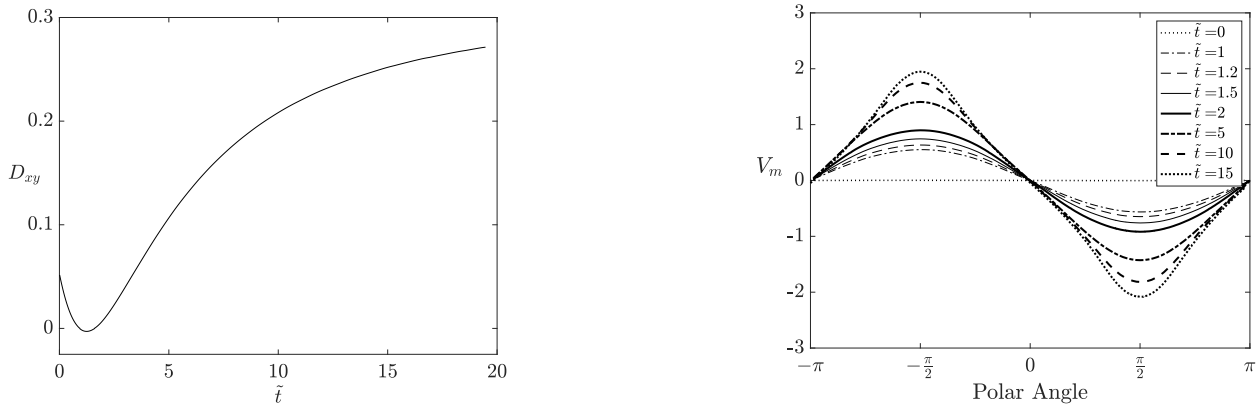

(a) (b)

Fig. 32: The deformation parameter and transmembrane potential for a capsule during the prolate-oblate-prolate transition. (a) D_{xy} as a function of time for an initially prolate capsule undergoing the prolate-oblate-prolate transition. (b) Transmembrane potential as a function of polar angle for various dimensionless times $\tilde{t}$. The dimensionless parameters in both figures are given by $\mathrm{Ca}_E = 2$, $\sigma_r = 0.1$, $C_m = 50$, $G_m = 0$, and $\varepsilon_r = 1$.

Figure 33 contains a quiver plot of the z centerline of the fluid velocity field in the $x-y$ plane and the electric forces exerted on the capsule membrane. In Figure 33a the initial velocity field is seen to stream from the poles to the equators, as expected for an uncharged membrane with $\sigma_r/\varepsilon_r < 1$. Compressive electrical stresses at the poles cause the capsule to deform towards an oblate spheroid. In Figures 33b and Figures 33c the flow field at $\tilde{t} = 1$ and $\tilde{t} = 1.2$ is plotted. Circulation inside the capsule develops, with the magnitude of the velocity of the circulating fluid

increasing between $\tilde{t} = 1$ and $\tilde{t} = 1.2$. The effect of the charging membrane can also be seen by the compressive electrical stresses at the equators. Figure 33d shows the flow field at $\tilde{t} = 1.5$, where the internal circulation has caused the flow to reverse directions. In Figure 33e and 33f the flow has fully reversed directions and is now streaming from the equators to the poles. In Figure 33f the capsule at $\tilde{t} = 5$ can be seen to have assumed a clear prolate shape. The fluid is still flowing from the equators to the poles and thus the elongation of capsule continues. In Figure 33g the fluid velocity at $\tilde{t} = 15$ can be seen to have decreased as indicated by the length of the flow vectors in the quiver plot. This agrees with the time evolution of the deformation parameter seen in Figure 32a, where it can be seen that at $\tilde{t} = 15$ the capsule has undergone the most rapid phase of deformation and is approaching a steady shape.

Figure 34 contains contour plots of a cross section of the electric potential and the field lines of the electric field at the center of the z-coordinate domain in the $x - y$ plane for the POP transition at various dimensionless times. Figure 34a shows the initial electric potential for a prolate spheroid. Figures 34b, 34c, and 34c show the electric potential at $\tilde{t} = 1$, 1.2, and 1.5, where the decreasing number of contour lines inside the capsule indicate that the electric potential is gradually approaching a constant value inside the capsule. The constant electric potential inside the capsule is caused by the charging of the membrane, which acts as a capacitor and shields the interior fluid. In Figures 34e and 34f the potential inside the fluid is seen to reach an approximately constant value of $-4aE_0$. In Figure 34g the electric potential and electric field at $\tilde{t} = 15$ are depicted. In this figure the effect of the prolate deformation on the transmembrane potential can be seen. The capsule has elongated along the y-axis and the jump in potential between the interior and exterior fluids at $\phi = \pm\pi/2$ is on the order of $2aE_0$, requiring a transmembrane potential of approximately $2aE_0$ to shield the interior fluid, as seen in Figure 32b.

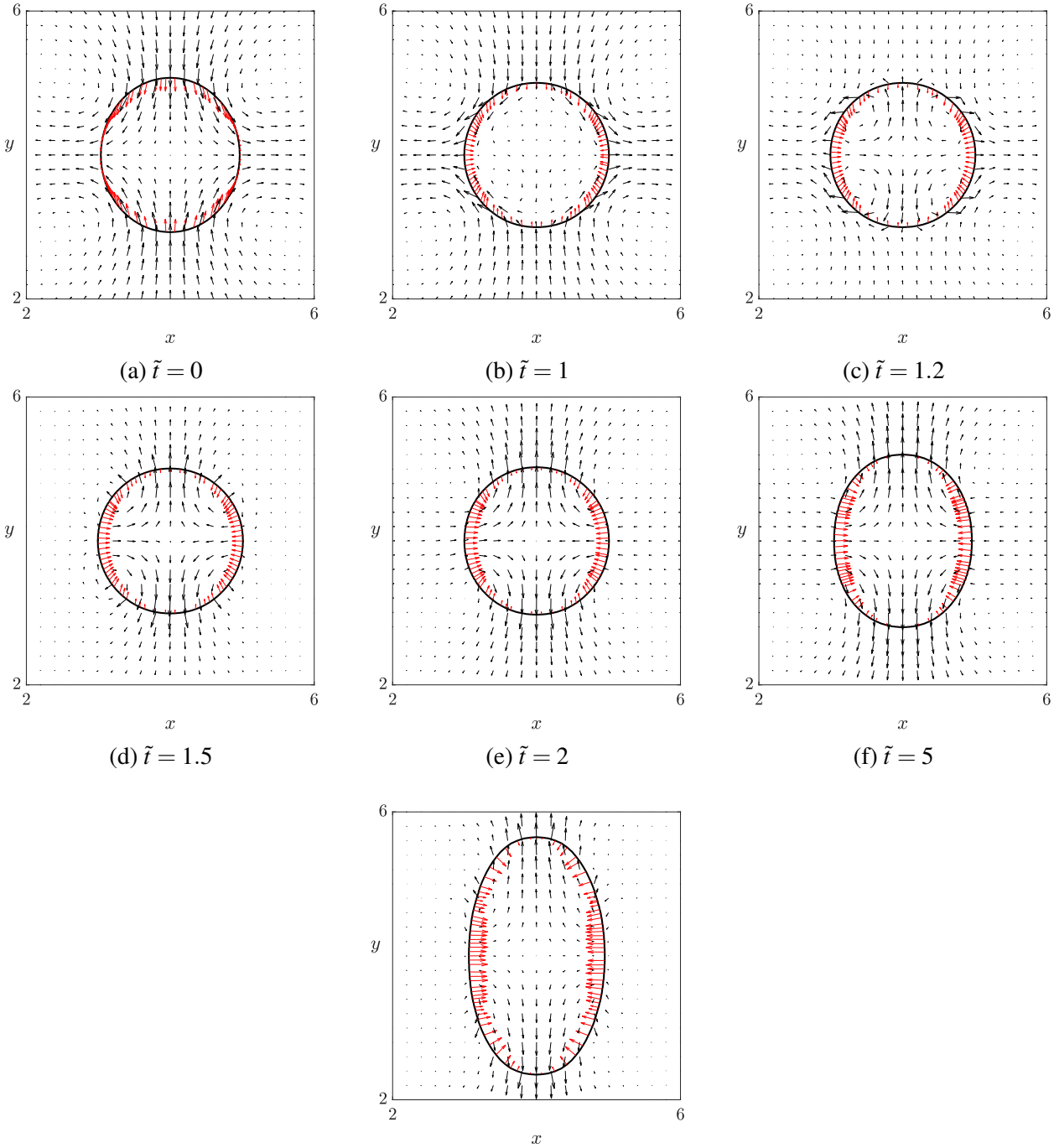

(a) $\tilde{t} = 0$ (b) $\tilde{t} = 1$ (c) $\tilde{t} = 1.2$

(d) $\tilde{t} = 1.5$ (e) $\tilde{t} = 2$ (f) $\tilde{t} = 5$

(g) $\tilde{t} = 15$

Fig. 33: The velocity field and electrical forces during the prolate-oblate-prolate transition. The velocity field is denoted by the black arrows and the electrical forces are denoted by the red arrows. The dimensionless parameters for the simulation are given by $\mathrm{Ca}_E = 2$, $E_b = 0$, $\lambda = 1$, $C_m = 50$, and $G_m = 0$.

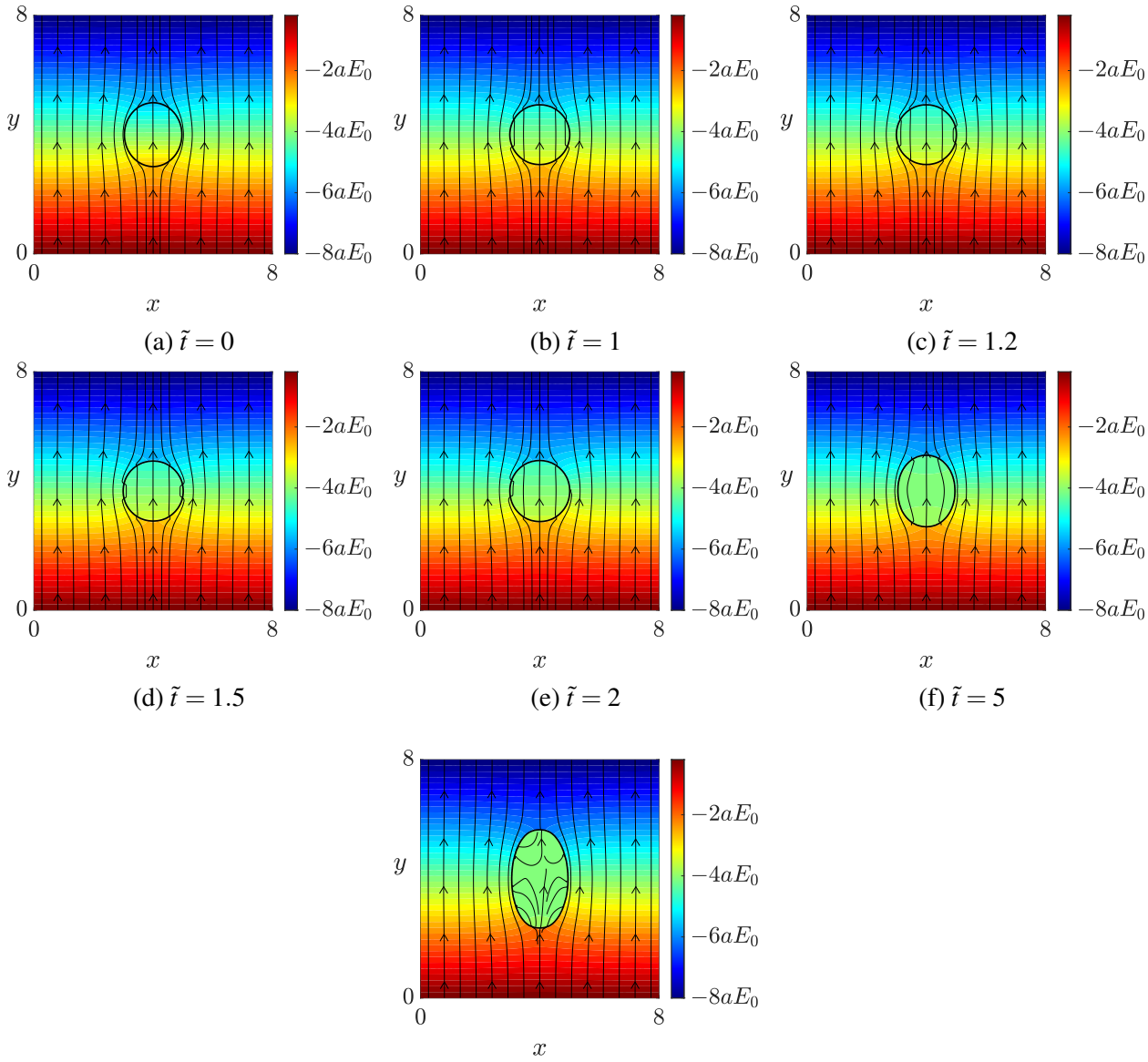

(a) $\tilde{t} = 0$ (b) $\tilde{t} = 1$ (c) $\tilde{t} = 1.2$

(d) $\tilde{t} = 1.5$ (e) $\tilde{t} = 2$ (f) $\tilde{t} = 5$

(g) $\tilde{t} = 15$

Fig. 34: Electric potential and electric field lines of an initially prolate capsule during the prolate-oblate-prolate transition. The parameters for the simulation are the same as those in Figure 33.

CHAPTER 6

COMBINED EFFECTS OF A SHEAR FLOW AND AN ELECTRIC FIELD

In shear flow capsules deform towards an oblate spheroid aligning themselves with the streamlines of the flow. In a DC electric field capsules with a charged membrane will deform towards a spheroid aligned with the electric field. Thus, for an electric field applied perpendicular to the shear flow the two effects will counteract one another with the dynamics dependent on the relative strength of the forces [75]. For a capsule in a combined DC electric field and shear flow the relation of the electric and viscous stresses is characterized by the mason number:

$$\mathrm{Mn} = \frac{\varepsilon E_0^2}{k\mu^+}.$$

Large values of Mn indicate an increased importance of the electric field on the overall dynamics, whereas smaller values of Mn indicate an increased importance on the shear flow.

To the best of the present authors' knowledge, the only study of capsules under the combined effects of a shear flow and a DC electric field is the small deformation analysis by Ha and Yang [75]. Ha and Yang considered electrically neutral spherical capsules and found that the addition of an electric field resulted in greater deformation, while the orientation of the capsule depended upon the ratio σ_r/ε_r. As in Chapter 5 when $\sigma_r/\varepsilon_r > 1$ the capsule is polarized along the direction of the electric field, resulting in an inclination angle closer to the y axis for a given shear rate. Conversely, when $\sigma_r/\varepsilon_r < 1$ the capsule polarization is perpendicular to the electric field, resulting in an inclination angle nearer the x axis.

In this work we consider the electrical properties of the membrane, which complicates these dynamics. The membrane capacitance and conductance result in a time-dependent jump in the potential, which impacts the polarization and deformation of the capsule. As demonstrated in Chapter 5 the membrane capacitance shields the interior fluid from the electric field. For nonconducting membranes this manifests itself as a compressive force at the equators which results in a steady prolate capsule independent of the ratio σ_r/ε_r. In the absence of an external flow, Das and Thaokar found that the membrane conductance counteracts the effects of the membrane capacitance, with

the behavior of conducting membranes approaching that of neutral membranes as the membrane conductance increases [80]. As will be demonstrated below, the competing dynamics of the membrane conductance and capacitance play a significant role in the equilibrium behavior of capsules in shear flow.

A number of numerical studies have been conducted for charged vesicles under the combined effects of a shear flow and an electric field [67, 72, 74]. For tumbling vesicles the electrical field dampens the tumbling motion, with strong fields causing the vesicle to transition from the tumbling to tank-treading regime. Furthermore, McConnell et al. reported an asymmetry of the tumbling motion in electric fields, as the charged membrane's polarization acts to resist the tumbling motion when it opposes the field and then subsequently reinforce the tumbling motion when the polarization is aligned with the field [67]. For vesicles in the tank-treading mode the electric field was shown to increase the inclination angle at which the vesicle reaches equilibrium [72].

While the behavior of vesicles and capsules are qualitatively similar, the area incompressible nature of vesicle membranes prohibits deformation of spherical vesicles. Spherical capsules, however, can exhibit large deformation under a variety of forces [28]. The dynamics of spherical capsules can provide insights into the role of the various dimensionless parameters, and thus this work will begin with a study of the parameter space for spherical capsules. This study will elucidate the role of the various parameters on the dynamics of capsules under the effects of a combined shear flow and DC electric field. Following this we will examine biconcave capsules in shear flow, with particular attention paid to the electric field's effect on the inclination angle in the tumbling and tank-treading motions.

A diagram of the simulation configuration is shown in Figure 35. The capsule is placed in the center of the fluid domain, $\Omega^+ \cup \Omega^- = [0,H]^3$. The ambient shear flow is given in terms of the shear rate, k as follows:

$$\mathbf{v} = \left[k\left(y - \frac{1}{2}H\right), 0, 0 \right]^{\mathrm{T}}. \tag{144}$$

The boundary conditions on the fluid are periodic in the x and z coordinates and are $v_x = -\frac{1}{2}Hk$ at $y = 0$ and $v_x = \frac{1}{2}Hk$ at $y = H$. A potential difference $-HE_0$ is applied in the y-direction, resulting in an approximately uniform electric field, $\mathbf{E} = E_0\hat{\mathbf{y}}$, far from the capsule. The fluid inside the capsule has permittivity, ε^-, and conductivity, σ^-, the ambient fluid has permittivity, ε^+, and conductivity,

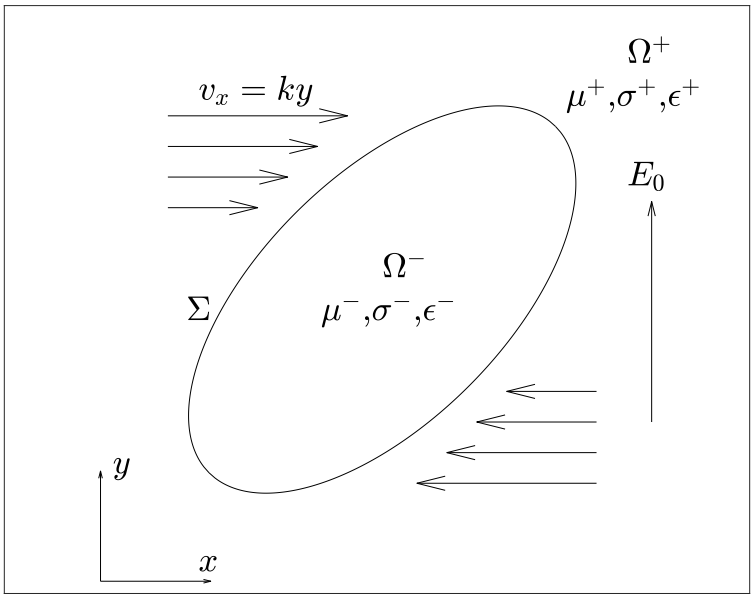

Fig. 35: Schematic of a capsule in a shear flow with a uniform DC electric field.

σ^+, and the membrane has permittivity, ε_m, and conductivity, σ_m.

As in Chapters 4 and 5, the simulations below are conducted with a Reynolds number of $\mathrm{Re} = 0.05$. The shear flow is normalized in the same manner as Chapter 4 by setting $\mu^+ = 4 \times 10^{-4}$ Pa·s, $a = 1$ m, $\rho = 1$ kg·m^{-3},and $k = 2 \times 10^{-4}$ s^{-1} The electrical properties are normalized by setting $\sigma^+ = 1$ S·m^{-1}, and $\varepsilon^+ = 1$ F·m^{-1}. With these variables fixed, the remaining parameters are determined through the selection of the dimensionless parameters Ca, Ca_E, σ_r, ε_r, λ, E_b, C_m, and G_m. As in Chapter 4, dimensionless times in this chapter are normalized by the shear rate. The simulations below use the same mesh used in Chapters 4 and 5, which consists of 5120 triangular elements composed of 2562 Lagrangian nodes. As in Chapter 5, the time step was selected using Equation (133). The decreased time step ensures resolution of the membrane charging scale, t_c, which is typically the most restrictive time scale, as can be seen in Table II.

6.1 SPHERICAL CAPSULES

In this section we will look at the deformation parameter, D_{xy}, and the inclination angle, θ, and the effect that Ca, Ca_E, λ, σ_r, ε_r, C_m, G_m, and E_b play in the dynamics. For the capillary number we consider the same range of values considered in the study for spherical capsules in shear flow, with

TABLE II: Dimensionless time scales for a spherical capsule in shear flow with $C_m = 50$, $G_m = 0$ for conductivity ratios, $\sigma_r = 10$ and $\sigma_r = 0.1$.

	kt_f	kt_m	kt_c	kt_e^+	kt_e^-
$\sigma_r = 0.1$	1	Ca	0.105	2×10^{-4}	2×10^{-3}
$\sigma_r = 10$	1	Ca	0.006	2×10^{-4}	2×10^{-5}

Ca ranging from 0.025 to 0.2. For the electric capillary number we consider values ranging from 0.025 to 0.5. Based on these considerations the Mason number, Mn=Ca_E/Ca, ranges from 0.125 to 20. As in the study for simple shear flow, we consider two viscosity ratios, $\lambda = 1$ and $\lambda = 5$, and four dimensionless bending stiffnesses, $E_b = 0$, $E_b = 0.01$, $E_b = 0.025$, and $E_b = 0.0375$. Conductivity ratios of $\sigma_r = 0.1$ and $\sigma_r = 10$ are considered, while the permittivity ratio is fixed at $\varepsilon_r = 1$. Following the study by Das and Thaokar [80], the membrane capacitance is held fixed at $C_m = 50$ and three membrane conductances, $G_m = 0$, $G_m = 1$, and $G_m = 10$, are considered.

As in Chapter 5, the Eulerian domain is a cube spanning of size $[0, 8.0a]^3$. The grid is discretized into a 161^3 grid, which results in a step size of $\Delta x = \Delta y = \Delta z = 0.05a$. A 6 grid W-cycle is used, which results in a resolution of 5^3 on the coarsest grid. As in the previous sections, the MRT relaxation parameters s_4 and s_1 are set according to Equations (44) and (45) respectively. The parameters s_0, s_3, s_5, and s_7 correspond to the conserved moments and are thus set equal to zero. The remaining relaxation parameters are set equal to 1.8.

6.1.1 NON-CONDUCTING CAPSULES WITH MATCHED VISCOSITIES

The first case considered here is the effect of varying the capillary number and electric capillary number for capsules with non-conducting membranes (i.e. $G_m = 0$) and matched viscosities (i.e. $\lambda = 1$). We will look at the deformation and inclination angle of the capsule for varying values of Ca and Ca_E. For a fixed value of Ca_E, increasing Ca is equivalent to decreasing the Mason number, Mn, indicating that the viscous stresses are increased relative to the electric stresses. Conversely, increasing Ca_E for a fixed Ca is equivalent to increasing Mn, indicating increased electrical stresses relative to the viscous stresses.

In Figure 36 the deformation and inclination angle for spherical capsules enclosing a fluid

less conducting than the ambient fluid are plotted for varying values of Ca_E. The dimensionless parameters are fixed at $C_m = 50$, $G_m = 0$, $\sigma_r = 0.1$, $\varepsilon_r = 1$, $\lambda = 1$, $E_b = 0$, and Ca=0.1. In Figure 36b the capsule's equilibrium inclination angle is seen to increase as the electric capillary number increases. This can be understood by considering the results from Chapter 5 where it was shown that, for a non-conducting membrane, the capsule's equilibrium shape was a prolate spheroid with an inclination angle of $\pi/2$ for all values of σ_r. As Ca_E increases the effects of the electric field become more dominant, resulting in an equilibrium angle nearer $\pi/2$. It's also interesting to note the effect that the field has on the initial inclination angle, where increased capillary numbers result in an inclination angle approaching 0. This phenomena is caused by the initially uncharged membrane, which results in compressive forces at the poles. These forces result in oblate deformation that competes with the effects of the shear flow and thus, the inclination angle will approach 0 as Ca_E increases.

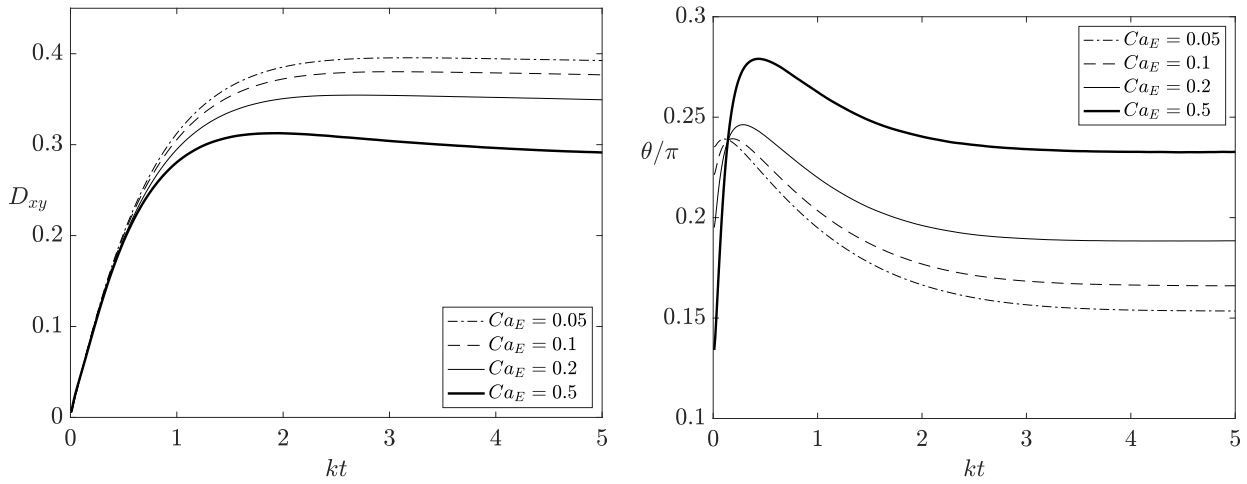

(a) (b)

Fig. 36: (a) Deformation and (b) inclination angle for an initially spherical capsule with Ca=0.1, $E_b = 0$, $\lambda = 1$, $\sigma_r = 0.1$, $\varepsilon_r = 1$, $C_m = 50$, and $G_m = 0$ for varying Ca_E.

In Figure 36a the deformation is seen to decrease as the electric capillary number increases. For a neutral membrane in a shear flow and DC electric field the deformation increases with the electric capillary number [75], and thus these results warrant further attention. Figure 37a shows

the profile of the capsule, the flow streamlines, and the electric forces once the capsule has reached its equilibrium shape for the case where $\mathrm{Ca}_E = 0.1$. As can be seen in the figure, the electric forces acting on the capsule are at their largest at the shoulders of the capsule, where they act in the opposite direction of the flow. These forces are caused by the capacitance of the fully-charged membrane. In the absence of an external flow field these forces cause the capsule to deform to a prolate spheroid as illustrated in Figures 29 and 30 of Chapter 5.

Figure 37b plots the magnitude of the electrical forces at equilibrium, denoted in the plot by f_e, for $\mathrm{Ca}_E = 0.05$, $\mathrm{Ca}_E = 0.1$, and $\mathrm{Ca}_E = 0.2$. The electrical forces are scaled by the viscous forces, μ^+ka^3, which remain fixed since Ca is held constant for $\mathrm{Ca}_E = 0.05$, $\mathrm{Ca}_E = 0.1$, $\mathrm{Ca}_E = 0.2$ in Figure 36. As can be seen in the figure, the forces at the capsule shoulders, which act against the shear-induced deformation, increase as Ca_E increases, and thus, for a fixed value of Ca, the deformation of the capsule will decrease as Ca_E increases as was observed in Figure 36a.

The equilibrium shape for the parameters from Figure 36 are plotted in Figure 38 for $\mathrm{Ca}_E = 0.05$, $\mathrm{Ca}_E = 0.1$, and $\mathrm{Ca}_E = 0.5$. As was shown in Figures 36a and 36b the capsule deformation decreases, while the capsule's inclination angle increases with increasing Ca_E. As will be demonstrated below, the steady shapes are independent of σ_r due to the presence of the fully charged, non-conducting, membrane.

Figure 39 shows the deformation and inclination angle for spheres with $C_m = 50$, $G_m = 0$, $\sigma_r = 10$, $\varepsilon_r = 1$, $\lambda = 1$, $E_b = 0$, and Ca=0.1 for varying values of Ca_E. This case is identical to the case from Figure 36, except for the conductivity ratio, σ_r, as we are now considering the case where capsule fluid is more conducting than the surrounding fluid. In the absence of shear flow these capsule would be expected to exhibit prolate deformation for all times. The effect of this is seen in Figure 39b, where the initial inclination angle is greater than $\pi/4$. The equilibrium deformation and inclination angles are the same as those from Figure 36, demonstrating the independence between the equilibrium configurations and σ_r.

Figure 40 demonstrates the effect of increasing the capillary number on the deformation of an initially spherical neo-Hookean capsule with $\mathrm{Ca}_E = 0.1$, $\lambda = 1$, $\sigma_r = 0.1$, $\varepsilon_r = 1$, $E_b = 0$, $C_m = 50$, and $G_m = 0$. For a shear flow in the absence of an electric field, increased values of Ca result in increased deformation. As is seen in Figure 40a, this pattern holds for capsules in a combined electric field and shear flow. The inclination angle is plotted as a function of time in Figure 40b

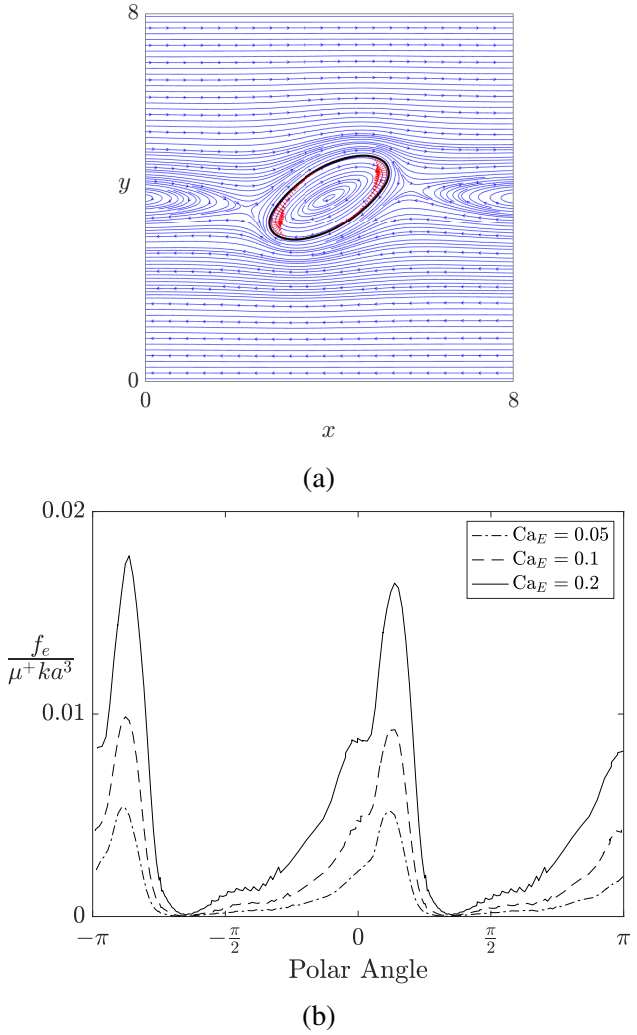

Fig. 37: The effect of the membrane electrical force on the equilibrium shape of an initially spherical capsule. (a) The capsule profile, flow streamlines (blue arrows), and electrical forces (red arrows) of an initially spherical capsule with $\mathrm{Ca}_E = 0.1$ at $kt = 5$. (b) The electrical force as a function of polar angle for an initially spherical capsule for varying values of Ca_E at $kt = 5$. The remaining dimensionless parameters are given by Ca= 0.1, $E_b = 0$, $\lambda = 1$, $\sigma_r = 0.1$, $\varepsilon_r = 1$, $C_m = 50$, and $G_m = 0$.

and, as in the case of simple shear flow, increasing Ca results in a decrease in the inclination angle. The initial inclination angle shows the inverse relationship, with increasing values of Ca resulting in an inclination angle closer to $\pi/4$. This can be understood by observing that since Ca_E is fixed,

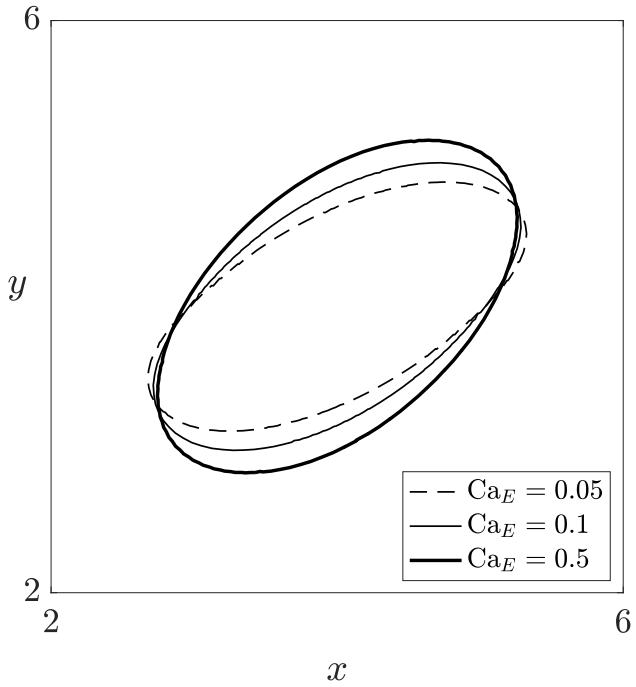

Fig. 38: The equilibrium shape of initially spherical capsules in a combined shear flow and DC electric field for Ca= 0.1, $\lambda = 1$, $E_b = 0$, $\sigma_r = 0.1$, $\varepsilon_r = 1$, $C_m = 50$, and $G_m = 0$.

increasing Ca causes the dynamics of the shear flow to play a greater role in the dynamics, and hence the initial orientation angle will approach $\pi/4$ seen in simple shear flow as Ca increases.

Figure 41 is the same as Figure 40, except that the conductivity ratio is set to $\sigma_r = 10$. In this case, $\sigma_r/\varepsilon_r > 1$ and thus, we would expect prolate deformation in the absence of an external flow. The deformation and inclination angle show the same pattern seen for simple shear flow and for the case when $\sigma_r = 0.1$: increasing Ca results in increased deformation and a capsule aligned more closely with the x-axis. The initial inclination angle also exhibits the same pattern seen in Figure 40b where increasing Ca results in an initial inclination angle closer to $\pi/4$ as would be expected in simple shear flow. As stated above, this indicates the greater role the shear flow plays in the dynamics as Ca increases.

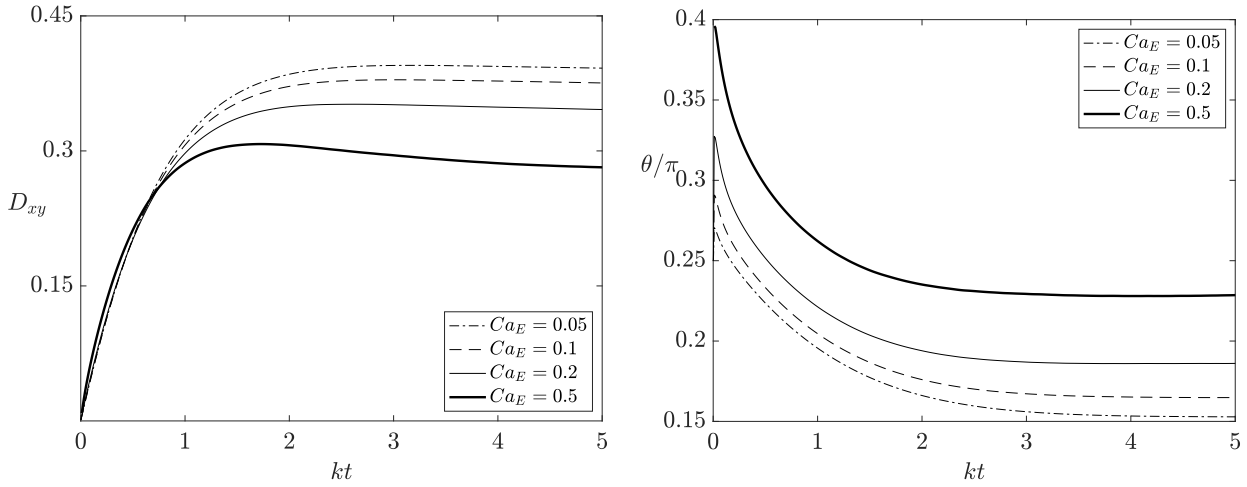

Fig. 39: (a) Deformation and (b) inclination angle for an initially spherical capsule with Ca= 0.1, $E_b = 0$, $\lambda = 1$, $\sigma_r = 10$, $\varepsilon_r = 1$, $C_m = 50$, and $G_m = 0$ for varying Ca_E.

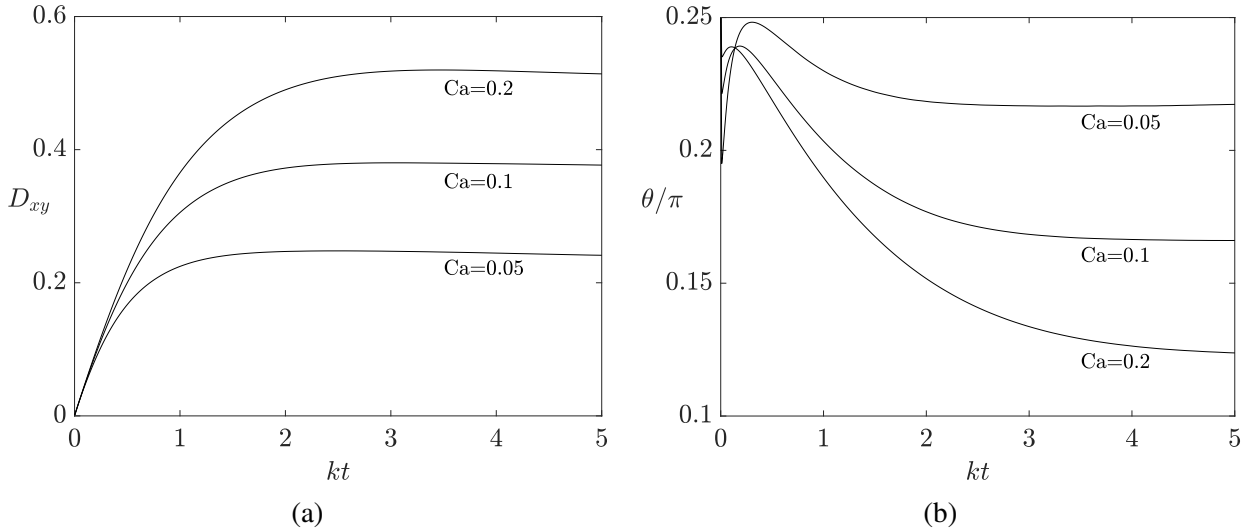

Fig. 40: (a) Deformation and (b) inclination angle for an initially spherical capsule with $\mathrm{Ca}_E = 0.1$, $E_b = 0$, $\lambda = 1$, $\sigma_r = 0.1$, $\varepsilon_r = 1$, $C_m = 50$, and $G_m = 0$ for varying Ca.

6.1.2 NON-CONDUCTING VISCOUS CAPSULES

Next we consider the case of capsules that are more viscous than the surrounding fluid. The increased viscosity of the capsule results in a slower relaxation time for the flow, and thus these

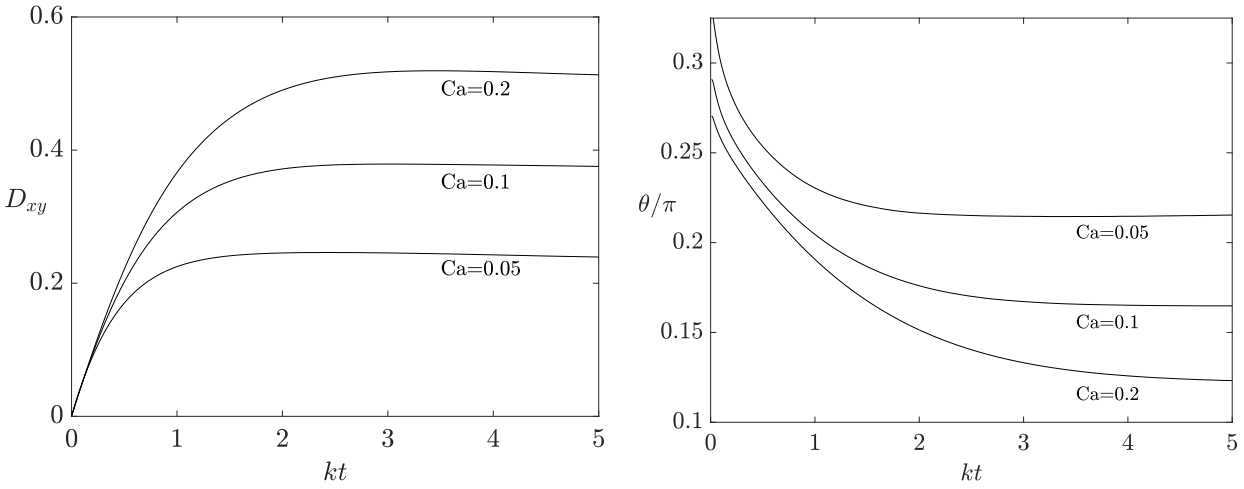

Fig. 41: (a) Deformation and (b) inclination angle for an initially spherical capsule with $\mathrm{Ca}_E = 0.1$, $E_b = 0$, $\lambda = 1$, $\sigma_r = 10$, $\varepsilon_r = 1$, $C_m = 50$, and $G_m = 0$ for varying Ca.

simulations are run until $kt = 15$. In Figure 42 the deformation and inclination angle for a capsule with material ratios $\lambda = 5$, $\sigma_r = 0.1$, and $\varepsilon_r = 1$ are plotted for multiple values of Ca_E. The remaining parameters are fixed at Ca=0.1, $E_b = 0$, $C_m = 50$, and $G_m = 0$. As can be seen in the figure, the deformation exhibits the same pattern noted for non-conducting capsules with $\lambda = 1$, where increasing Ca_E results in reduced deformation and an equilibrium inclination angle nearer the y-axis.

Figure 43b shows the effect of increasing Ca for a capsule with $\lambda = 5$, $\sigma_r = 0.1$, and $\varepsilon_r = 1$. The remaining parameters are held fixed at $\mathrm{Ca}_E = 0.1$, $E_b = 0$, $C_m = 50$, and $G_m = 0$. As in the case of capsules with matched viscosities, increasing Ca results in increased deformation and an inclination angle nearer the x axis at equilibrium. The initial inclination angle also follows the behavior noted for capsules with matched viscosities, where increasing Ca results in an inclination angle closer to $\pi/4$ as would be expected in the absence of an electric field. As mentioned above, this is because for a fixed Ca_E, increasing Ca increases the viscous stresses relative to the electrical stresses, and thus the capsule behavior will approach that of a capsule in simple shear flow.

Figure 44 is the counterpart to Figure 42 for capsules with $\sigma_r = 10$ instead of $\sigma_r = 0.1$, where the effects of varying Ca_E were studied. The remaining parameters are fixed at $\lambda = 1$, $\varepsilon_r = 1$, Ca=0.1, $E_b = 0$, $C_m = 50$, and $G_m = 0$. As in the case of capsules with matched viscosities, the

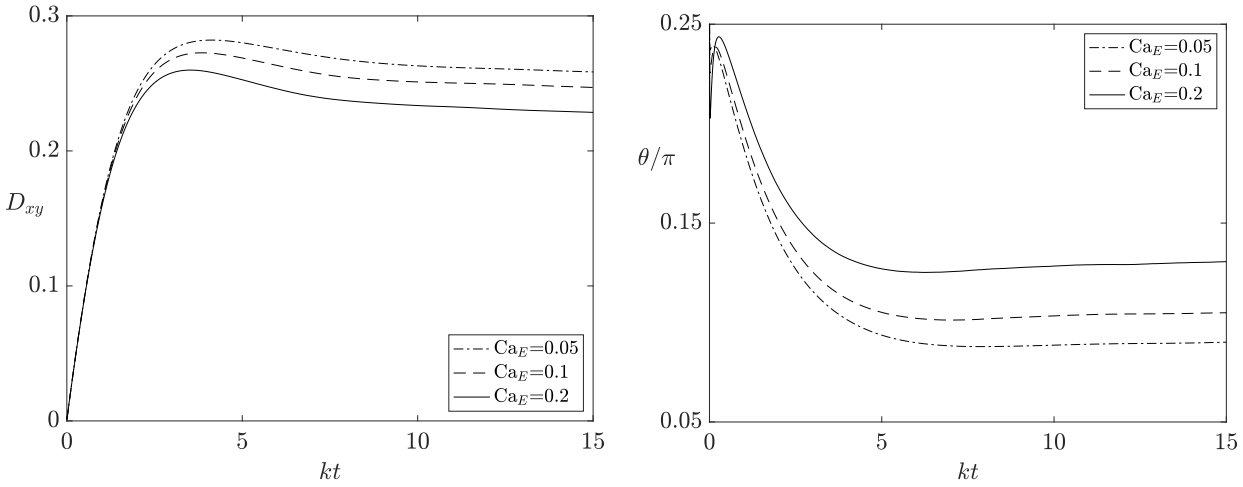

Fig. 42: (a) Deformation and (b) inclination angle for an initially spherical capsule with Ca=0.1, $E_b = 0$, $\lambda = 5$, $\sigma_r = 0.1$, $\varepsilon_r = 1$, $C_m = 50$, and $G_m = 0$ for varying Ca_E.

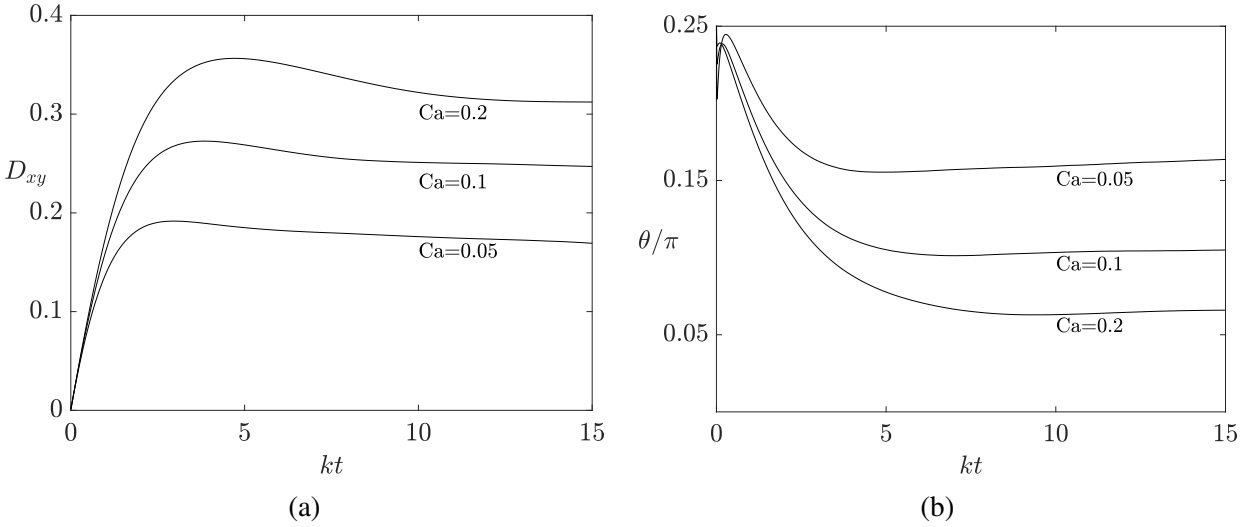

Fig. 43: (a) Deformation and (b) inclination angle for an initially spherical capsule with $\mathrm{Ca}_E = 0.1$, $E_b = 0$, $\lambda = 5$, $\sigma_r = 0.1$, $\varepsilon_r = 1$, $C_m = 50$, and $G_m = 0$ for varying Ca.

equilibrium behavior is identical to that for capsules with $\sigma_r = 0.1$ due to the charging of the membrane, which, for non-conducting membranes, results in equilbirium behavior that is independent of σ_r [80]. The initial inclination angle increases with Ca_E due to the increased electrical stresses which for $\sigma_r = 10$ cause the capsule to exhibit greater alignment with the y axis.

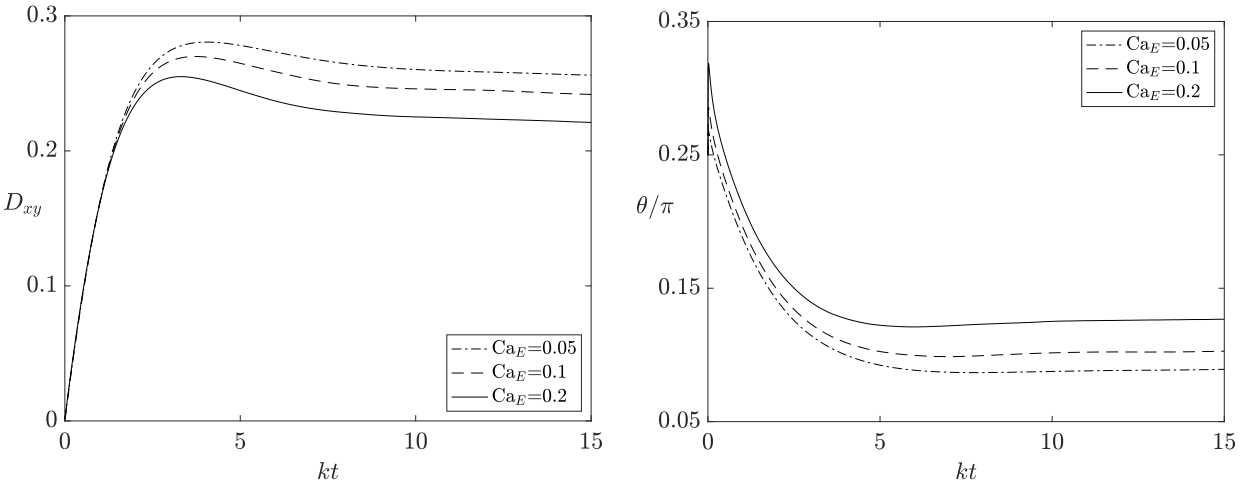

(a) (b)

Fig. 44: (a) Deformation and (b) inclination angle for an initially spherical capsule with Ca=0.1, $E_b = 0$, $\lambda = 5$, $\sigma_r = 10$, $\varepsilon_r = 1$, $C_m = 50$, and $G_m = 0$ for varying Ca_E.

Figure 45 is the counterpart to Figure 43 for capsules with $\sigma_r = 10$ instead of $\sigma_r = 0.1$, where the effects of varying Ca were studied. The remaining parameters are fixed at $\lambda = 1$, $\varepsilon_r = 1$, $\mathrm{Ca}_E = 0.1$, $E_b = 0$, $C_m = 50$, and $G_m = 0$. As noted above, the equilibrium behavior is identical to the case for $\sigma_r = 0.1$. The initial behavior also follows the pattern noted for $\sigma_r = 0.1$, where increasing Ca results in an initial inclination angle closer to $\pi/4$.

6.1.3 CONDUCTING MEMBRANES

Next, we consider the effect of the membrane conductance for capsules under a combined shear flow and DC electric field. Das and Thaokar investigated conducting capsules in a uniform DC electric field in the absence of external flows, finding that the behavior of conducting capsules approaches the behavior of neutral membranes as G_m increases [80]. Physically speaking conducting membranes allow charge to pass from one side of the membrane to the other, and thus increasing the membrane conductance reduces the shielding effects of the membrane capacitance. Based on the observed effects of the membrane capacitance in the previous sections, where increased electric field strengths (indicated by increased values of Ca_E) resulted in less deformation, our primary focus will be on the effect of membrane conductance on the relationship between Ca_E and D_{xy}.

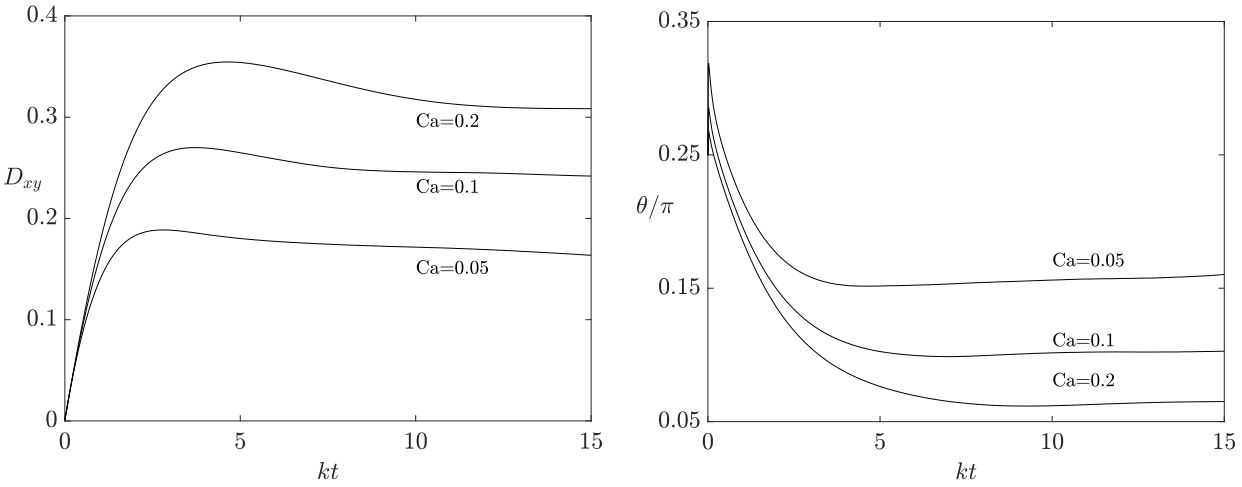

Fig. 45: (a) Deformation and (b) inclination angle for an initially spherical capsule with $\mathrm{Ca}_E = 0.1$, $E_b = 0$, $\lambda = 5$, $\sigma_r = 10$, $\varepsilon_r = 1$, $C_m = 50$, and $G_m = 0$ for varying Ca.

Figure 46 plots the deformation and inclination angle for an initially spherical capsule with a conducting membrane, $G_m = 1$, enclosing a fluid that is less conducting than the ambient fluid for multiple values of Ca_E. The remaining parameters are fixed at Ca=0.1, $E_b = 0$, $\lambda = 1$, $\sigma_r = 0.1$, $\varepsilon_r = 1$, and $C_m = 50$. The deformation parameter is plotted in Figure 46a, where it can be seen that the deformation increases with increasing Ca_E. In Figure 46b an increasing Ca_E is seen to decrease the inclination angle, indicating that the capsule's equilibrium inclination angle moves towards the x axis. This behavior matches the small deformation theory of Ha and Yang for neutral membranes with $\sigma_r < 1$ [75], suggesting that membrane conductance dampens the effects of the membrane capacitance on the steady state.

Figure 47 presents the deformation and inclination angle for an initially spherical capsule with a conducting membrane, $G_m = 1$, and a conductivity ratio of $\sigma_r = 10$, for multiple values of Ca_E. The remaining parameters are fixed at Ca=0.1, $E_b = 0$, $\lambda = 1$, $\varepsilon_r = 1$, and $C_m = 50$. As can be seen in the Figure an increase in the electric field strength results in less deformation and an inclination angle nearer the y axis. This behavior matches the results from simulations of capsules with non-conducting membranes (e.g. Figure 41) rather than the results reported by Ha and Yang for neutral membranes [75]. This suggests that a membrane conductance of $G_m = 1$ is not sufficient to recover the behavior of neutral membranes for capsules with $\sigma_r = 10$.

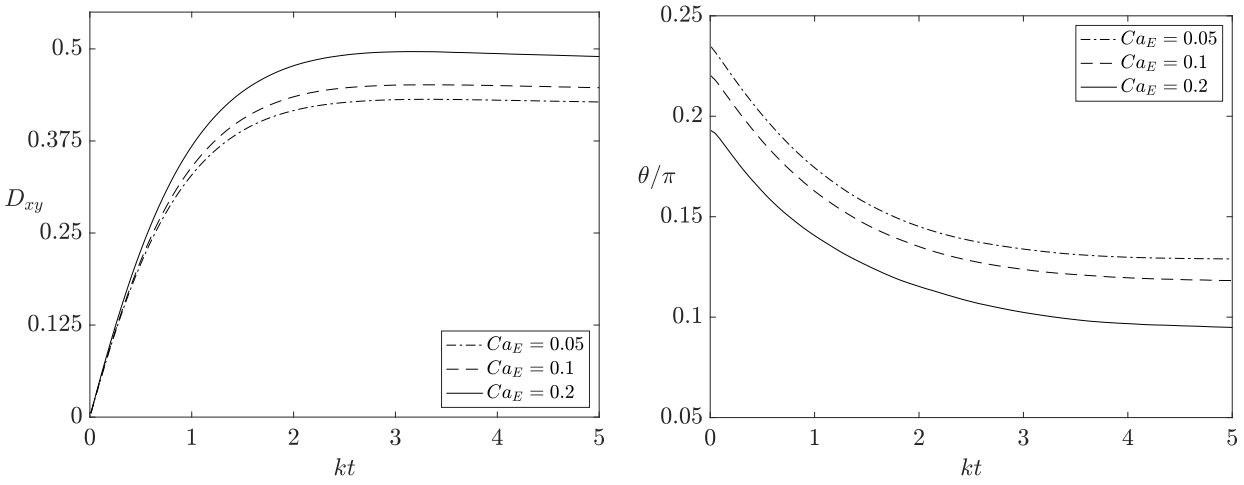

(a) (b)

Fig. 46: (a) Deformation and (b) inclination angle for an initially spherical capsule with Ca= 0.1, $E_b = 0$, $\lambda = 1$, $\sigma_r = 0.1$, $\varepsilon_r = 1$, $C_m = 50$, and $G_m = 1$ for varying Ca_E.

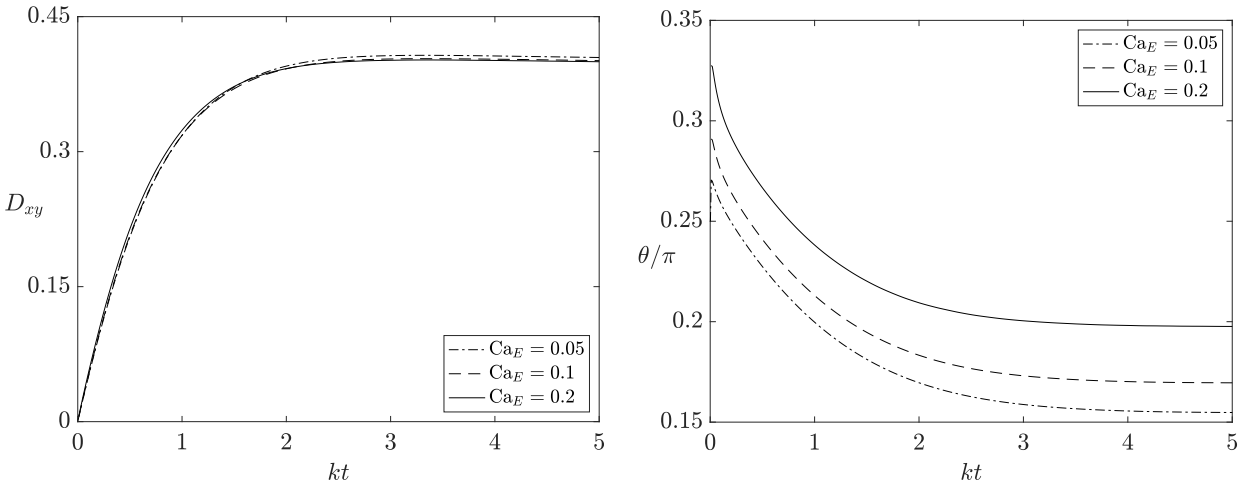

(a) (b)

Fig. 47: (a) Deformation and (b) inclination angle for an initially spherical capsule with Ca= 0.1, $E_b = 0$, $\lambda = 1$, $\sigma_r = 10$, $\varepsilon_r = 1$, $C_m = 50$, and $G_m = 1$ for varying Ca_E.

Next we increase the membrane conductivity to $G_m = 10$ while keeping the membrane capacitance fixed at $C_m = 50$. As before, we consider capsules with conductivity ratios $\sigma_r = 10$ and $\sigma_r = 0.1$ for $\mathrm{Ca}_E = 0.05$, 0.1, and 0.2. As in the simulations with $G_m = 1$ the remaining parameters are fixed at Ca=0.1, $E_b = 0$, $\lambda = 1$, $\varepsilon_r = 1$, and $C_m = 50$. In Figure 48 the deformation and

inclination angle are plotted for the case with $\sigma_r = 0.1$. For $\mathrm{Ca}_E = 0.2$ numerical capsule burst occurrs and thus, the results for $\mathrm{Ca}_E = 0.2$ are not pictured. For $\mathrm{Ca}_E = 0.05$ and $\mathrm{Ca}_E = 0.1$ the same trends seen for $G_m = 1$ are observed where stronger fields result in greater deformation and a capsule oriented nearer the x axis. When compared with the case for $G_m = 1$, greater deformation and an inclination angle nearer the x axis occur for a given value of Ca_E.

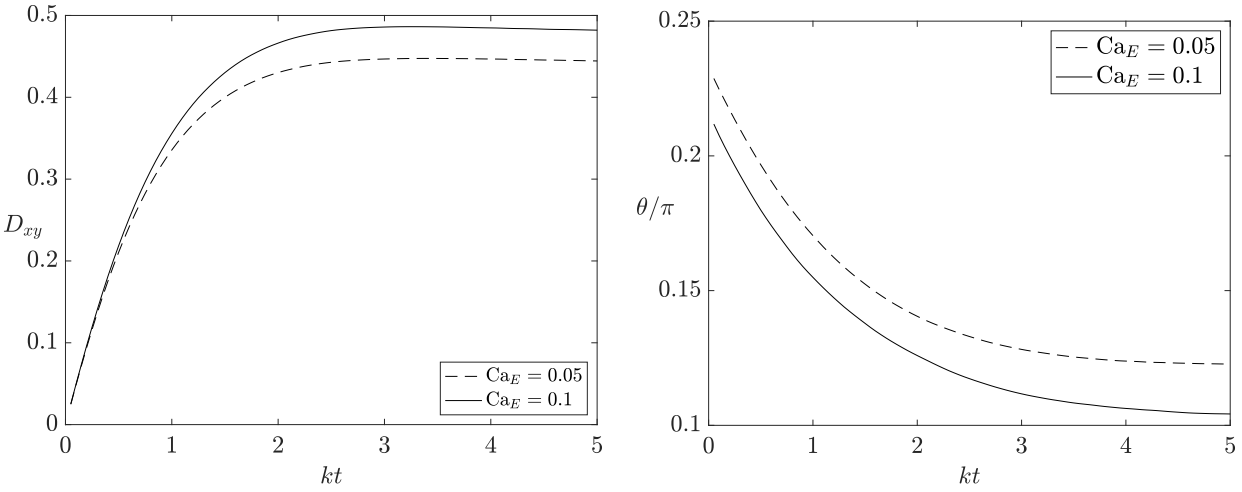

Fig. 48: (a) Deformation and (b) inclination angle for an initially spherical capsule with Ca=0.1, $E_b = 0$, $\lambda = 1$, $\sigma_r = 0.1$, $\varepsilon_r = 1$, $C_m = 50$, and $G_m = 10$ for varying Ca_E.

Figure 49 depicts the deformation and inclination angle for a capsule with $G_m = 10$ and $\sigma_r = 10$. The remaining parameters are the same as in Figure 48. As can be seen in the Figure 49a, for $G_m = 10$, increasing Ca_E results in greater deformation, matching the expected behavior of a neutral membrane. The inclination angle is depicted in Figure 49b, where it can be seen that increasing the electric field strength results in a capsule more closely aligned with the y axis.

The difference in behavior between capsules with $\sigma_r = 0.1$ and $\sigma_r = 10$ for membrane conductance $G_m = 1$ can be understood by considering the effect of σ_r and G_m on the transmembrane potential. A qualitative estimate of the transmembrane potential can be obtained by considering the analytical expression for the transmembrane potential of a sphere in a DC electric field, given

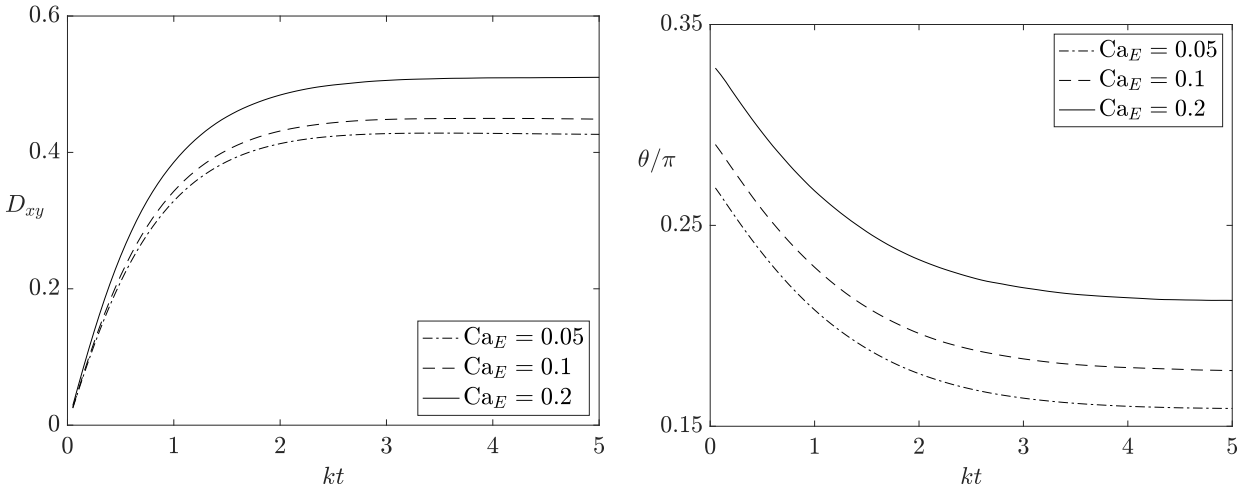

(a) (b)

Fig. 49: (a) Deformation and (b) inclination angle for an initially spherical capsule with Ca=0.1, $E_b = 0$, $\lambda = 1$, $\sigma_r = 10$, $\varepsilon_r = 1$, $C_m = 50$, and $G_m = 10$ for varying Ca_E.

by [62]:

$$V_m(\theta,t) = -aE_0\bar{V}(t)\cos\theta \tag{145}$$

where the magnitude, $\bar{V}$ is a time-dependent function given by:

$$\bar{V}(t) = \frac{3}{2\left[1+G_m\left(\frac{1}{2}+\frac{2}{\sigma_r}\right)\right]}\left[1-\exp\left(-\frac{t}{t_c}\right)\right]. \tag{146}$$

The equilibrium behavior is determined by the transmembrane potential of the capsule when it is fully-charged, computed by taking the limit of $\bar{V}$ as $t \to \infty$.

Before considering the case when $G_m = 1$ it is instructive to consider the limiting cases of $G_m = 0$ and $G_m \gg 1$. For a non-conducting membrane we have $G_m = 0$ giving us $\bar{V} = 1.5$ for a fully-charged capsule. This case was studied in Section 6.1.1 where it was shown that, under the combined effects of shear flow and a DC electric field, deformation of the capsule will decrease as Ca_E increases. For a highly conducting membrane we have $G_m \gg 1$ giving us $\bar{V} \approx 0$ for a fully-charged capsule. Neutral capsules also have $\bar{V} = 0$, suggesting that capsules with $G_m \gg 1$ will behave similar to a neutral capsule. Numerical studies by Das and Thaokar in [80] lend further credence to this reasoning, as they found that for $G_m = 100$ capsules with $\sigma_r = 0.1$ and $\sigma_r = 10$

behaved similar to neutral capsules. Neutral membranes under a combined shear flow and DC electric field were studied by Ha and Yang in [75] where it was shown that increasing Ca_E resulted in increased deformation. Thus we would expect that for $\bar{V} \approx 0$ capsule deformation will increase as Ca_E increases, while for $\bar{V} \approx 1$, the capsule will behave as a non-conducting membrane.

Inserting $G_m = 1$ and $\sigma_r = 0.1$ into Equation (146), we find that the transmembrane potential of a fully-charged spherical membrane is $V \approx 0.07$ and thus the behavior of the capsule is expected to be similar to that of a highly-conducting or neutral membrane. This reasoning is supported by the results from Figure 46 where it is seen that capsules with $G_m = 1$ and $\sigma_r = 0.1$ behave as neutral capsules, with deformation increasing as Ca_E is increased. Conversely, inserting $G_m = 1$ and $\sigma_r = 10$ into Equation (146) we have $V \approx 1.07$ and thus, based on the discussion above, the behavior of the capsule is expected to be similar to that of a non-conducting membrane. This matches the results from Figure 47 where the deformation decreases as Ca_E is increased as was observed for non-conducting capsules in Section 6.1.1.

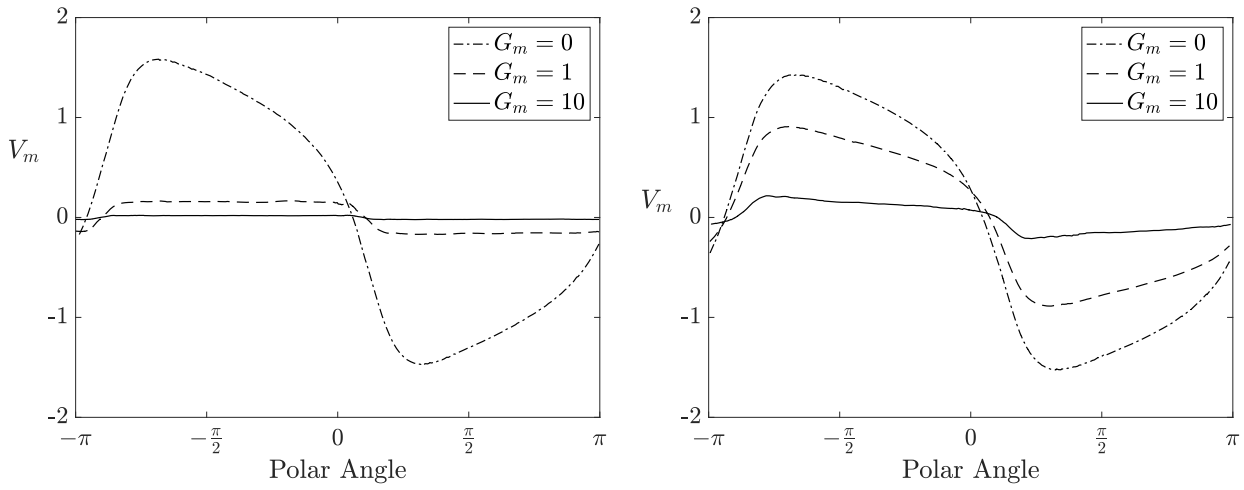

(a) $\sigma_r = 0.1$ (b) $\sigma_r = 10$

Fig. 50: The equilibrium transmembrane potential as a function of polar angle for various membrane conductivities. (a) The equilibrium transmembrane potential for an initially spherical capsule with $\sigma_r = 0.1$. (b) The equilibrium transmembrane potential for an initially spherical capsule with $\sigma_r = 10$. The remaining parameters are fixed at Ca$= 0.1$, $\mathrm{Ca}_E = 0.1$, $E_b = 0$, $\lambda = 1$, $\varepsilon_r = 1$, and $C_m = 50$.

The analytical estimate of Equation (145) qualitatively explains the divergent behavior for capsules with $\sigma_r = 0.1$ and $\sigma_r = 10$, however the capsules in Figures 46 and 47 are spheroidal and are inclined between the x and y axis, and thus we present the numerical values of the transmembrane potential in order to assess the degree to which the analysis above holds. Figure 50 depicts the transmembrane potential in the plane of shear at steady state for $G_m = 0$, 1, and 10 for capsules with $\sigma_r = 0.1$ and $\sigma_r = 10$. For $G_m = 0$ the transmembrane potentials are the same for $\sigma_r = 0.1$ and $\sigma_r = 10$, as predicted by Equation (145). For $G_m = 1$, the transmembrane potential for capsules with $\sigma_r = 0.1$ is on the order of 0.2, whereas for capsules with $\sigma_r = 10$ the transmembrane potential is on the order of 1. This also agrees with the analysis above, suggesting that for $G_m = 1$ the transmembrane potential plays a larger role in the dynamics of capsules with $\sigma_r = 10$. For $G_m = 10$, we see that $V_m \ll 1$ for capsules with $\sigma_r = 0.1$ and capsules with $\sigma_r = 10$ and thus, we expect these capsule to behave as neutral capsules for both $\sigma_r = 0.1$ and $\sigma_r = 10$ as demonstrated in Figures 48 and 49.

In order to further study the effects of the transmembrane potential on the electric field inside the capsule we consider the profile of the electric field and potential in the plane of shear. For non-conducting capsules ($G_m = 0$) the electric potential and electric field at steady state are independent of the conductivity ratio since the interior fluid is fully shielded from the electric field. Thus, we only plot the electric field for the case when $\sigma_r = 0.1$ since the two plots are identical. The electric potential and electric field lines at the z centerline in the plane of shear for a capsule at equilibrium are depicted in Figure 51 for a capsule with Ca$= 0.1$, $\mathrm{Ca}_E = 0.1$, $\lambda = 1$, $E_b = 0$, $\sigma_r = 0.1$, $\varepsilon_r = 1$, and $C_m = 50$. As can be seen in the figure, the electric potential is approximately constant inside the capsule, and thus the electric field in the interior is nearly zero.

Figure 52 depicts the fields lines for capsules with membrane conductivity $G_m = 1$. In Figure 52a the electric potential and electric field lines at the z centerline in the plane of shear for a capsule at equilibrium are depicted for a capsule with $\sigma_r = 0.1$. The electric potential now exhibits a gradient, ranging from approximately $-3aE_0$ to $-5aE_0$ inside the capsule. In Figure 52b the electric potential and electric field lines for at the z centerline in the plane of shear for a capsule at equilibrium are depicted for a capsules with $\sigma_r = 10$. As in the case of a non-conducting membrane the electric potential inside the capsule is nearly constant, further supporting the notion that for $\sigma_r = 10$, a larger membrane conductivity is required to overcome the membrane capacitance.

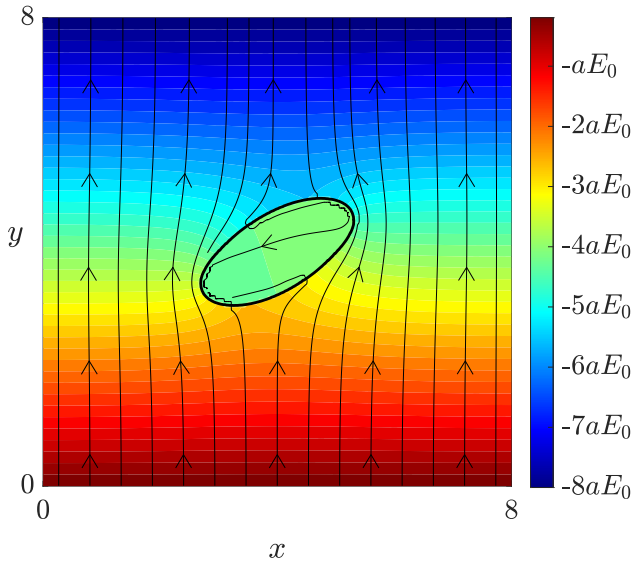

Fig. 51: A heat map of the steady-state electric potential and the electric field lines in the $x-y$ plane for Ca= 0.1, $\mathrm{Ca}_E = 0.1$, $\varepsilon_r = 1$, $\lambda = 1$, $C_m = 50$, and $G_m = 0$.

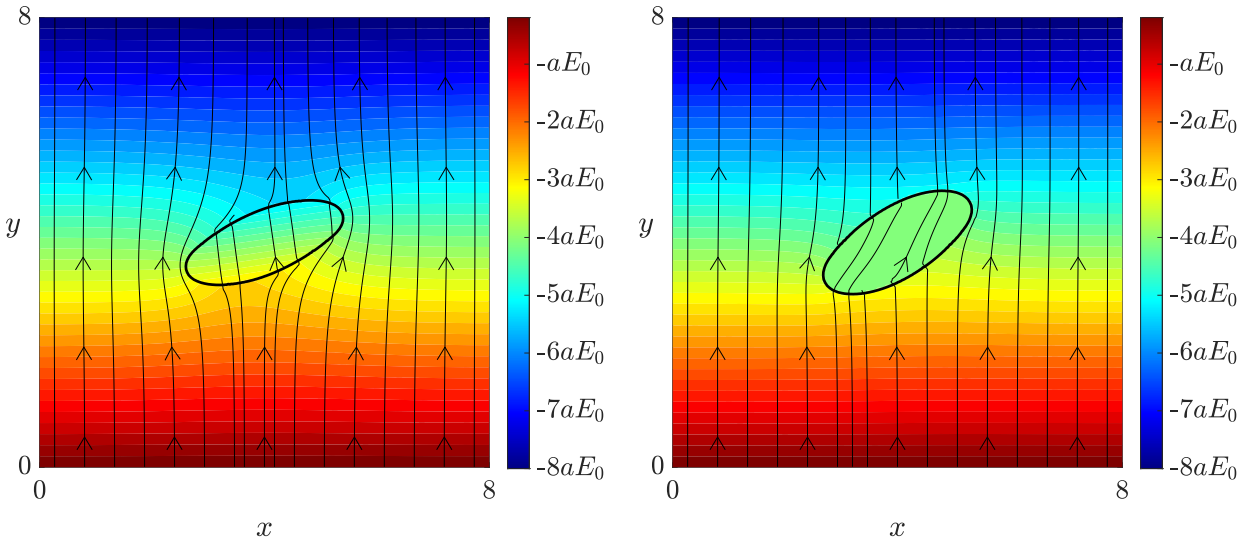

(a) $\sigma_r = 0.1$ (b) $\sigma_r = 10$

Fig. 52: A heat map of the steady-state electric potential and the electric field lines in the $x-y$ plane for Ca=0.1, $\mathrm{Ca}_E = 0.1$, $\varepsilon_r = 1$, $\lambda = 1$, $C_m = 50$, and $G_m = 1$.

Figure 53 depicts the fields lines for capsules with membrane conductivity $G_m = 10$. In Figure 53a the electric potential and electric field lines for at the z centerline in the plane of shear for a

capsule at equilibrium are depicted for a capsules with $\sigma_r = 0.1$. As in Figure 52a the electric potential in the interior of the capsule exhibits a gradient, with the electric potential ranging from $-5.5aE_0$ to $-2.5aE_0$, indicating a stronger electric field inside the capsule. In Figure 53b the high conductance of the interior fluid for capsules with $\sigma_r = 10$ is seen to affect the electric field outside the capsule, as the field lines pass directly through the capsule.

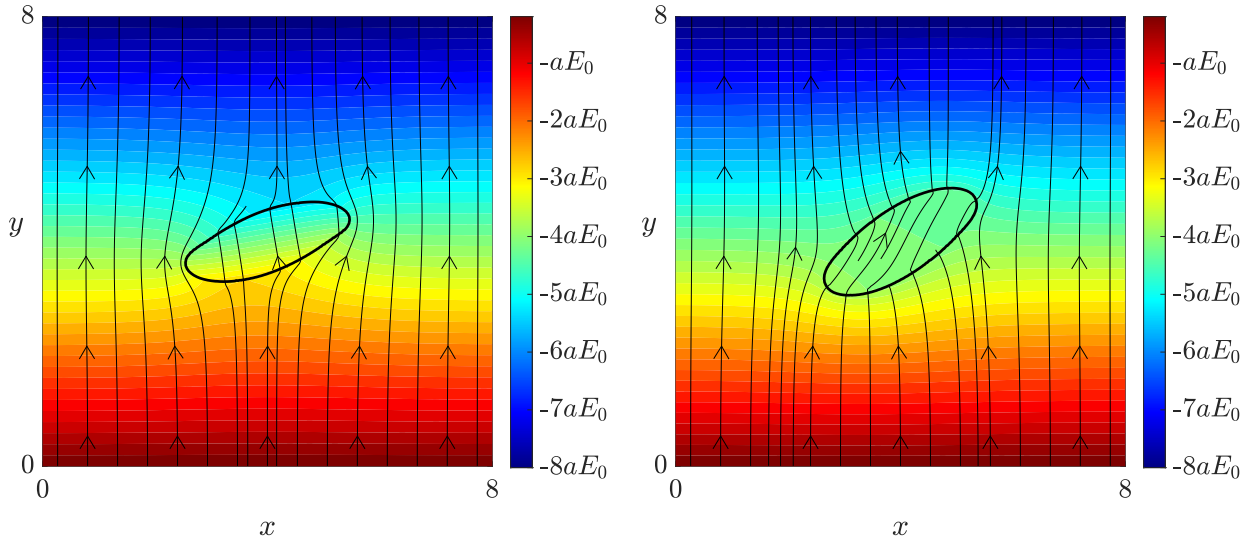

(a) $\sigma_r = 0.1$ (b) $\sigma_r = 10$

Fig. 53: A heat map of the steady-state electric potential and the electric field lines in the $x-y$ plane for Ca=0.1, $\mathrm{Ca}_E = 0.1$, $\varepsilon_r = 1$, $\lambda = 1$, $C_m = 50$, and $G_m = 10$.

6.1.4 THE EFFECTS OF CAPSULE BENDING STIFFNESS

For initially spherical capsules, the capsule's bending stiffness exerts compressive forces on the capsule membrane. In shear flow these forces result in reduced deformation and an inclination angle nearer $\pi/4$ for a given value of Ca [41, 46]. In this section we consider the effect of bending stiffness for initially spherical capsules in a combined electric field and shear flow.

In Figure 54 the deformation and inclination angle for various values of the bending stiffness,

E_b, are presented for a spherical capsule with conductivity ratio $\sigma_r = 0.1$. The remaining parameters are fixed at Ca=0.1, $\mathrm{Ca}_E = 0.1$, $\lambda = 1$, $\varepsilon_r = 1$, $C_m = 50$, and $G_m = 0$. In Figure 54a the deformation is seen to decrease as the capsule's bending stiffness increases as was reported for capsules in shear flow [41, 46]. The inclination angle, presented in Figure 54b, is shown to exhibit similar behavior to that seen in simple shear flow, where increased bending stiffness results in an equilibrium angle further from the x axis.

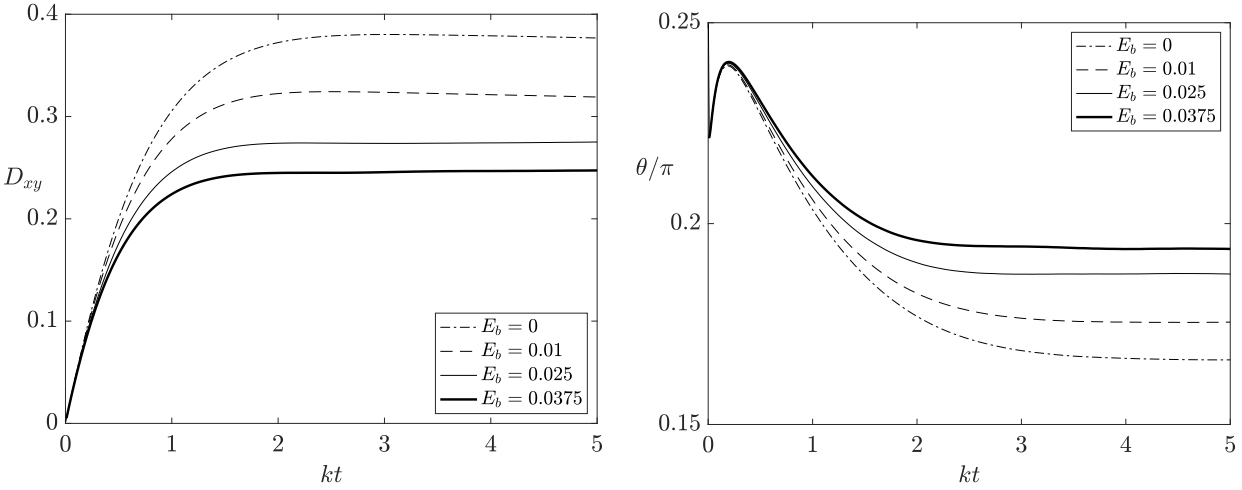

(a) (b)

Fig. 54: (a) Deformation and (b) inclination angle for an initially spherical capsule with Ca=0.1, $E_b = 0$, $\lambda = 5$, $\sigma_r = 0.1$, $\varepsilon_r = 1$, $C_m = 50$, and $G_m = 1$ for varying values of E_b.

Figure 55 shows the deformation and inclination angle of an initially spherical capsule with conductivity ratio $\sigma_r = 10$ for various values of the bending stiffness, E_b. As in Figure 54, the remaining parameters are fixed at Ca= 0.1, $\mathrm{Ca}_E = 0.1$, $\lambda = 1$, $\varepsilon_r = 1$, $C_m = 50$, and $G_m = 0$. The deformation, shown in Figure 55a, and the inclination angle, shown in Figure 55b, exhibit the same behavior seen in simple shear flow, with increased bending stiffness resulting in less deformation and an inclination angle farther from the x axis. It also should be noted that the equilibrium behavior is independent of $\sigma_r = 0.1$ and $\sigma_r = 10$, with both reaching the same equilibrium angles and steady shapes.

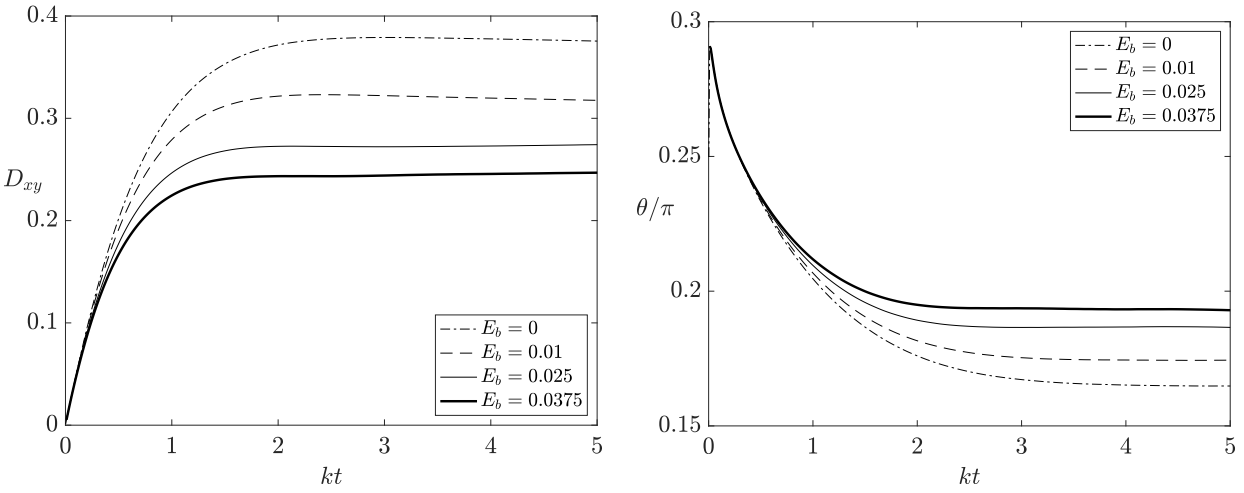

(a) (b)

Fig. 55: (a) Deformation and (b) inclination angle for a capsule with Ca= 0.1, Ca$_E$=0.1, $\lambda = 5$, $\sigma_r = 10$, $\varepsilon_r = 1$, $C_m = 50$, and $G_m = 0$ for varying values of E_b.

6.2 BICONCAVE CAPSULES

The dynamics of biconcave capsules in shear flow was studied in Chapter 4, where it was shown that the motion can be grouped into tank-treading and tumbling motions, with tank-treading occurring at high shear rates or low viscosity ratios and tumbling occurring at low shear rates or high viscosity ratios. To the best of the present authors' knowledge no numerical simulations of red blood cells under a combined shear flow and DC electric field have been conducted. Spheroidal vesicles in a combined shear flow and DC electric have been studied numerically by a number of authors [67, 72, 74]. In these studies it was reported that the electric field dampened the tumbling motion, with strong fields causing the capsules to transition from tumbling to tank-treading motion. Given the similarity between the dynamics of spheroidal capsules and biconcave capsules in simple shear flow, it's expected that biconcave capsules will exhibit similar behavior.

For the simulations in this section we consider two cases: one case for $\sigma_r/\varepsilon_r > 1$ and one case for $\sigma_r/\varepsilon_r < 1$. In [82] red blood cells *in vivo* are reported to have electrical properties given by $\sigma_r = 1.054$, $G_m \approx 0$, $C_m = 282$, and $\varepsilon_r = 0.6$. In this work we choose $\varepsilon_r = 0.6$, $G_m = 0$ and $C_m = 250$, however we choose a slightly larger conductivity ratio of $\sigma_r = 1.5$ due to numerical stiffness in the integration of Equation (73) for capsules with $\sigma_r \approx 1$ using the scheme proposed by [74].

For $\varepsilon_r = 0.6$, both $\sigma_r = 1.054$ and $\sigma_r = 1.5$ result in $\sigma_r/\varepsilon_r > 1$ and thus, their behavior is expected to be qualitatively similar. Furthermore, given that, for capsules with $G_m = 0$, the behavior of spherical capsules was shown to be independent of σ_r after the charging of the membrane, we expect the choice of a larger σ_r to be negligible for $kt \gg \tilde{t}_c$. The second case considered here is for membranes with $\sigma_r/\varepsilon_r < 1$, where we choose $\sigma_r = 0.1$, $\varepsilon_r = 1$, $G_m = 0$, and $G_m = 50$ so that the dynamics of biconcave capsules can be contrasted with the results for spherical capsules discussed in Section 6.1.

As in the previous simulations, we use a mesh consisting of 5120 triangular elements composed of 2562 Lagrangian nodes. As in Chapter 4, the Skalak constitutive law is used with $C = 5$. The capsule is placed in the center of the fluid domain with an ambient shear flow. The initial shape of the biconcave capsule given by Equation (136) has a maximum radius of $1.6a$, as opposed to the initial radius of a for spherical capsules, and thus we increase the domain size to $[0, 10.0a]$ in x, y and z to prevent wall effects. The Eulerian grid is discretized into a 161^3 grid, which results in a step size of $\Delta x = \Delta y = \Delta z = 0.0625a$.

6.2.1 TUMBLING CAPSULES IN AN ELECTRIC FIELD

First, we consider the effects of the electric field on capsules which exhibit tumbling motion in shear flow in the absence of an electric field. For the case where $\sigma_r/\varepsilon_r < 1$ we consider biconcave capsules with $\lambda = 4$ and $E_b = 0.015$ in a shear flow with Ca=0.25. In Chapter 4, in the absence of an electric field, capsules with these parameters were shown to exhibit the tumbling motion (see Figure 20). In Figure 56a the inclination angle of a capsule with $\sigma_r = 0.1$, $\varepsilon_r = 1$, $G_m = 0$, and $C_m = 50$ is shown for $\mathrm{Ca}_E = 0$, 0.1, 0.2, and 0.5. For $\mathrm{Ca}_E = 0.1$ (Mn=0.4), the capsule initially undergoes a half rotation in the tumbling motion before transitioning to the tank-treading mode. This behavior agrees qualitatively with the spheroidal simulations by McConnell et al. in [67], where vesicles were shown to exhibit a half rotation before entering the tank-treading mode. At $\mathrm{Ca}_E = 0.2$ (Mn=0.8) the capsule exhibits a large swinging motion before reaching a relatively constant inclination angle in the tank-treading regime. At $\mathrm{Ca}_E = 0.5$ (Mn=2) the tumbling motion is fully suppressed, with the capsule exhibiting the tank-treading motion throughout the simulation. These results demonstrate the electric field's ability to suppress the tumbling motion of capsules in shear flow.

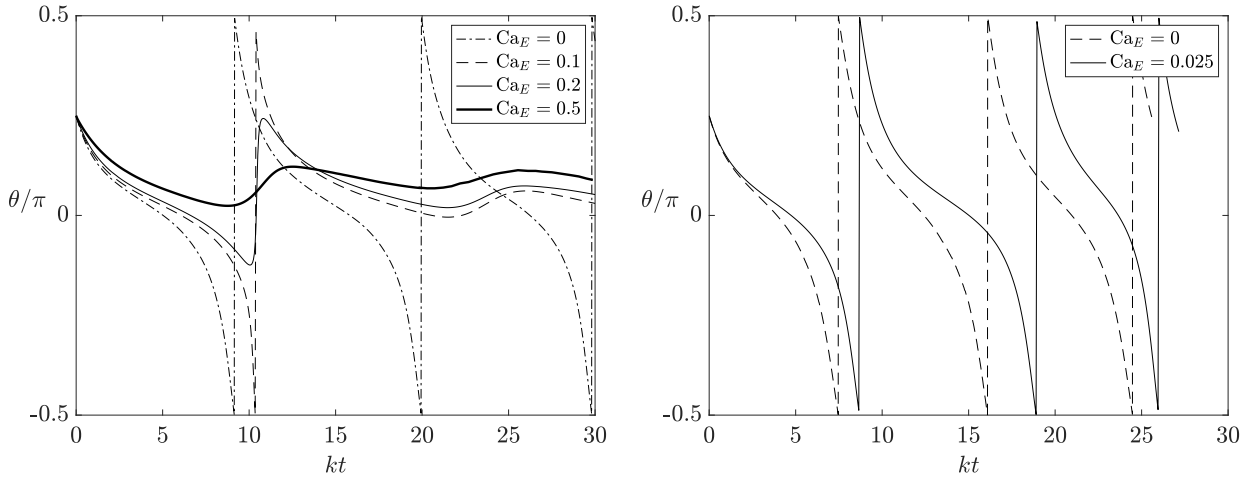

(a) (b)

Fig. 56: The inclination angle of tumbling biconcave capsules in a combined shear flow and DC electric field. (a) Simulations for capsules with Ca=0.25, $\lambda = 4$, $\sigma_r = 0.1$, $\varepsilon_r = 1$, $E_b = 0.015$, $C_m = 50$, and $G_m = 0$ for varying field strengths, Ca_E. (b) Simulations for capsules with Ca=0.1, $\lambda = 4$, $E_b = 0.015$, $\sigma_r = 1.5$, $\varepsilon_r = 0.6$, $C_m = 250$, and $G_m = 0$.

Next, we consider the effects of a weak electric field on a capsule with $\sigma_r/\varepsilon_r > 1$. For spheroidal vesicles in weak electric fields, the electric field was shown to decrease the tumbling frequency [74]. We select $\sigma_r = 1.5$, $\varepsilon_r = 0.6$, $C_m = 250$, and $G_m = 0$ in order to approximate the physiological parameters of a red blood cell, as discussed above. The shear flow strength is given by Ca=0.1 and the capsule has viscosity ratio $\lambda = 4$ and bending stiffness $E_b = 0.015$. The electric field strength is given by $\mathrm{Ca}_E = 0.25$ (Mn= 0.25). The inclination angle for capsules with and without the electric field is plotted in Figure 56b. As expected, in the weak electric field the capsule remains in the tumbling mode, however the electric field results in a decreased tumbling frequency due to the opposing forces of the electric field.

Figure 57 plots the capsule profile, electric potential, and electric field at the z-coordinate centerline. In Figure 57a the initial position and electric field of the capsule are shown. At $kt = 0$ the membrane is uncharged and thus the electric field lines pass through the capsule fluid. In Figures 57b-57c the effect of the membrane capacitance can be observed as the interior fluid has an approximately constant potential. In Figure 57c-57j the capsule is seen to complete a full rotation in the tumbling mode.

6.2.2 THE EFFECT OF THE ELECTRIC FIELD ON TANK-TREADING CAPSULES

Next, we consider the effect of the electric field on capsules in the tank-treading mode. For spheroidal vesicles, Hu et al. reported that the electric field will increase the inclination angle of vesicles in shear flow [74]. These findings agree with the findings from Section 6.1 for spherical capsules in shear flow. We consider the case from Section 6.2.1 for a capsule with $\sigma_r/\varepsilon_r < 1$, giving us $\sigma_r = 0.1$, $\varepsilon_r = 1$, $C_m = 50$, and $G_m = 0$. For this case, we consider a capsule with matched viscosity $\lambda = 1$ in a shear flow given by Ca=0.1, which as can be seen in Figure 21, is the smallest value of Ca for which capsules with $\lambda = 1$ will exhibit tank-treading behavior.

The inclination angle is plotted in Figure 58 for $\mathrm{Ca}_E = 0$, 0.1, and 0.2. In the absence of an electric field the capsule exhibits oscillations with minimum and maximum inclination angles of approximately 0 and $\pi/10$ respectively. For $\mathrm{Ca}_E = 0.1$ and 0.2 the amplitude of the oscillations decreases and the inclination angle increases. As can be seen from the figure, increasing the field strength results in a capsule with increased inclination angle. This agrees with the results for spheroidal vesicles from [74] and the numerical simulations for spherical capsules in Section 6.1.

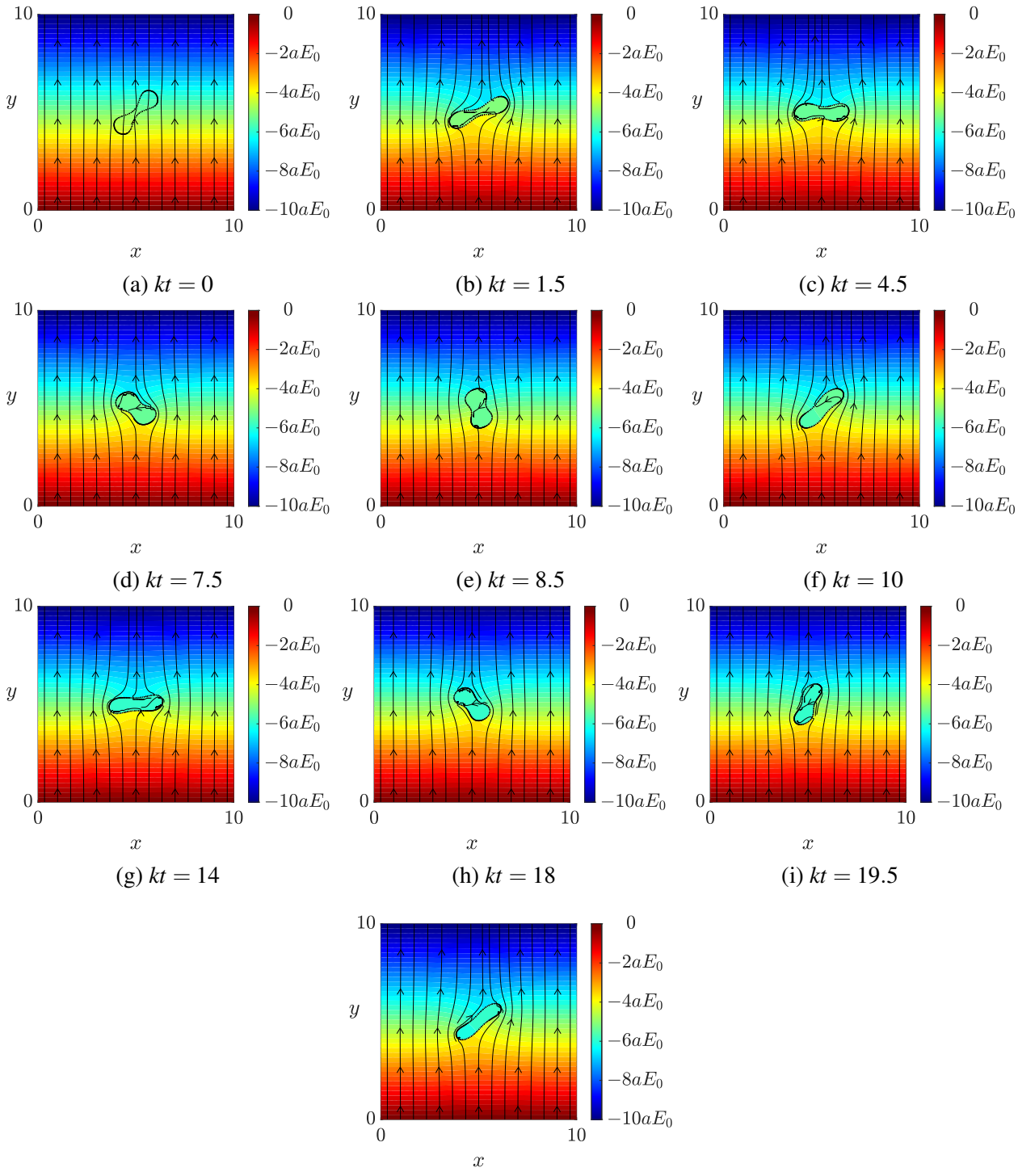

(a) $kt = 0$ (b) $kt = 1.5$ (c) $kt = 4.5$

(d) $kt = 7.5$ (e) $kt = 8.5$ (f) $kt = 10$

(g) $kt = 14$ (h) $kt = 18$ (i) $kt = 19.5$

(j) $kt = 20.5$

Fig. 57: The capsule profile, electric potential, and electric field for an initially biconcave capsule with $\mathrm{Ca}_E = 0.025$, Ca=0.1, $\sigma_r = 1.5$, $\varepsilon_r = 0.6$, $\lambda = 4$, $E_b = 0.025$, $C_m = 250$, and $G_m = 0$ at various times.

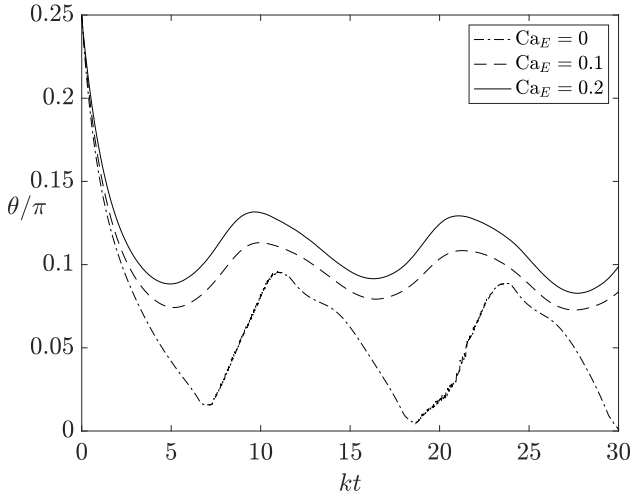

Fig. 58: The inclination angle of tank-treading biconcave capsules in a combined shear flow and DC electric field. The dimensionless parameters are given by Ca=0.1, $\lambda = 1$, $E_b = 0.015$, $\sigma_r = 0.1$, $\varepsilon_r = 1$, $C_m = 50$, and $G_m = 0$ for varying field strengths.

CHAPTER 7

CONCLUSION

In this work a quasi-steady, dual time-stepping (DTS) lattice Boltzmann method (LBM) was presented for flow-induced capsule deformation simulations using the immersed boundary method (IBM). In the proposed DTS scheme we assume the flow is quasi-steady, allowing us to separate the LBM time step from the physical time step. Next, a framework for combining the dual time-stepping LBM-IBM capsule algorithm with the immersed interface method (IIM) was proposed for simulations of electrohydrodynamic capsule deformation. The method is then used to study the dynamics of elastic capsules under the combined effects of shear flow and a DC electric field.

In Chapter 4 the DTS capsule model was validated through numerical simulations of capsules in shear flow over a wide range of dimensionless parameters and various capsule geometries. The efficiency of the newly proposed scheme is then studied through comparison of the CPU time for the proposed algorithm to the CPU time of the standard LBM-IBM capsule deformation algorithm. Our results suggest that for efficient application of the DTS scheme the physical time step should be several orders of magnitude larger than the traditional LBM time step in order to defray the additional computational cost per time step of the multigrid LBM. For simulations of shear-induced deformation we find that the DTS scheme is twice as fast as the standard LBM scheme when a physical time step 100 times larger than the LBM time step is used. Larger differences between the two time steps increase the speed-up of the DTS scheme proportionally. For the parameter regime in which standard LBM-IBM models of capsule deformation are most computationally expensive, the DTS scheme presented in this work results in speed-up on the order of 20. Even for parameter regimes in which increasing the physical time step is limited by the separation of scales we find speed-up on the order of 4-10 times the standard LBM-IBM capsule model.

In Chapter 5, the coupled immersed boundary-immersed interface scheme is validated through numerical simulations of capsules in an initially stationary fluid under the application of a DC electric field. The numerical results were compared with predictions from small deformation theory and the simulations of Das and Thaokar [80], where close agreement was observed. Simulations

of large deformation were presented to demonstrate the effects of the membrane's electrical properties on the equilibrium shape of the capsule. The chapter concludes with a simulation of the prolate-oblate-prolate transition for initially spheroidal capsules in a DC electric field.

In Section 6.1 a systematic parameter study of spherical capsules under the combined effects of shear flow and a DC electric field is conducted. While a number of researchers have studied droplets [89] and vesicles [72, 67, 74] in a combined shear flow and DC electric field, to the best of the present authors' knowledge the only comparable study for capsules is the small deformation analysis by Ha and Yang [75]. Furthermore, the analysis by Ha and Yang neglects the membrane's electrical properties, which are found to have a significant effect on the dynamics. For non-conducting capsules the membrane capacitance results in compressive electric stresses that develop at the equators, counteracting the deformation due to the shear flow. These stresses are stronger in stronger electric fields and thus, less deformation is observed in stronger fields, reversing the trend reported for neutral capsules by Ha and Yang in [75]. The membrane conductance reduces the effects of the membrane capacitance and the dynamics become heavily dependent on the electrical properties of the system. For membranes with high conductivities the capsule behavior approaches that of a neutral membrane as reported by Das and Thaokar in [80] for capsules in a DC electric field in the absence of a shear flow. The effects of varying the capillary number, electric field strength, viscosity ratio, and bending stiffness are also considered.

In Section 6.2 the work is concluded with numerical simulations of biconcave capsules in a combined shear flow and DC electric field. The electric field was found to have a number of significant effects on the dynamics of biconcave capsules. For capsules in the tumbling regime, weak electric fields exerted in the cross-stream direction decrease the tumbling frequency. Strong electric fields cause the capsule to transition from the tumbling to tank-treading regime. For capsules in the tank-treading mode, the electric field increases the capsule's inclination angle.

The present DTS scheme treats the flow as a quasi-steady problem and thus the method is limited to flows in the low Reynolds number regime. In order to ensure physical fidelity, careful consideration of the expected dynamics is advised when using the proposed numerical scheme for $\mathrm{Re} \geq 0.1$. For phenomena where the quasi-steady assumption does not hold, the method proposed by Gsell et al. in [87] could be employed. In the low Reynolds number regime discussed in this work, the proposed method has some advantages over the method from [87]. Neglecting the

transient term reduces the memory footprint of the algorithm by avoiding storage of the previous velocity and density fields. The present method also employs the standard LBM procedures for the collision and streaming steps, allowing for quick implementation into current LBM-IBM capsule codes.

For a given application the suitability of the proposed scheme is related to the physical time scales of interest. For capsule simulations in shear flow, the maximum size of the time step is limited by the desire to fully resolve the membrane response time scale, t_m. Using the time step selection proposed here, the minimum recommended ratio between the elastic time scale, t_m, and the traditional LBM time step, δt, is $t_m/\delta t \approx 200$, which results in a speed-up of approximately 2 using the DTS scheme. For electrohydrodynamic problems, the membrane charging time, t_c, places an additional constraint on the time step. For the parameter range considered here t_c is found to be smaller than t_m and thus resolution of the membrane dynamics require consideration of $t_c/\delta t$ and $t_m/\delta t$.

Red blood cells assume a biconcave shape in their unstressed shape and thus, understanding the effects of electric fields on their dynamics is important to the development of microfluidic devices, which use electrical and mechanical forces to study red blood cells [15]. The numerical simulations of capsules under the combined effects of shear flow and DC electric fields provide important insights into the effect of the numerous electrohydrodynamic parameters on the dynamics. The proposed immersed boundary-immersed interface DTS scheme also provides a framework for efficient simulations of capsule deformation in the electrohydrodynamic regime. Extension of the current numerical scheme to AC electric fields would allow for simulations of dielectrophoresis, which was shown to be an effective method for separation of healthy and malaria-infected red blood cells [13]. Future directions could also include consideration of the membrane viscosity allowing for comparison with the pulsed DC electric field experiments of [132], offering potential insights into the mechanisms of red blood cell shape memory.

REFERENCES

[1] S.-H. Lee, X. Nguyen, and H. Ko, "Study on droplet formation with surface tension for electrohydrodynamic inkjet nozzle," *Journal of Mechanical Science and Technology*, vol. 26, pp. 1403–1408, 2012.

[2] S. Mhatre, V. Vivacqua, M. Ghadiri, A. Abdullah, M. Al-Marri, A. Hassanpour, B. Hewakandamby, B. Azzopardi, and B. Kermani, "Electrostatic phase separation: A review," *Chemical Engineering Research and Design*, vol. 96, pp. 177–195, 2015.

[3] S. Mahnič-Kalamiza, E. Vorobiev, and D. Miklavčič, "Electroporation in food processing and biorefinery," *Journal of Membrane Biology*, vol. 247, pp. 1279–1304, 2014.

[4] P. van Hoogevest and A. Fahr, "Phospholipids in cosmetic carriers," in *Nanocosmetics: From Ideas to Products*, J. Cornier, C. M. Keck, and M. Van de Voorde, Eds. Cham, Switzerland: Springer International Publishing, 2019, pp. 95–140.

[5] G. Pieper, H. Rehage, and D. Barthés-Biesel, "Deformation of a capsule in a spinning drop apparatus," *Journal of Colloid and Interface Science*, vol. 202, pp. 296–300, 1998.

[6] R. Dimova, K. Riske, S. Aranda, N. Bezlyepkina, R. Knorr, and R. Lipowsky, "Giant vesicles in electric fields," *Soft Matter*, vol. 44, pp. 817–827, 2007.

[7] R. Hochmuth and R. Waugh, "Erythrocyte membrane elasticity and viscosity," *Annual Review of Physiology*, vol. 49, pp. 209–219, 1987.

[8] K. Mäller, D. Fedosov, and G. Gomper, "Margination of micro- and nano-particles in blood flow and its effect on drug delivery," *Scientific Reports*, vol. 4, p. 4871, 2014.

[9] D. Perrier, L. Rems, and P. Boukany, "Lipid vesicles in pulsed electric fields: Fundamental principles of the membrane response and its biomedical applications," *Advances in Colloid and Interface Science*, vol. 249, pp. 248–271, 2017.

[10] S. Chien, S. Usami, R. J. Dellenback, and M. I. Gregersen, "Blood viscosity: Influence of erythrocyte deformation," *Science*, vol. 157, pp. 827–829, 1967.

[11] T. W. Secomb, R. Skalak, N. Ozkaya, and J. F. Gross, "Flow of axisymmetric red blood cells in narrow capillaries," *Journal of Fluid Mechanics*, vol. 163, pp. 405–423, 1986.

[12] T. Yaginuma, M. Oliveira, R. Lima, T. Ishikawa, and T. Yamaguchi, "Human red blood cell behavior under homogenous extensional flow in a hyperbolic-shaped microchannel," *Biomicrofluidics*, vol. 7, p. 054 110, 2013.

[13] E. Du, M. Dau, and S. Suresh, "Quantitative biomechanics of healthy and diseased human red blood cells using dielectrophoresis in a microfluidic system," *Extreme Mechanics Letters*, vol. 1, pp. 35–41, 2014.

[14] M. Dao, C. T. Lim, and S. Suresh, "Mechanics of the human red blood cell deformed by optical tweezers," *Journal of the Mechanics and Physics of Solids*, vol. 51, pp. 2259–2280, 2003.

[15] M. Toner and D. Irimia, "Blood-on-a-chip," *Annual Review of Biomedical Engineering*, vol. 7, pp. 77–103, 2005.

[16] H. Henon, G. J. Sheard, and A. Fouras, "Erythrocyte deformation in a microfluidic cross-slot channel," *RSC Advances*, vol. 4, pp. 36 079–36 088, 2014.

[17] D. A. Fedosov, B. Caswell, and G. E. Karniadakis, "A multiscale red blood cell model with accurate mechanics, rheology, and dynamics," *Biophysics Journal*, vol. 98, pp. 2215–2225, 2010.

[18] R. Skalak, A. Tozeren, R. Zarda, and S. Chien, "Strain energy functions of red blood cell membranes," *Biophysical Journal*, vol. 13, pp. 245–264, 1973.

[19] W. Helfrich, "Elastic properties of lipid bilayers: Theory and possible experiments," *Zeitschrift fur Naturforschung*, vol. 28, pp. 693–703, 1973.

[20] R. Christensen, "A nonlinear theory of viscoelasticity for application to elastomers," *Journal of Applied Mechanics*, vol. 250, pp. 762–768, 1980.

[21] G. Taylor, "The viscosity of a fluid containing small drops of another fluid," *Proceedings of the Royal Society A*, vol. 138, no. 834, pp. 41–48, 1932.

[22] H Schmid-Schönbein and R. Wells, "Fluid drop-like transition of erythrocytes under shear," *Science*, vol. 165, pp. 3288–3291, 1969.

[23] H. Goldsmith and J. Marlow, "Flow behaviour of erythrocytes I: Rotation and deformation in dilute suspensions," *Proceedings of the Royal Society London B*, vol. 182, pp. 351–384, 1972.

[24] T. Fischer, M Stöhr-Liesen, and H. Schmid-Schönbein, "The red cell as a fluid droplet: Tank tread-like motion of the human erythtocyte membrane in shear flow," *Science*, vol. 202, no. 4370, pp. 894–896, 1978.

[25] S. Chien, "Red cell deformability and its relevance to blood flow," *Annual Review of Physiology*, vol. 49, pp. 177–192, 1987.

[26] J. Dupire, M. Socol, and A. Viallat, "Full dynamics of a red blood cell in shear flow," *Proceedings of the National Academy of Sciences for the United States of America*, vol. 109, no. 51, pp. 20 808–20 813, 2012.

[27] T. Fischer and R. Korzeniewski, "Threshold shear stress for the transition between tumbling and tank-treading of red blood cells in shear flow: Dependence on the viscosity of the suspending medium," *Journal of Fluid Mechanics*, vol. 736, pp. 351–365, 2013.

[28] D. Barthés-Biesel, "Motion and deformation of elastic capsules and vesicles in flow," *Annual Review of Fluid Mechanics*, vol. 48, pp. 25–52, 2016.

[29] F. Rumscheidt and S. Mason, "Particle motions in sheared suspensions XI. Internal circulation in fluid droplets (experimental)," *Journal of Colloid Sciences*, vol. 16, pp. 210–237, 1961.

[30] T. Fischer, M Stöhr-Liesen, and H. Schmid-Schönbein, "Red blood cell microrheology: Comparison of the behavior of single cell rbc and liquid drops in shear flow," *American Institute of Chemical Engineers Symposium Series*, vol. 182, no. 74, pp. 38–45, 1978.

[31] D. Barthés-Biesel, "Motion of a spherical microcapsule freely suspended in a linear shear flow," *Journal of Fluid Mechanics*, vol. 100, pp. 831–853, 1980.

[32] D. Barthés-Biesel and J. Rallison, "Role of membrane viscosity in the orientation and deformation of a spherical capsule suspended in shear flow," *Journal of Fluid Mechanics*, vol. 160, pp. 119–135, 1985.

[33] D. Barthés-Biesel and H. Sgaier, "The time-dependent deformation of a capsule freely suspended in a linear shear flow," *Journal of Fluid Mechanics*, vol. 113, pp. 251–267, 1981.

[34] K. Chang and W. Olbricht, "Experimental studies of the deformation and breakup of a synthetic capsule in steady and unsteady simple shear flow," *Journal of Fluid Mechanics*, vol. 250, pp. 609–633, 1993.

[35] A. Walter, H. Rehage, and H. Leonhard, "Shear induced deformation of polyamide microcapsules," *Colloid Polymer Science*, vol. 278, pp. 169–175, 2000.

[36] C. Pozrikidis, "Finite deformation of liquid capsules enclosed by elastic membranes in simple shear flow," *Journal of Fluid Mechanics*, vol. 297, pp. 123–152, 1995.

[37] S. Ramanujan and C. Pozrikidis, "Deformation of liquid capsules enclosed by elastic membranes in simple shear flow: Large deformations and the effect of fluid viscosities," *Journal of Fluid Mechanics*, vol. 361, pp. 117–143, 1998.

[38] C. Peskin, "The immersed boundary method," *Acta Numerica*, vol. 11, pp. 479–517, 2002.

[39] C. Eggleton and A. Popel., "Large deformation of red blood cell ghosts in a simple shear flow," *Physics of Fluids*, vol. 10, pp. 1834–1845, 1998.

[40] A. Walter, H. Rehage, and H. Leonhard, "Shear induced deformation of microcapsules: Shape oscillations and membrane folding," *Colloids and Surfaces A*, vol. 183, pp. 123–132, 2001.

[41] C. Pozrikidis, "Effect of membrane bending stiffness on the deformation of capsules in simple shear flow," *Journal of Fluid Mechanics*, vol. 440, pp. 2669–2691, 2001.

[42] ——, "Interfacial dynamics for Stokes flow," *Journal of Computational Physics*, vol. 169, pp. 250–301, 2001.

[43] ——, "Numerical simulation of flow-induced deformation of red blood cells," *Annals of Biomedical Engineering*, vol. 31, pp. 1194–1205, 2003.

[44] Y. Sui, Y. Chew, P. Roy, and H. Low, "A hybrid method to study flow-induced deformation of three-dimensional capsules," *Journal of Computational Physics*, vol. 227, pp. 6351–6371, 2008.

[45] Y. Sui, Y. Chew, P. Roy, Y. Cheng, and H. Low, "Dynamic motion of red blood cells in simple shear flow," *Physics of Fluids*, vol. 20, p. 112 106, 2008.

[46] D. Le, "Effect of bending stiffness on the deformation of liquid capsules enclosed by thin shells in shear flow," *Physical Review E*, vol. 82, p. 016 318, 2017.

[47] D. Cordasco and P. Bagchi, "On the shape memory of red blood cells," *Physics of Fluids*, vol. 29, p. 041 901, 2017.

[48] T. Omomori, T. Ishikawa, D. Barthés-Biesel, A.-V. Salsac, Y. Imai, and T. Yamaguchi, "Tension of red blood cell membrane in simple shear flow," *Physical Review E*, vol. 86, p. 056 321, 2012.

[49] A. Farutin, T. Biben, and C. Misbah, "3d numerical simulations of vesicle and inextensible capsule dynamics," *Journal of Computational Physics*, vol. 275, pp. 539–568, 2014.

[50] Z. Peng, A. Mashayekh, and Q. Zhu, "Erythrocyte responses in low-shear-rate flows: Effects of non-biconcave stress-free state in the cytoskeleton," *Journal of Fluid Mechanics*, vol. 742, pp. 96–118, 2014.

[51] K. Tsubota, S. Wada, and H. Liu, "Elastic behavior of a red blood cell with the membranes nonuniform natural state: Equilibrium shape, motion transition under shear flow, and elongation during tank-treading motion," *Biomechanical Modeling and Mechanobiology*, vol. 13, pp. 735–746, 2014.

[52] Z. Peng, S. Salehyar, and Q. Zhu, "Stability of the tank-treading modes of erythrocytes and its dependence on cytoskeleton reference states," *Journal of Fluid Mechanics*, vol. 771, pp. 449–467, 2015.

[53] K. Sinha and M. Graham, "Dynamics of a single red blood cell in simple shear flow," *Physical Review E*, vol. 92, p. 042 710, 2015.

[54] D. Le and Z. Tan, "Large deformation of liquid capsules enclosed by thin shells immersed in the fluid," *Journal of Computational Physics*, vol. 229, pp. 4097–4116, 2010.

[55] A. Z. K. Yazdani and P. Bagchi, "Phase diagram and breathing dynamics of a single red blood cell and a biconcave capsule in dilute shear flow," *Physical Review E*, vol. 84, p. 026 314, 2011.

[56] W. Huang, C. Chang, and H. Sung, "Three-dimensional simulation of elastic capsules in shear flow by the penalty immersed boundary method," *Journal of Computational Physics*, vol. 231, pp. 3340–3364, 2012.

[57] D. Cordasco and P. Bagchi, "Intermittency in red blood cell dynamics," *Journal of Fluid Mechanics*, vol. 759, pp. 472–488, 2014.

[58] R. Allan and S. Mason, "Particle behavior in shear and electric fields I. Deformation and burst of fluid drops," *Proceedings of the Royal Society of London. Series A, Mathematical and Physical Sciences*, vol. 267, no. 1328, pp. 45–61, 1962.

[59] G. Taylor, "Studies in electrohydrodynamics I. The circulation produced in a drop by an electric field," *Proceedings of the Royal Society A*, vol. 291, no. 1425, pp. 159–166, 1966.

[60] J. Melcher and G. Taylor, "Electrohydrodynamics: A review of the role of interfacial shear stresses," *Annual review of fluid mechanics*, vol. 1, no. 1, pp. 111–146, 1969.

[61] D. Saville, "Electrohydrodynamics: The Taylor-Melcher leaky dielectric model," *Annual review of fluid mechanics*, vol. 29, no. 1, pp. 27–64, 1997.

[62] P. M. Vlahovska, "Electrohydrodynamics of drops and vesicles," *Annual Review of Fluid Mechanics*, vol. 51, pp. 305–330, 2019.

[63] M. S. Abbasi, R. Song, S. Cho, and J. Lee, "Electro-hydrodynamics of emulsion droplets: Physical insights to applications," *Micromachines*, vol. 11, no. 10, p. 942, 2020.

[64] K. A. DeBruin and W. Krassowska, "Modeling electroporation in a single cell I. Effects of field strength and rest potential," *Biophysical Journal*, vol. 77, pp. 1213–1224, 1999.

[65] J. T. Schwalbe, P. M. Vlahovska, and M. J. Miskis, "Vesicle electrohydrodynamics," *Physical Review E*, vol. 83, p. 046 309, 2011.

[66] K. Sinha, S. Das, R. b. Karyappa, and R. M. Thaokar, "Electrohydrodynamics of vesicles and capsules," *Langmuir*, vol. 36, pp. 4863–4886, 2020.

[67] L. C. McConnel, M. J. Miskis, and P. M. Vlahovska, "Vesicle electrohydrodynamics in DC electric fields," *IMA Journal of Applied Mathematics*, vol. 78, no. 4, pp. 797–817, 2013.

[68] L. C. McConnel, P. M. Vlahovska, and M. J. Miskis, "Vesicle dynamics in uniform electric fields: Squaring and breathing," *Soft Matter*, vol. 11, pp. 4840–4846, 2015.

[69] L. C. McConnel, M. J. Miskis, and P. M. Vlahovska, "Continuum modeling of the electric-field-induced tension in deforming lipid vesicles," *The Journal of Chemical Physics*, vol. 143, no. 24, p. 243 132, 2015.

[70] E. M. Kolahdouz and D. Salac, "A numerical model for the transmembrane voltage of vesicles," *Applied Mathematics Letters*, vol. 39, pp. 7–12, 2015.

[71] ——, "Electrohydrodynamics of three-dimensional vesicles: A numerical approach," *SIAM Journal of Scientific Computing*, vol. 37, no. 3, B473–B494, 2015.

[72] ——, "Dynamics of three-dimensional vesicles in DC electric fields," *Physical Review E*, vol. 92, p. 012 302, 2015.

[73] A. Morshed, P. Dutta, M. R. Hossan, and R. Dillon, "Electrodeformation of vesicles suspended in a liquid medium," *Physical Review Fluids*, vol. 3, p. 103 702, 2018.

[74] W.-F. Hu, M.-C. Lai, Y. Seol, and Y.-N. Young, "Vesicle electrohydrodynamic simulations by coupling immersed boundary and immersed interface method," *Journal of Computational Physics*, vol. 317, pp. 66–81, 2016.

[75] J.-W. Ha and S.-M. Yang, "Electrohydrodynamic effects on the deformation and orientation of a liquid capsule in a linear flow," *Physics of Fluids*, vol. 12, pp. 1671–1682, 2000.

[76] R. Karyappa, S. Deshmukh, and R. Thaokar, "Deformation of an elastic capsule in a uniform electric field," *Physics of Fluids*, vol. 26, p. 122 108, 2014.

[77] S. Puri and R. M. Thaokar, "Study of dependence of elasticity on the microstructure of microcapsules using electro-deformation technique," *Colloids and Surfaces A*, vol. 569, pp. 179–189, 2019.

[78] M. Ouriemi and P. M. Vlahovska, "Electrohydrodynamic deformation and rotation of a particle-coated drop," *Langmuir*, vol. 31, no. 23, pp. 6298–6305, 2015.

[79] R. M. Thaokar, "Time-dependent electrohydrodynamics of a compressible viscoelastic capsule in the small-deformation limit," *Physical Review E*, vol. 94, p. 042 607, 2016.

[80] D. Das and R. M. Thaokar, "Large-deformation electrohydrodynamics of an elastic capsule in a DC electric field," *Journal of Fluid Mechanics*, vol. 841, pp. 489–520, 2018.

[81] S. Das and R. M. Thaokar, "Large deformation electrohydrodynamics of a Skalak elastic capsule in AC electric field," *Soft Matter*, vol. 14, no. 9, p. 1719, 2018.

[82] S. Das, S. D. Deshmukh, and R. M. Thaokar, "Deformation of a biconcave-discoid in extensional flow and electric field," *Journal of Fluid Mechanics*, vol. 860, pp. 115–144, 2019.

[83] T. Krüger, F. Varnik, and D. Raabe, "Efficient and accurate simulations of deformable particles immersed in a fluid using a combined immersed boundary lattice Boltzmann finite element method," *Computers and Mathematics with Applications*, vol. 61, pp. 3485–3505, 2011.

[84] J. Gounley and Y. Peng, "Response and recovery times of elastic and viscoelastic capsules in shear flow," *Communications in Computational Physics*, vol. 17, no. 5, pp. 1151–1168, 2015.

[85] A. Ghaffarian and K. Hejranfar, "An implicit dual-time stepping spectral dfifference lattice Boltzmann method for simulation of viscous compressible flows on structured meshes," *Meccanica*, vol. 54, pp. 1561–1581, 2019.

[86] G. Guzel and I. Koc, "Time-accurate flow simulations using a finite-volume based lattice Boltzmann flow solver with dual time stepping scheme," *International Journal of Computational Methods*, vol. 13, no. 6, p. 1 650 035, 2016.

[87] S. Gsell, U. D'Ortona, and J. Favier, "Multigrid dual-time stepping lattice Boltzmann method," *Physical Review E*, vol. 101, p. 023 309, 2020.

[88] D. Mavriplis, "Multigrid solution of the steady-state lattice Boltzmann equation," *Computers & Fluids*, vol. 35, pp. 793–804, 2006.

[89] W.-F. Hu, M.-C. Lai, and Y.-N. Young, "A hybrid immersed boundary and immersed interface method for electrohydrodynamic simulations," *Journal of Computational Physics*, vol. 282, pp. 47–61, 2015.

[90] M. R. Hossan, R. Dillon, and P. Dutta, "Hybrid immersed interface-immersed boundary methods for AC dielectrophoresis," *Journal of Computational Physics*, vol. 270, pp. 640–659, 2014.

[91] S. Mählmann and D. T. Papageorgiou, "Numerical study of electric field effects on the deformation of two-dimensional liquid drops in simple shear flow at arbitrary Reynolds number," *Journal of Fluid Mechanics*, vol. 626, pp. 367–393, 2009.

[92] S. Mandal and S. Chakraborty, "Effect of uniform electric field on the drop deformation in simple shear flow and emulsion shear rheology," *Physics of Fluids*, vol. 29, p. 072 109, 2017.

[93] P. M. Vlahovska, "On the rheology of a dilute emulsion in a uniform electric field," *Journal of Fluid Mechanics*, vol. 670, pp. 481–503, 2011.

[94] E. Lac, D. Barthés-Biesel, N. Pelekasis, and J. Tsamopoulos, "Spherical capsules in three-dimensional unbounded Stokes flows: Effect of the membrane constitutive law and onset of buckling," *Journal of Fluid Mechanics*, vol. 516, pp. 303–334, 2004.

[95] D. Barthés-Biesel, A. Diaz, and E. Dhenin, "Effect of constitutive laws for two-dimensional membranes on flow-induced capsule deformation," *Journal of Fluid Mechanics*, vol. 460, pp. 211–222, 2002.

[96] O. Zhong-can and W. Helfrich, "Bending energy of vesicle membranes: General expressions for the first, second, and third variation of the shape energy and applications to spheres and cylinders," *Physical Review A*, vol. 39, no. 10, pp. 5280–5288, 1989.

[97] X. Li and K. Sarkar, "Front tracking simulation of deformation and buckling instability of a liquid capsule enclosed by an elastic membrane," *Journal of Computational Physics*, vol. 227, pp. 4998–5018, 2008.

[98] D. V. Le, "Subdivision elements for large deformation of liquid capsules enclosed by thin shells," *Computer Methods in Applied Mechanics and Engineering*, vol. 199, pp. 2622–2632, 2010.

[99] Y. Sui, Y. Chew, P. Roy, and H. Low, "Inertia effect on the transient deformation of elastic capsules in simple shear flow," *Computers and Fluids*, vol. 38, pp. 49–59, 2009.

[100] G. Taylor, "The formulation of emulsions in definable fields of flow," *Proceedings of the Royal Society A*, vol. 146, no. 858, pp. 501–523, 1934.

[101] S. Deng, K. Ito, and Z. Li, "Three-dimensional elliptic solvers for interface problems and applications," *Journal of Computational Physics*, vol. 184, no. 1, pp. 215–243, 2003.

[102] C. Armstrong and Y. Peng, "Numerical simulations of capsule deformation using a dual time-stepping lattice Boltzmann method," *Phys. Rev. E*, vol. 103, no. 2, p. 023 309, 2021.

[103] J. Charrier, S. Shrivastava, and R. Wu, "Free and constrained inflation of elastic membranes in relation to thermoforming - Non-Axisymmetric problems," *Journal of Strain Analysis*, vol. 24, no. 2, pp. 55–74, 1989.

[104] X. He and L. Luo, "Lattice Boltzmann model for the incompressible Navier-Stokes equation," *Journal of Statistical Physics*, vol. 88, pp. 927–944, 3 1997.

[105] T. Krüger, H. Kusumaatmaja, A. Kuzmin, O. Shardt, G. Silva, and E. M. Viggen, *The Lattice Boltzmann Method: Principles and Practice*. Springer, 2017.

[106] D. d'Humiéres, I. Ginzburg, M. Krafczyk, P. Lallemand, and L. Luo, "Multiple-relaxation-time lattice Boltzmann models in three dimensions," *Philosophical Transactions of The Royal Society A Mathematical Physical and Engineering Sciences*, vol. 360, pp. 437–451, 2002.

[107] P. Lallemand, L. Luo, and Y. Peng, "A lattice Boltzmann front-tracking method for interface dynamics with surface tension in two dimensions," *Journal of Computational Physics*, vol. 226, no. 2, pp. 1367–1384, 2007.

[108] J. Tölke, M. Krafcczyk, and R. Ernst, "A multigrid-solver for the discrete Boltzmann equation," *Journal of Statistical Physics*, vol. 107, pp. 573–591, 1 2002.

[109] W. Briggs, V. Henson, and S. McCormick, *A Multigrid Tutorial*, 2nd ed. Philadelphia, PA: SIAM Books, 2000.

[110] U. Trottenberg, C. Osterlee, and A. Schuller, *Multigrid*. San Diego, CA: Academic Press, Inc., 2001.

[111] R. J. Leveque and Z. Li, "The immersed interface method for elliptic equations with discontinuous coefficients and singular sources," *SIAM Journal on Numerical Analysis*, vol. 31, no. 4, pp. 1019–1044, 1994.

[112] Z. Li, "A fast iterative algorithm for elliptic interface problems," *SIAM Journal on Numerical Analysis*, vol. 35, no. 1, pp. 230–254, 1998.

[113] J.-J. Xu, W. Shi, W.-F. Hu, and J.-J. Huang, "A level-set immersed interface method for simulation the electrohydrodynamics," *Journal of Computational Physics*, vol. 400, p. 108 956, 2020.

[114] A. Guckenberg, M. Schrame, P. G. Chen, M. Leonetti, and S. Gekle, "On the bending algorithms for soft objects in flows," *Computer Physics Communications*, vol. 207, pp. 1–23, 2016.

[115] A. Guckenberg and S. Gekle, "Theory and algorithms to compute Helfrich bending forces: A review," *Journal of Physics: Condensed Matter*, vol. 29, p. 203 001, 2017.

[116] R. Garimella and B. Swartz, "Curvature estimation for unstructured triangulations of surfaces," Los Alamos National Laboratory, Los Alamos, NM, Tech. Rep. LA-UR-03-8240, 2003.

[117] M. Reuter, S. Biasotti, D. Giorgi, G. Patané, and M. Spagnuolo, "Discrete Laplace-Beltrami operators for shape analysis and segmentation," *Computer & Graphics*, vol. 33, pp. 381–390, 2009.

[118] U. Pinkall and K. Polthier, "Computing discrete minimal surfaces and their conjugates," *Experimental Mathematics*, vol. 2, pp. 15–36, 1993.

[119] M. Meyer, M. Desbrun, P. Schröder, and A. Barr, "Discrete differential- geometry operators for triangulated 2-manifolds," 2002.

[120] J. Walter, A.-V. Salsac, D. Barthés-Biesel, and P. L. Tallec, "Coupling of finite element and boundary integral methods for a capsule in a Stokes flow," *International Journal for Numerical Methods in Engineering*, vol. 83, pp. 829–850, 2010.

[121] J. Walter, A.-V. Salsac, and D. Barthés-Biesel, "Ellipsoidal capsules in simple shear flow: Prolate versus oblate initial shapes," *Journal of Fluid Mechanics*, vol. 676, pp. 318–347, 2011.

[122] J. Zhang, P. C. Johnson, and A. S. Popel, "An immersed boundary lattice Boltzmann approach to simulate deformable liquid capsules and its application to microscopic blood flows," *Physical Biology*, vol. 4, pp. 285–295, 2007.

[123] D. Patil, K. N. Premnath, and S. Banerjee, "Multigrid lattice Boltzmann method for accelerated solution of elliptic equations," *Journal of Computational Physics*, vol. 265, pp. 172–194, 2014.

[124] C. Armstrong and Y. Peng, "An mrt extension to the multigrid lattice Boltzmann method," *Communications in Computational Physics*, vol. 26, no. 4, pp. 1178–1195, 2019.

[125] M. Abkarian, M. Faivre, and A. Viallat, "Swinging of red blood cells under shear flow," *Physical Review Letters*, vol. 98, p. 188 302, 2007.

[126] S. Kessler, R. Finken, and U. Seifert, "Swinging and tumbling of elastic capsules in shear flow," *Journal of Fluid Mechanics*, vol. 605, pp. 207–226, 2008.

[127] P. Bagchi and R. Kalluri, "Dynamics of nonspherical capsules in shear flow," *Physical Review E*, vol. 80, p. 016 307, 2009.

[128] Y. Fung, *Biomechanics: Mechanical Properties of Living Tissues*, 2nd ed. New York, NY: Springer-Verlag, 1993.

[129] D. Cordasco, A. Yazdani, and P. Bagchi, "Comparison of erythrocyte dynamics in shear flow under different stress-free configurations," *Physics of Fluids*, vol. 26, p. 041 902, 2014.

[130] D. Le and Z. Tan, "Hydrodynamic interaction of elastic capsules in bounded shear flow," *Communications in Computational Physics*, vol. 16, no. 4, pp. 1031–1055, 2014.

[131] P. Vlahovska, R. S. Gracia, S. Aranda-Espinoza, and R. Dimova, "Electrohydrodynamic model of vesicle deformation in alternating electric fields," *Biophysical Journal*, vol. 96, pp. 4789–4803, 2009.

[132] H. Englehardt and E. Sackmann, "On the measurement of shear elastic moduli and viscosities of erythrocyte plasma membranes by transient deformation in high frequency electric fields," *Biophysical Journal*, vol. 54, pp. 495–608, 1988.

APPENDIX A

THE LEAKY DIELECTRIC MODEL

The fluids are assumed to obey Ohm's law, giving us the following expression for the current density, **J**, inside the fluid:

$$\mathbf{J} = \sigma\mathbf{E} + q\mathbf{u} \tag{147}$$

where σ is the fluid's conductivity, **E** is the electric field, q is the free charge, and **u** is the fluid velocity.

In the absence of sources, conservation of charge is given by:

$$\frac{\partial q}{\partial t} + \nabla \cdot \mathbf{J} = 0. \tag{148}$$

Applying Ohm's Law for a conducting fluid, from Equation (147), we can re-write this as:

$$\frac{\partial q}{\partial t} + \nabla \cdot (\sigma\mathbf{E} + q\mathbf{u}) = 0. \tag{149}$$

The charge will accumulate at the interface on a time scale given by, $\frac{\varepsilon^- + 2\varepsilon^+}{\sigma^- + 2\sigma^+}$, and thus for phenomena in which the relevant time scales of the physical problem are much larger than this, we can assume $q = 0$ in the bulk. If we further assume that time-varying currents are negligible, and thus that the electric field is irrotational, we can introduce an electric potential, $\mathbf{E} = -\nabla\psi$, and re-write Equation (149) as:

$$\nabla \cdot (\sigma \nabla \psi) = 0. \tag{150}$$

This equation is coupled with interface relations for the jump in potential, ψ, and current density $\mathbf{J} = -\sigma\nabla\psi \cdot \mathbf{n}$, across the interface [60].

The conductivity is assumed to be constant in the bulk and thus Equation (150) becomes Laplace's Equation. Continuity of the electric potential and current current density across the

interface results in the following system of equations:

$$\sigma^+ \Delta \psi^+ = 0 \quad \text{in} \quad \Omega^+ \tag{151}$$

$$\sigma^- \Delta \psi^- = 0 \quad \text{in} \quad \Omega^- \tag{152}$$

$$[\![\psi]\!] = 0 \text{ on } \Sigma \tag{153}$$

$$[\![\sigma \psi_n]\!] = 0 \text{ on } \Sigma \tag{154}$$

where $[\![\cdot]\!]$ denotes the jump in a variable from Ω^+ to Ω^-.

APPENDIX B

IMMERSED INTERFACE METHOD DETAILS

B.1 INTERPOLATION OF INTERFACE FUNCTIONS

Let $f(\mathbf{X})$ be a function defined on the interface and let (η, τ) be the local coordinates. An interpolation of f can be expressed based on its values at the control points, $\mathbf{X_i}$ as follows:

$$f(\mathbf{X}) = \sum_{|\mathbf{X}-\mathbf{X_i}|\leq R} \alpha_i f(\mathbf{X_i}) \tag{155}$$

where the interpolating coefficients α_i are as yet unknown.

To obtain the coefficients, α_i we use a Taylor series approximation about $\mathbf{X}$ to re-write the right hand side as follows:

$$f(\mathbf{X}) = \sum_{|\mathbf{X}-\mathbf{X_i}|\leq R} \alpha_i \big\{ f(\mathbf{X}) + (\mathbf{X}-\mathbf{X_i}) \cdot \nabla f(\mathbf{X}) + (\mathbf{X}-\mathbf{X_i})^T H[f(\mathbf{X})](\mathbf{X}-\mathbf{X_i}) + H.O.T \big\}.$$

Near the point $\mathbf{X}$, we can re-write this in terms of the local coordinates (η_i, τ_i) as follows:

$$f(\mathbf{X}) = \sum_{|\mathbf{X}-\mathbf{X_i}|\leq R} \big\{ \alpha_i f(\mathbf{X}) + \alpha_i \eta_i f_\eta(\mathbf{X}) + \alpha_i \tau_i f_\tau(\mathbf{X}) + \frac{1}{2}\alpha_i \eta_c^2 f_{\eta\eta}(\mathbf{X}) + \eta_i \tau_i f_{\eta\tau}(\mathbf{X}) + + \frac{1}{2}\tau_i^2 f_{\tau\tau}(\mathbf{X}) + H.O.T \big\}.$$

Requiring the right and left sides of the equation to match to second order gives us the following

system of equations:

$$\begin{aligned}
\sum \alpha_i &= 1 \\
\sum \alpha_i \eta_i &= 0 \\
\sum \alpha_i \tau_i &= 0 \\
\frac{1}{2} \sum \alpha_i \eta_i^2 &= 0 \\
\sum \alpha_i \eta_i \tau_i &= 0 \\
\frac{1}{2} \sum \alpha_i \tau_i^2 &= 0
\end{aligned}$$

The N control points in the Neighborhood, $|\mathbf{X} - \mathbf{X_i}| \leq R$, allow us to re-write this as a system of equations:

$$\begin{pmatrix}
1 & 1 & \dots & 1 & 1 \\
\eta_1 & \eta_2 & \dots & \eta_{N-1} & \eta_N \\
\tau_1 & \tau_2 & \dots & \tau_{N-1} & \tau_N \\
\frac{1}{2}\eta_1^2 & \frac{1}{2}\eta_2^2 & \dots & \frac{1}{2}\eta_{N-1}^2 & \frac{1}{2}\eta_N^2 \\
\eta_1\tau_1 & \eta_2\tau_2 & \dots & \eta_{N-1}\tau_{N-1} & \eta_N\tau_N \\
\frac{1}{2}\tau_1^2 & \frac{1}{2}\tau_2^2 & \dots & \frac{1}{2}\tau_{N-1}^2 & \frac{1}{2}\tau_N^2
\end{pmatrix}
\begin{pmatrix}
\alpha_1 \\ \alpha_2 \\ \vdots \\ \alpha_{N-1} \\ \alpha_N
\end{pmatrix}
=
\begin{pmatrix}
1 \\ 0 \\ 0 \\ 0 \\ 0 \\ 0
\end{pmatrix} \tag{156}$$

For $N > 6$ the system is over-determined and a least squares solution is obtained.

This interpolation method can also give us second order estimates of f_η, f_τ, $f_{\eta\eta}$, $f_{\eta\tau}$, and $f_{\tau\tau}$. By adjusting the right hand side vector in Equation (156). For example, an interpolation of $f_{\eta\tau}$ can be obtained by replacing the right hand side vector in Equation (156) as follows:

$$\begin{pmatrix}
1 & 1 & \dots & 1 & 1 \\
\eta_1 & \eta_2 & \dots & \eta_{N-1} & \eta_N \\
\tau_1 & \tau_2 & \dots & \tau_{N-1} & \tau_N \\
\frac{1}{2}\eta_1^2 & \frac{1}{2}\eta_2^2 & \dots & \frac{1}{2}\eta_{N-1}^2 & \frac{1}{2}\eta_N^2 \\
\eta_1\tau_1 & \eta_2\tau_2 & \dots & \eta_{N-1}\tau_{N-1} & \eta_N\tau_N \\
\frac{1}{2}\tau_1^2 & \frac{1}{2}\tau_2^2 & \dots & \frac{1}{2}\tau_{N-1}^2 & \frac{1}{2}\tau_N^2
\end{pmatrix}
\begin{pmatrix}
\alpha_1 \\ \alpha_2 \\ \vdots \\ \alpha_{N-1} \\ \alpha_N
\end{pmatrix}
=
\begin{pmatrix}
0 \\ 0 \\ 0 \\ 0 \\ 1 \\ 0
\end{pmatrix} \tag{157}$$

B.2 INTERPOLATION OF THE NORMAL DERIVATIVE AND COMPUTATION OF THE CORRECTION TERM

Solving the Immersed Interface problem to $O(\Delta x^2)$ requires computation of a correction term which depends on approximations of the jump in the ψ as well as its first and second derivatives. The jumps are expressed in the local coordinates (ξ, η, τ), where ξ is the normal direction to the surface at the projection point $\mathbf{X}^*_{ijk}$ and η and τ are coordinates in the plane tangent to the surface. In a small neighborhood of $\mathbf{X}^*_{ijk}$, we can parametrize the surface in terms of $\xi = \chi(\eta, \tau)$, η and τ. In this frame the jumps in ψ can be expressed as follows [101]:

$$[\![\psi]\!] = w \tag{158}$$

$$[\![\psi_\xi]\!] = g \tag{159}$$

$$[\![\psi_\eta]\!] = w_\eta \tag{160}$$

$$[\![\psi_\tau]\!] = w_\tau \tag{161}$$

$$[\![\psi_{\xi\xi}]\!] = g(\chi_{\eta\eta} + \chi_{\tau\tau}) + \left[\!\left[\frac{f}{\sigma}\right]\!\right] - w_{\eta\eta} - w_{\tau\tau} \tag{162}$$

$$[\![\psi_{\eta\eta}]\!] = w_{\eta\eta} - g\chi_{\eta\eta} \tag{163}$$

$$[\![\psi_{\tau\tau}]\!] = w_{\tau\tau} - g\chi_{\tau\tau} \tag{164}$$

$$[\![\psi_{\xi\eta}]\!] = w_\eta \chi_{\eta\eta} + w_\tau \chi_{\eta\tau} + g_\eta \tag{165}$$

$$[\![\psi_{\xi\tau}]\!] = w_\eta \chi_{\eta\tau} + w_\tau \chi_{\tau\tau} + g_\tau \tag{166}$$

$$[\![\psi_{\eta\tau}]\!] = w_{\eta\tau} - g\chi_{\eta\tau}.. \tag{167}$$

Solution of the Poisson system gives us u_{ijk} at the Eulerian nodes. In order to estimate the jump in u_n across the interface we need to approximate u_n^+ and u_n^- at the control points. This can be achieved at a control point, $\mathbf{X}$, to second order using the following form:

$$u_n^-(\mathbf{X}) = \sum \gamma_{ijk} u_{ijk} - C(\mathbf{X}) \tag{168}$$

where C is a correction term, accounting for the jump across the interface and the γ_{ijk} are the interpolating coefficients.

In terms of the local coordinates (ξ_i, η_j, τ_k) on the inside of the interface Taylor series expansion

of u_{ijk} about $\mathbf{X}$ is given by:

$$u_{ijk} = u^-(\mathbf{X}) + \xi_i u^-_\xi(\mathbf{X}) + \eta_j u^-_\eta(\mathbf{X}) + \tau_k u^-_\tau(\mathbf{X}) + \frac{1}{2}\xi_i^2 u^-_{\xi\xi}(\mathbf{X}) + \xi_i\eta_j u^-_{\xi\eta}(\mathbf{X}) + \xi_i\tau_k u^-_{\xi\tau}(\mathbf{X}) + \frac{1}{2}\eta_j^2 u^-_{\eta\eta}(\mathbf{X}) + \eta_j\tau_k u^-_{\eta\tau}(\mathbf{X}) + \frac{1}{2}\tau_k^2 u^-_{\tau\tau}(\mathbf{X}).$$

Nodes outside the interface can be expanded in a similar fashion with the negative superscripts replaced with positive superscripts. Thus, the sum given in Equation (168) can be re-written in terms of u^- and u^+ evaluated at the control point as follows:

$$\sum_{(i,j,k)} \gamma_{ijk} u_{ijk} = \sum_{(i,j,k)\in\Omega^-} \gamma_{ijk} \begin{pmatrix} u^- + \xi_i u^-_\xi + \eta_j u^-_\eta + \tau_k u^-_\tau + \frac{1}{2}\xi_i^2 u^-_{\xi\xi} + \xi_i\eta_j u^-_{\xi\eta} \\ +\xi_i\tau_k u^-_{\xi\tau} + \frac{1}{2}\eta_j^2 u^-_{\eta\eta} + \eta_j\tau_k u^-_{\eta\tau} + \frac{1}{2}\tau_k^2 u^-_{\tau\tau} \end{pmatrix} + \sum_{(i,j,k)\in\Omega^+} \gamma_{ijk} \begin{pmatrix} u^+ + \xi_i u^+_\xi + \eta_j u^+_\eta + \tau_k u^+_\tau + \frac{1}{2}\xi_i^2 u^+_{\xi\xi} + \xi_i\eta_j u^+_{\xi\eta} \\ +\xi_i\tau_k u^+_{\xi\tau} + \frac{1}{2}\eta_j^2 u^+_{\eta\eta} + \eta_j\tau_k u^+_{\eta\tau} + \frac{1}{2}\tau_k^2 u^+_{\tau\tau} \end{pmatrix}$$

Introduce the following coefficients:

$$a_1 = \sum_{(i,j,k)\in\Omega^-} \gamma_{ijk} \qquad a_2 = \sum_{(i,j,k)\in\Omega^+} \gamma_{ijk}$$

$$a_3 = \sum_{(i,j,k)\in\Omega^-} \gamma_{ijk}\xi_i \qquad a_4 = \sum_{(i,j,k)\in\Omega^+} \gamma_{ijk}\xi_i$$

$$a_5 = \sum_{(i,j,k)\in\Omega^-} \gamma_{ijk}\eta_j \qquad a_6 = \sum_{(i,j,k)\in\Omega^+} \gamma_{ijk}\eta_j$$

$$a_7 = \sum_{(i,j,k)\in\Omega^-} \gamma_{ijk}\tau_k \qquad a_8 = \sum_{(i,j,k)\in\Omega^+} \gamma_{ijk}\tau_k$$

$$a_9 = \sum_{(i,j,k)\in\Omega^-} \gamma_{ijk}\xi_i^2 \qquad a_{10} = \sum_{(i,j,k)\in\Omega^+} \gamma_{ijk}\xi_i^2$$

$$a_{11} = \sum_{(i,j,k)\in\Omega^-} \gamma_{ijk}\eta_j^2 \qquad a_{12} = \sum_{(i,j,k)\in\Omega^+} \gamma_{ijk}\eta_j^2$$

$$a_{13} = \sum_{(i,j,k)\in\Omega^-} \gamma_{ijk}\tau_k^2 \qquad a_{14} = \sum_{(i,j,k)\in\Omega^+} \gamma_{ijk}\tau_k^2$$

$$a_{15} = \frac{1}{2}\sum_{(i,j,k)\in\Omega^-} \gamma_{ijk}\xi_i\eta_j \qquad a_{16} = \frac{1}{2}\sum_{(i,j,k)\in\Omega^+} \gamma_{ijk}\xi_i\eta_j$$

$$a_{17} = \frac{1}{2}\sum_{(i,j,k)\in\Omega^-} \gamma_{ijk}\xi_i\tau_k \qquad a_{18} = \frac{1}{2}\sum_{(i,j,k)\in\Omega^+} \gamma_{ijk}\xi_i\tau_k$$

$$a_{19} = \frac{1}{2}\sum_{(i,j,k)\in\Omega^-} \gamma_{ijk}\eta_j\tau_k \qquad a_{20} = \frac{1}{2}\sum_{(i,j,k)\in\Omega^+} \gamma_{ijk}\eta_j\tau_k.$$

allows us to re-write the Taylor expansion as follows:

$$\begin{aligned}\sum_{i=1}^{N} \gamma_{ijk}u_{ijk} = {} & a_1u^- + a_2u^+ + a_3u^-_\xi + a_4u^+_\xi + a_5u^-_\eta + a_6u^+_\eta \\ & + a_7u^-_\tau + a_8u^+_\tau + a_9u^-_{\xi\xi} + a_{10}u^+_{\xi\xi} + a_{11}u^-_{\eta\eta} + a_{12}u^+_{\eta\eta} + a_{13}u^-_{\tau\tau} \\ & + a_{14}u^+_{\tau\tau} + a_{15}u^-_{\xi\eta} + a_{16}u^+_{\xi\eta} + a_{17}u^-_{\xi\tau} + a_{18}u^+_{\xi\tau} + a_{19}u^-_{\eta\tau} + a_{20}u^+_{\eta\tau}.\end{aligned}$$

If we introduce a correction term, C:

$$C = a_2[\![u]\!] + a_4[\![u_\xi]\!] + a_6[\![u_\eta]\!] + a_8[\![u_\tau]\!] + a_{10}[\![u_{\xi\xi}]\!] + a_{12}[\![u_{\eta\eta}]\!] + a_{14}[\![u_{\tau\tau}]\!] + a_{16}[\![u_{\xi\eta}]\!] + a_{18}[\![u_{\xi\tau}]\!] + a_{20}[\![u_{\eta\tau}]\!]$$

We can re-write this in terms of u^- and its derivatives by introducing the correction term, C:

$$\begin{aligned}\sum_{i=1}^{N} \gamma_{ijk} u_{ijk} = {} & (a_1 + a_2)u^- + (a_3 + a_4)u^-_\xi + (a_5 + a_6)u^-_\eta + (a_7 + a_8)u^-_\tau \\ & + (a_9 + a_{10})u^-_{\xi\xi} + (a_{11} + a_{12})u^-_{\eta\eta} + (a_{13} + a_{14})u^-_{\tau\tau} \\ & + (a_{15} + a_{16})u^-_{\xi\eta} + (a_{17} + a_{18})u^-_{\xi\tau} + (a_{19} + a_{20})u^-_{\eta\tau} \\ & - C\end{aligned}$$

Looking at the right and left hand sides we see that in order for the γ_{ijk} to interpolate the normal derivative, we need to require:

$$a_3 + a_4 = 1 \tag{169}$$

$$a_{2j-1} + a_{2j} = 0, \ j \neq 2 \tag{170}$$

We can use these conditions to construct the following system:

$$\begin{pmatrix} 1 & 1 & \dots & 1 & 1 \\ \xi_{i_1} & \xi_{i_2} & \dots & \xi_{i_{N-1}} & \xi_{i_N} \\ \eta_{j_1} & \eta_{j_2} & \dots & \eta_{j_{N-1}} & \eta_{j_N} \\ \tau_{k_1} & \tau_{k_2} & \dots & \tau_{k_{N-1}} & \tau_{k_N} \\ \frac{1}{2}\xi^2_{i_1} & \frac{1}{2}\xi^2_{i_2} & \dots & \frac{1}{2}\xi^2_{i_{N-1}} & \frac{1}{2}\xi^2_{i_N} \\ \frac{1}{2}\eta^2_{j_1} & \frac{1}{2}\eta^2_{j_2} & \dots & \frac{1}{2}\eta^2_{j_{N-1}} & \frac{1}{2}\eta^2_{j_N} \\ \frac{1}{2}\tau^2_{k_1} & \frac{1}{2}\tau^2_{k_2} & \dots & \frac{1}{2}\tau^2_{k_{N-1}} & \frac{1}{2}\tau^2_{k_N} \\ \xi_{i_1}\eta_{j_1} & \xi_{i_2}\eta_{j_2} & \dots & \xi_{i_{N-1}}\eta_{j_{N-1}} & \xi_{i_N}\eta_{j_N} \\ \xi_{i_1}\tau_{k_1} & \xi_{i_2}\tau_{k_2} & \dots & \xi_{i_{N-1}}\tau_{k_{N-1}} & \xi_{i_N}\tau_{k_N} \\ \eta_{i_1}\tau_1 & \eta_2\tau_2 & \dots & \eta_{N-1}\tau_{N-1} & \eta_N\tau_N \end{pmatrix} \begin{pmatrix} \gamma_{i_1,j_1,k_1} \\ \gamma_{i_2,j_2,k_2} \\ \vdots \\ \gamma_{i_{N-1},j_{N-1},k_{N-1}} \\ \gamma_{i_N,j_N,k_N} \end{pmatrix} = \begin{pmatrix} 0 \\ 1 \\ 0 \\ \vdots \\ 0 \\ 0 \end{pmatrix} \tag{171}$$

Equation (171) is over-determined and the system is solved in the least squares sense.

Once the γ_{ijk} have been obtained, we can compute the a_i using Equations (169) and (170). With the a_i known we can compute the correction term, C.

B.3 IIM MATRIX COMPUTATIONS

For simulations in which the membrane's electrical properties are not considered the standard immersed interface method can be used. In this case the algorithm discussed by Deng et al. in [101] is used. Below is a brief outline of the numerical method. Equations (69) and (71) can be written as a block matrix equation in terms of the unknowns Ψ and G:

$$\begin{bmatrix} L & C_2 \\ D & E \end{bmatrix} \begin{bmatrix} \Psi \\ G \end{bmatrix} = \begin{bmatrix} F - C_1 W \\ PV \end{bmatrix}. \tag{172}$$

We can eliminate Ψ from the system by first solving the Schur complement:

$$\begin{aligned} \left(E - DL^{-1}C_2\right) G &= PV - DL^{-1}\left(F - C_1 W\right) \\ &\stackrel{\text{def}}{=} \bar{V}. \end{aligned} \tag{173}$$

Equation (173) is an $n_c \times n_c$ system for G, where n_c is the number of control points. This system is typically much smaller than the $n_x n_y n_z \times n_x n_y n_z$ system for Ψ.

In this work Equation (173) is solved iteratively using GMRES. The matrix vector multiplications and matrix inversions in Equation (173) are done without assembling the matrices. These computations are motivated by the observation that, if the jump condition $[\![\psi_n]\!] = Q$ is known, solution of the Poisson problem given by Equation (69) is:

$$\Psi(Q) = L^{-1}\left(F - C_1 W - C_2 Q\right)$$

where the solution is denoted by $\Psi(Q)$ to emphasize the solution's dependence on Q. $\Psi(Q)$ can be efficiently solved with a fast Poisson solver. Defining $\Psi_n^+(Q)$ and $\Psi_n^-(Q)$ as the approximation to the normal derivatives of the solution $\Psi(Q)$, we can write the residual of the known jump condition

$[\sigma\psi_n] = v$ as:

$$R(Q) = V - \left[\sigma^+\Psi_n^+(Q) - \sigma^-\Psi_n^-(Q)\right] \tag{174}$$

$$= PV - D\Psi(Q) - EQ \tag{175}$$

$$= PV - DL^{-1}(F - C_1W - C_2Q) - EQ. \tag{176}$$

In practice, $R(Q)$ is computed using Equation (174) after obtaining least squares approximations to Ψ_n^+ and Ψ_n^-.

The right-hand side vector, $\bar{V}$, from Equation (173) is obtained by computing $R(0)$. This can be easily seen by inserting $Q = 0$ into Equation (176) as follows:

$$R(0) = PV - DL^{-1}(F - C_1W) \tag{177}$$

$$= \bar{V}. \tag{178}$$

The matrix vector product, $\left(E - DL^{-1}C_2\right)Q$ is obtained from $R(Q)$ as follows:

$$\left(E - DL^{-1}C_2\right)Q = EQ - DL^{-1}C_2Q \tag{179}$$

$$= EQ - D\left[L^{-1}(F - C_1W) - \Psi(Q)\right] \tag{180}$$

$$= EQ - DL^{-1}(F - C_1W) + PV - PV + D\Psi(Q) \tag{181}$$

$$= PV - DL^{-1}(F - C_1W) + D\Psi(Q) + EQ - PV \tag{182}$$

$$= \bar{V} - R(Q). \tag{183}$$

The matrix-free algorithm for IIM can be summarized as follows:

1. Compute right-hand side vector $\bar{V}$

   i) Apply one step of the Immersed Interface Method with $Q = 0$ to obtain $\Psi(0) = L^{-1}(F - C_1W)$

   ii) Compute normal derivatives $\Psi_n^+(0)$ and $\Psi_n^-(0)$ based on $\Psi(0)$

   iii) Use normal derivatives to compute $\bar{V} = R(0)$ using Equation (174)

2. Solve Equation (174) iteratively with GMRES method until $R(Q) < \text{tol}$

i) Solve Immersed Interface Problem with $[\psi_n] = Q$

ii) Compute normal derivatives $\Psi_n^+(Q)$ and $\Psi_n^-(Q)$ based on $\Psi(Q)$

iii) Compute matrix vector multiplication, $\left(E - DL^{-1}C_2\right)Q$, using Equation (183)

3. Compute $\Psi(G)$ using a fast Poisson solver

APPENDIX C

SMALL DEFORMATION THEORY FOR HOOKEAN MEMBRANE

Below we derive the deformation of an elastic capsule in a DC electric field in the limit of small deformations for a leaky dielectric system. In [76], Karyappa et al. derive the deformation for the case of a perfect dielectric. The derivation here extends their work to the case of a leaky dielectric system and thus, it closely follows their work. The derivation also borrows elements from the derivation by Ouriemi and Vlahovska [78], who derived a similar result for the case of area inextensible membranes.

Consider an initially spherical capsule with radius a with matched viscosity $\lambda = 1$. For a capsule in an initially stationary flow, the problem is axisymmetric with radius, r, and polar angle θ. The polar angle measures the angle between $\mathbf{r}$ and the y axis. Let the permittivity and conductivity ratios be denoted as ε_r and σ_r, respectively, let the far-field condition on the electric potential be given by:

$$\mathbf{E} \to -E_0 r\cos\theta\hat{\mathbf{y}}, \tag{184}$$

and let the boundary conditions across the interface be given by:

$$[\![\psi]\!] = 0 \tag{185}$$

$$[\![\sigma\psi]\!] = 0. \tag{186}$$

Expanding the potential inside, ψ^-, and outside the capsule, ψ^+ in terms of the Legendre polynomials, $P_\ell(\cos\theta)$, and applying orthogonality conditions gives us the following solution:

$$\psi^-(r,\theta) = -E_0 r\cos\theta\frac{3}{\sigma_r+2} \tag{187}$$

$$\psi^+(r,\theta) = -E_0 r\cos\theta + E_0 a^3 r^{-2}\cos\theta\frac{\sigma_r-1}{\sigma_r+2}. \tag{188}$$

The electric fields are thus given by:

$$E_r^+(r,\theta) = E_0\left(1-2\frac{a^3}{r^3}\frac{\sigma_r-1}{\sigma_r+2}\right)\cos\theta \tag{189}$$

$$E_\theta^+(r,\theta) = -E_0\left(1+\frac{a^3}{r^3}\frac{\sigma_r-1}{\sigma_r+2}\right)\sin\theta \tag{190}$$

$$E_r^-(r,\theta) = \frac{3E_0}{\sigma_r+2}\cos\theta \tag{191}$$

$$E_\theta^-(r,\theta) = -\frac{3E_0}{\sigma_r+2}\sin\theta. \tag{192}$$

The electrical tractions result from the jump in the Maxwell stress tensor, τ_E^+, given by Equation (3) across the interface:

$$f_r(\theta) = \frac{\varepsilon^+}{2}\left[E_r^+E_r^+ - E_\theta^+E_\theta^- - \varepsilon_r\left(E_r^-E_r^- - E_\theta^-E_\theta^-\right)\right] \tag{193}$$

$$f_\theta(\theta) = \varepsilon^+\left(E_r^+E_\theta^+ - \varepsilon_r E_r^-E_\theta^-\right). \tag{194}$$

Inserting Equations (189)-(192) into Equations (193) and (194) gives us:

$$f_r(\theta) = \frac{9\varepsilon^+E_0^2\left[\sigma_r^2-1+\left(\sigma_r^2-2\varepsilon_r+1\right)\cos 2\theta\right]}{4\left(\sigma_r+2\right)^2} \tag{195}$$

$$f_\theta(\theta) = \frac{9\varepsilon^+E_0^2(\varepsilon_r-\sigma_r)\sin 2\theta}{2\left(\sigma_r+2\right)^2}. \tag{196}$$

Expand the radial deformation in Legendre polynomials:

$$u_r(\theta) = \sum_\ell s_\ell P_\ell(\cos\theta) \tag{197}$$

and assume the tangential deformation matches the form of the tangential force in Equation (196):

$$u_\theta(\theta) = s_\theta \sin 2\theta \tag{198}$$

where the coefficients s_ℓ and s_θ are currently unknown.

For small deformations the strains are related to the deformation as follows:

$$\varepsilon_\theta(\theta) = \frac{1}{a}\left(\frac{\partial u_\theta}{\partial \theta} + u_r\right) \tag{199}$$

$$\varepsilon_\phi(\theta) = \frac{1}{a}\left(u_r + \cot\theta u_\theta\right). \tag{200}$$

In terms of the Poisson ratio, ν, the generalized Hooke's law gives us the elastic tensions in terms of the strains as follows:

$$T_\theta = \frac{E_s}{1-\nu^2}\left(\varepsilon_\theta + \nu\varepsilon_\phi\right) \tag{201}$$

$$T_\phi = \frac{E_s}{1-\nu^2}\left(\varepsilon_\phi + \nu\varepsilon_\theta\right) \tag{202}$$

The equilibrium equations for the membrane are given by [76]:

$$\frac{T_\theta}{a} + \frac{T_\phi}{a} = f_r \tag{203}$$

$$\frac{\partial\left(\sin\theta T_\theta\right)}{\partial\theta} - \cos\theta T_\phi = -a\sin\theta f_\theta. \tag{204}$$

The coefficients for the expansion of the radial deformation, denoted by s_ℓ, and the coefficient for the tangential deformation s_θ can be obtained by multiplying Equations (203) and (204) by Legendre polynomials, integrating from 0 to π, and applying the resulting orthogonality conditions.

Through evaluation of the requisite integrals it can be shown that $s_1 = 0$, $s_\ell = 0$ for $\ell > 2$. The coefficients s_θ, s_0, and s_2 are given by:

$$s_\theta = -\frac{9a\varepsilon^+E_0^2(\nu+1)}{8E_s}\frac{(\sigma_r+1)^2 - 4\varepsilon_r}{(\sigma_r+2)^2} \tag{205}$$

$$s_0 = -\frac{3a\varepsilon^+E_0^2(\nu-1)}{4E_s}\frac{\sigma_r^2 + \varepsilon_r - 2}{(\sigma_r+2)^2} \tag{206}$$

$$s_2 = \frac{3a\varepsilon^+E_0^2}{4E_s}\frac{\sigma_r\nu(\sigma_r+6) + \sigma_r(5\sigma_r+6) - 16\varepsilon_r - 8\nu\varepsilon_r + 5 + \nu}{(\sigma_r+2)^2}. \tag{207}$$

In the small deformation limit the deformation of a Hookean membrane will match that of a neo-Hookean membrane and a Skalak membrane for $\nu = 1/2$. After inserting $\nu = 1/2$ into Equation

(207) and replacing $a\varepsilon^{+}E_0^2/E_s$ with Ca_E we have:

$$s_2 = \frac{3}{8}\mathrm{Ca}_E \frac{11\sigma_r^2 + 18\sigma_r + 11 - 40\varepsilon_r}{(\sigma_r + 2)^2}. \tag{208}$$

The tangential strain corresponds to membrane stretching and does not contribute to deformation and the shape coefficient s_0 applies a uniform pressure that is counteracted by the hydrostatic pressure. Thus, the deformation is solely due to the s_2 coefficient, and the shape equation of the capsule can be written as:

$$r(\theta) = a\left[1 + s_2 P_\ell(\cos\theta)\right]. \tag{209}$$

The capsule shape equation reaches its extrema at 0 and $\pi/2$ thus the equilibrium deformation parameter is given by:

$$D_{xy} = \frac{r(\pi/2) - r(0)}{r(\pi/2) + r(0)} \tag{210}$$

$$= \frac{1 + s_2 - 1 + \frac{1}{2}s_2}{2 + \frac{1}{2}s_2} \tag{211}$$

$$\approx \frac{3}{4}s_2. \tag{212}$$

where we have used the fact that $s_2 \ll 1$. Finally, the equilibrium deformation in the limit of small deformations can be expressed by inserting Equation (208) into Equation (212) giving us:

$$D_{xy} = \frac{9}{32}\mathrm{Ca}_E \frac{11\sigma_r^2 + 18\sigma_r + 11 - 40\varepsilon_r}{(\sigma_r + 2)^2}. \tag{213}$$

VITA

Charles Leland Armstrong
Department of Mathematics and Statistics
Old Dominion University
Norfolk, VA 23529

PREVIOUS DEGREES

M.S. Computational and Applied Mathematics, Old Dominion University, Norfolk, VA (2018)

B.S. Mathematics, Old Dominion University, Norfolk, VA (2015)

PUBLICATIONS

Charles Armstrong and Yan Peng. "Numerical simulations of capsule deformation using a dual time-stepping lattice Boltzmann method", *Physical Review E*, vol. 103, no. 4, p. 023309, 2021.

Charles Armstrong and Yan Peng. "An MRT extension to the multigrid lattice Boltzmann equation". *Communications in Computational Physics*, vol. 26, no. 4, pp. 1178-1195, 2019.

Typeset using LaTeX.